Microwave-assisted condensation of bio-based hydroxymethylfurfural and acetone over recyclable hydrotalcite-related materials

Alberto Tampieri,[a] Cesare Russo,[a] Raffaele Marotta,[b] Magda Constantí,[a] Sandra Contreras,[a] Francesc Medina*[a]

* Corresponding author. Email address: francesc.medina@urv.cat.

[a] DEQ, ETSEQ, Universitat Rovira i Virgili, Avinguda dels Països Catalans 26, 43007, Tarragona, Spain.

[b] DICMAPI, Università di Napoli Federico II, p.le V. Tecchio 80, 80125, Napoli, Italy.

Abstract

The microwave-assisted neat aldol condensation of biomass-derived platform chemical 5-hydroxymethyl furfural (HMF) and acetone over hydrotalcite-based catalysts has been studied. High conversions are obtained in very short times with relatively low catalyst loadings. The condensation products, which are biofuel and functional polymer precursors, are selectively obtained. Heterogeneous catalysts with different basic properties derived from the same parent hydrotalcite have been tested. The solids were characterized by PXRD, ICP-AES, ESEM-EDX, TEM, FT-IR and Raman spectroscopy, N_2 physisorption, CO_2 chemisorption and TGA-MS. The products in the final reaction mixtures were determined by GC-FID and -MS, HPLC-DAD and -TOF, and NMR. NMR was also used to determine the stereoconfiguration of the obtained products and pointed to a complete *E*-selectivity of our process. Different catalyst recycle strategies have been explored, and the most active catalyst, a meixnerite-type solid, can be recycled with low activity loss.

Keywords: Microwave-assisted organic synthesis, biofuel production, rehydrated hydrotalcite, layered double hydroxide, catalyst recycle.

1. Introduction

Production of energy and chemicals from the depleting fossil fuel feedstock may not meet the steadily-growing global demand at some point this century [1]. This, combined with the concerns about climate changes due to anthropogenic emissions [2], has pushed the scientific community in a search for alternative raw materials to satisfy our needs. In this regard, biomass has been individuated as a renewable and possibly sustainable pool of resources, being the only large organic carbon source on our planet other than fossil fuels [3–5]. Raw materials from fossil fuels and biomass are inherently different, as the former are generally constituted by largely unfunctionalized hydrocarbons whereas the constituents of the latter exhibit an array of functional groups and include heteroatoms at specific positions [6]. Chemocatalysis, in particular heterogeneous catalysis, plays a vital role in petroleum refining [7], reducing reaction times, energy consumptions and wastes. The same would likely be true in post-oil bio-refining, especially in energy-scarcity scenarios. Hence, it comes as no surprise that in the last decades considerable attention has been drawn to the design of suitable catalysts for the production and upgrade of bio-derived platform chemicals [8–10].

Six-carbon chains contained in the structure of the widely available hexoses may be exploited to obtain linear hexane [11]. Yet, *n*-hexane is at the lower chain-range limit for molecules in liquid-alkane transportation fuels [12]. Thus, methods to increase chain length are required to convert cellulosic materials into alkane biofuels. 5-hydroxymethyl furfural (HMF), obtained by dehydration of hexoses, is considered one of the bio-derived platform chemicals that will be most important in bio-refining [13]. However, HMF's potential has not been fully expressed yet, mostly due to its problematic isolation and lack of stability connected to the presence of the hydroxyl group in the structure [14,15]. These and other limitations have earned this building block the label of "sleeping giant" of sustainable chemistry [16]. HMF's high synthetic potential lies in the presence of three distinct oxygen-bearing functional groups in its structure (an aldehyde, an alcohol, and a furan ring), and a plethora of HMF derivatives with just as many applications have been reported [17]. The HMF's aldehyde moiety allows chain lengthening by means of carbon-carbon bond forming reactions such

as aldol condensations with suitable nucleophilic partners. This reaction is an important carbon-carbon bond formation tool in industry, where it is generally catalysed by homogeneous strong caustics [18]. Cross-reaction of HMF on one or both ends of acetone, which can also be obtained from biomass [19], affords chain lengths in the diesel and jet fuel ranges [20]. The condensation products, also known as C9 (mono-condensation) and C15 (double condensation), may be converted into linear alkanes by total hydrodeoxygenation (HDO) [21]. Such enones and their derivatives may also be alternatives to current petrol-derived monomers or cross-linking agents, or organic dyes [22]. This aldol condensation-based strategy unlocks the synthesis of linear paraffins with targeted chain lengths from biomass, as opposed to other protocols to obtain the same products but with little control over the obtained chain lengths (e. g. Fischer-Tropsch process) [23]. The same strategy has also been applied to furfural [24,25].

Processes for the condensation of HMF and acetone catalysed by alkalis such as NaOH have been reported [12,26]. Corrosion of the reaction vessels, difficult separation from the reaction mixtures and expensive wastewater treatments are major disadvantages of using these homogeneous caustics in aldol condensation processes [18]. Thereby, the development of analogous protocols involving heterogeneous catalysts would be highly desirable. After the group of Dumesic firstly envisioned this approach and demonstrated its feasibility [27], a number of protocols for the aldol condensation of HMF and acetone based on heterogeneous catalysis have been reported [28–40]. Hydrotalcites (HT) are carbonate minerals that belong to the category of layered double hydroxides (LDH). HT-like materials can be easily prepared by co-precipitation of suitable Mg and Al salts in basic media, and possess a laminar structure containing water and anions in the inter-layer space (Fig. 1) [41]. HTs find application in catalysis for their mild Brønsted basicity; on the other hand, HTs are often calcined to afford the correspondent mixed metal oxides (MMO), also known as layered double oxides (LDO), which are strong Lewis bases [42]. Mg/Al MMOs were reported as HMF-acetone aldol condensation catalysts in the seminal Dumesic's article [27]; later, the group of Ordóñez studied the process more in detail and developed a simplified kinetic model [29]. MMOs have been used in

the reaction of acetone with furfural, as well [43]. After HT calcination the layers collapse, but the LDH laminar structure is not completely lost and may be recovered if the MMO is immersed in an aqueous solution (Fig. 1) [44]. This strategy enables the preparation of HT-related catalysts containing different inter-layer components [45], and it has been used to obtain meixnerite-type (MX) solids, which are strong Brønsted bases [42]. It has already been demonstrated by our and other groups that catalysts of this class, also called re-hydrated HTs, are very active catalysts in aldol condensation reactions [43,46,47].

It was firstly reported in 1986 that reactions performed inside a commercial microwave (MW) oven experienced considerable rate increases [48,49]. Since then, the field of microwave-assisted organic synthesis (MAOS) has advanced significantly, and nowadays MW irradiation has become a popular heating method due to the unconventional heating profile and specific thermal effects such as selective heating and hotspot formation [50]. Microwaves are making their way to industry, not without their problems [51], as a result of the increasing interest and number of applications of microwave heating to chemical and material processing [52]. Many times it has been claimed that MAOS is a "green" chemistry because of the aforementioned effects that make MW heating a more efficient reaction heating method than conventional heating. However, the assessment of MAOS greenness is not straightforward and the energy efficiency should be analysed case by case [53,54]. Nonetheless, this type of dielectric heating proved to be particularly convenient in heterogeneous catalysis as the vast majority of solid catalysts are excellent MW absorbers [55,56].

Microwave irradiation already proved to be an outstanding heating method for the dehydration of hexoses to HMF [57], and to have beneficial effects in the preparation of HTs [58]. Additionally, it has recently been demonstrated that HT-related catalysts can catalyse the isomerization of glucose to fructose, which is a fundamental step in the synthesis of HMF from biomass [59]. From a process integration standpoint, the importance of developing a process to convert HMF into C9 and C15 that involves microwave irradiation and HT-related catalysts is apparent. Herein, we report a study of the batch, liquid-phase neat aldol condensation of HMF and acetone over HT-related materials with the

implementation of MW heating. 2:1 Mg:Al HTs with different degrees of modification (as-synthesized, calcined, regenerated and rehydrated) were tested as catalysts for the transformation, and their performances compared. Cycles of calcination-reconstruction were used to regenerate the solids obtained after reaction and assess the recycling potential of our catalysts, a crucial parameter for a green process. Both solid catalysts and reaction species in the liquid phase were thoroughly characterized by several analytical techniques.

2. Experimental

2.1. Catalyst preparations

The parent catalyst, a 2:1 Mg:Al hydrotalcite (HT), was prepared from its precursors (Mg and Al nitrates) by co-precipitation in de-ionized water with NaOH and Na_2CO_3 to supply carbonates and keep the pH constant at 10. The co-precipitation medium was let stirring overnight to afford the HT after filtration, washing with de-ionized water, drying at 373 K for 24 h and grinding to reduce particle size below 500 μm. All the other catalysts were prepared using HT as a starting material. After being used as a catalyst in an aldol condensation, the used HT was separated from the reaction mixture by filtration and washed with acetone. The solid obtained was left drying at room temperature to obtain the recovered HT (HT_{rec}). Calcination of HT at 723 K for 4 h afforded the correspondent mixed metal oxide (MMO). The MMO was regenerated by immersing the solid in 1 M aqueous $NaCO_3$ to obtain the regenerated HT (HT_{reg}) after centrifugation, filtration, washing with de-ionized water and drying at 373 K for 24 h. Rehydration of the MMO, immersed in pure de-ionized water, afforded a layered double hydroxide of the MX-type after centrifugation, filtration, washing with acetone and drying under vacuum. The prepared MMO, HT_{reg} and MX were also used as a catalyst in aldol condensations. After filtration and washing with acetone, the recovered MMO (MMO_{rec}), HT_{reg} (HT_{rec}) and MX (MX_{rec}), respectively, were obtained. These recovered catalysts were used as starting materials for the preparation of the recycled catalysts MMO', HT'$_{reg}$ and MX', which were prepared in the same

way as their parent MMO, HT_{reg} and MX, and used a second time as catalysts. Analogously, the MX'_{rec} recovered after aldol condensation was recycled to afford MX''. Finally, MX'' was used as a catalyst for a third time and recovered (MX''_{rec}). Detailed catalysts preparations are provided in the *Supplementary Information* (Section S3).

2.2. Catalyst characterization

The prepared catalysts were characterized by PXRD, ICP-AES, ESEM-EDX, TEM, FT-IR and Raman spectroscopy, N_2 physisorption, CO_2 chemisorption, and TGA-MS. PXRD measurements were performed ex situ using a Siemens D5000 diffractometer (Bragg-Brentano parafocusing geometry and vertical θ-θ goniometer) fitted with a curved graphite diffracted-beam monochromator, incident and diffracted-beam Soller slits, a 0.06° receiving slit and scintillation counter as a detector. The angular 2θ diffraction range was between 5 and 70°. The data were collected with an angular step of 0.05° at 3s per step and sample rotation. A low background Si (510) wafer was used as a sample holder. $Cu_{K\alpha}$ radiation was obtained from a copper X-ray tube operating at 40 kV and 30 mA.

ICP-AES analyses were performed on aqueous HT samples obtained after MW digestion in an Ethos Easy (Milestone) digester. The spectrometer used for the analysis was a 160 CCD (Spectro Arcos). The results and details of the ICP-AES analysis are provided in the *Supplementary Information* (Section S4.1).

ESEM analyses were performed using an Environmental Scanning Electron Microscope Quanta 600 (FEI Company). The EDX analyses were performed using an Oxford Instruments EDX detector. The analyses were performed at 20 kV accelerating voltage and 10 mm of working distance in high vacuum mode. The micrographs were taken on samples that were previously coated with gold using a Q150R ES sputter coater (Quorum Technologies). The thickness of the deposited gold layer was about 15 nm. The results and details of the EDX analysis are provided in the *Supplementary Information* (Section S4.2).

TEM images were collected using a JEOL 1011 Transmission Electron Microscope operating at 80 kV. The solid samples were dispersed in ethanol by sonication, and a drop of each of the resulting suspensions was poured on a different carbon coated-copper grid.

FT-IR spectra in the mid-IR region were recorded using a FT/IR 6700 Jasco spectrometer, with a TGS detector and equipped with an ATR PRO ONE accessory (diamond crystal kit high-throughput model optimized for mid-IR measurements). Each spectrum was recorded by accumulating 32 scans at a 4 cm^{-1} resolution between 600 and 4000 cm^{-1}.

Raman spectra in the mid-IR region were recorded using an inVia confocal Raman microscope (Renishaw) equipped with IlluminatIR II infrared microprobe (Smiths). Spectra were calibrated using the 520.5 cm^{-1} line of a silicon wafer. Each spectrum was recorded at a nominal resolution of 2 cm^{-1} in the range between 100 and 4000 cm^{-1}. For the excitation, a red (633 nm, HeNe, Renishaw RL633) and a near-IR laser (785 nm, Renishaw HPNIR785) were used. The results of the Raman analysis are provided in the *Supplementary Information* (Section S4.3).

TGA was performed using a SENSYS evo TG-DSC (S60/58129, Setaram Instrumentation). 2 to 6 mg of solid were placed in the analysis crucible. After an initial conditioning step (300 s at 303 K under flowing Ar (or synthetic air) at 30 sccm, a flow that was kept throughout the whole analysis), the crucible was heated up to 1073 K at a constant heating 10 K/min rate. This temperature was kept for 300 s and then the chamber was let cool down for 1540 s. The instrument outlet was connected to a mass spectrometer (HiCube pumping station and PrismaPlus QMG220, Pfeiffer Vacuum) for the determination of the gas composition. The results of the mass spectrometry analyses are provided in the *Supplementary Information* (Section S4.4).

The nitrogen adsorption-desorption isotherms, BET surface area and pore volume of the prepared catalysts were obtained by N_2 physisorption analysis at 77 K using a Quadrasorb *SI* Models 4.0 with the QuadraWin Software (Quantachrome Instruments, v. 5.0 + newer). Before analysis, the LDHs were outgassed at 393 K for 18 h under vacuum (6 mTorr) in the instrument pre-chamber (FloVac Degasser, Quantachrome Instruments) to remove the adsorbed species from the samples; the

MMO, less susceptible to high temperature thermal treatments, was outgassed at 473 K at the same conditions.

TPD-CO_2 studies were performed using an AutoChem II 2920 chemisorption analyzer (Micromeritics). About 100 mg of solid were placed inside the sample tube, together with glass wool to prevent the solid to be carried away. The solids were first dried at 393 K for 100 minutes under 30 sccm of He; then, in the CO_2 adsorption step, the solid was cooled to 308 K and kept under 30 sccm of 2.5% CO_2/He for 30 minutes; after that, for the CO_2 temperature-programmed desorption, the solid was heated to 1073 K at 10 K/min under 30 sccm of He. Degradation studies were performed following the same procedure but flowing with He instead of 2.5% CO_2/He in the CO_2 adsorption step. The results of the analyses were revealed by a thermal conductivity detector (TCD). A cold trap (cooling bath of ethanol:ethylene glycol 20:80 v:v at 208 K) was used to eliminate the contribute of water to the TCD signal. The results and details of the TPD-CO_2 analyses are provided in the *Supplementary Information* (Section S4.5).

2.3. Aldol condensation

The aldol condensations were performed under microwave irradiation and magnetic stirring inside an MW reactor (Fig. S11, single reaction chamber microwave synthesis system, Milestone SynthWAVE). The reactor setup is shown in Fig. 2. Up to five reaction tubes could be simultaneously placed in the reaction rack, and were used to run five identical parallel reactions. The rack was inserted in the PTFE reaction vessel and immersed in the water bath contained in it. The reaction chamber was tightly sealed before activating the MW heating, and in all cases it was pressurized with 10 bars of N_2 without performing any air purge. The reaction mixture consisted of 0.1 g of HMF in 5 mL of acetone, and variable amounts of solid catalyst. The reaction outcome was determined by GC-FID analysis of the final reaction mixtures using toluene as an internal standard. The samples were analyzed with a GC-2010 (Shimadzu) using a TRB-5 column (Teknokroma, TR-120232; length: 30 m, film thickness: 25 μm; inner diameter: 0.25 mm). In addition, liquid-phase ^{1}H NMR spectrometry

was used to establish the cis-trans ratio of the condensation products. NMR spectra were obtained by using a Varian VNMRSYS 400 equipped with a 5mm auto-switchable PFG probe and a Bruker Avance Neo NMR 400MHz equipped with a Smart PI HR-400-S1-BBF/H/D-5.0-Z SP N probe. All ^{1}H NMR spectra are reported in parts per million (ppm) downfield of TMS and were calibrated using the residual solvent peak of $CDCl_3$ (7.26 ppm) or the solvent peak of no-D acetone (2.09 ppm). For the latter, since the solvent is not deuterated, a capillary containing D_2O was inserted in the NMR tubes with the purpose of providing a signal for the lock. The final reaction mixtures were also analysed by GC-MS, HPLC-DAD, HPLC-TOF. Detailed reaction and analysis procedures are provided in the *Supplementary Information* (Section S5.3).

3. Results and discussion

3.1. Preliminary studies

We began our study by designing the reactor setup and defining the range of reaction conditions. The general structure of the bath temperature programs used for all experiments is depicted in Fig. 3. It is important to notice that the temperature sensor is immersed in the bath (Fig. 2); therefore, all reported temperatures refer to the bath ones, and never to the reaction ones, which are unknown. The microwave irradiation power was set to range from 0 to 300 W and it was automatically modulated by the reactor for the bath real temperature profile to match the temperature program. In a first, power-intensive step, the bath temperature was increased from room temperature to 363 K over a time t_1. This temperature was then kept for a time t_2, after which the bath was let cool down for a time t_3. During the cool-down step, which was t_3 = 20 min in all cases, the bath temperature lowers below 329 K, preventing acetone from boiling at the reaction chamber pressure release.

Initial exploration into the proposed aldol condensation process showed that the microwave-assisted neat reaction of HMF and acetone over the as-prepared HT at 2:1 HMF:HT was complete in a matter of hours. The reaction times were progressively decreased, and with a heating t_1 = 10 min

and a constant temperature t_2 = 20 min the conversion still was complete (Table 1, entry 1). It is common practice to count the reaction time starting from the moment the reaction temperature is reached until when the reaction is interrupted, which would correspond to t_2 in our case. However, the high conversions obtained by reducing progressively the reaction times made it clear that a non-negligible part of conversion happens during the heating step. Indeed, when t_2 is reduced to zero the conversion is still very high (entry 2). In this case, a real bath temperature of 363 K is not reached by the water bath before it starts cooling down. Considering that the test tube glass is a bad microwave absorber which poses an obstacle to the heat transfer, and that acetone is a worse microwave absorber than water, it is unlikely that the solvent ever reaches that temperature either. Hence, a 91 % conversion at these conditions is surprising considering the low basicity of as-synthesized HT. In light of this, we supposed that it is not the solvent temperature driving the reaction, but the MW irradiation instead. In this view, a possible explanation for the unnaturally high reactivity of the as-synthesized HT could be that the microwave irradiation is efficiently absorbed by the solid catalyst and that it creates hotspots inside it. This would imply also that the reaction outcome would be highly influenced by the power used to increase the bath temperature, which in our experience is not very reproducible. Thereby, in order to avoid reproducibility problems, the temperature program was modified as follows: t_1 was reduced to zero, whereas t_2 and t_3 were set at 10 and 20 minutes, respectively. As a result of that, the system is forced to reach a bath temperature of 363 K as soon as the reactor is activated, and over a t_2 of 10 minutes the MW irradiation is constant at ~300 W, the set higher limit (Fig. S13). At these conditions, the bath temperature experiences a non-linear increase and approaches 363 K at the end of the 10 minutes. The conversion obtained with this t_2-only method was 93 % (entry 3), comparable to the one of the t_1-only method (entry 2). With these heating parameters in hand, the catalyst loading was decreased. 20 mg of catalyst, corresponding to an HMF:HT ratio of 5:1, catalysed the conversion of about 70% of the reagent (entry 4) and it was used as a model catalyst loading for further investigation. Importantly, in a microwave-assisted blank

reaction no conversion is observed (entry 5), demonstrating that microwaves alone do not promote the reaction.

3.2. Catalyst characterization

Characterization of the solids before and after reaction shed light on the modifications to the HT structure and composition caused by the microwave-assisted process. XRD data obtained for HT is in accordance with the previously reported literature (Fig. 4) [44]. Analysis of HT_{rec}, the solid recovered after reaction, suggests that no substantial modification was brought about by the reaction. This indicates that the interaction of microwaves with the HT do not alter its structure significantly. The same conclusions stand after ESEM and TEM analyses of the same samples (Fig. 5a, b, d and e). Both HT and HT_{rec} exhibit the "desert rose"-like morphology typical of these LDH [47], and no visible differences can be spotted between their micrographs.

However, different observations are made for the changes in composition. There is a clear, visible change in the composition of the solid after reaction, which changes color from white (HT) to golden brown (HT_{rec}) (Fig. S1). EDX analysis of the two samples highlights a slight increase in the carbon content of the solids, although the overall compositions do not appear to have changed dramatically (Table 2, entries 1 and 2). These results point to a surficial composition change, probably caused by the adsorption of reaction species on the catalyst surface. FT-IR analysis provides some additional details about this composition change (Fig. 6). The recorded spectra are in accordance with previously reported ones. In the HT spectrum the broad band peaking at ~ 3400 cm^{-1} is generally associated with M-OH stretches [60]. The inflection point of this band at ~ 3100 cm^{-1} has been assigned to an H_2O-$[CO_3]^{2-}$ bridge [47]. The peak at ~ 1650 cm^{-1} corresponds to H_2O bending [47]. The sharp peak at ~ 1350 cm^{-1} is characteristic of the $[CO_3]^{2-}$ ν_3 mode [47]. Finally, the broad and intense band below 1100 cm^{-1} includes various peaks associated with M-OH translations [60,61]. The reaction does not seem to drastically modify the catalyst composition, as it can be seen on the HT_{rec} spectrum. Nevertheless, a crucial difference between the HT and the HT_{rec} spectra can be detected: a

peak at 1571 cm^{-1}, in the region of double bond stretches, which should belong to the adsorbed matter. This peak overlaps with the one of the H_2O bending. The adsorbed molecules should include multiple carbon-carbon and carbon-oxygen double bonds in their molecular structures. Therefore, it is possible that this peak includes more than one signal. At this stage, we did not have enough information on the identity of the adsorbed molecules to draw any conclusion from the presence and position of this peak. For this reason, we prepared C15 with an alternative protocol (following the procedure to obtain a product molar C9:C15 ratio of 0.04:1) [22]. The FT-IR spectrum of the obtained solid does indeed contain a peak in the same position that, importantly, is not present in the spectrum of HMF. Although this cannot be considered as concluding evidence, these observations suggest that the adsorbed matter should be chemically similar to the condensation products, and that the peak 1571 cm^{-1} correspond to an IR absorption connected to the newly forged carbon-carbon bond, that is, not present in the original HMF structure. This may also correspond to the acetone-derived carbon-oxygen double bond implemented. Yet another possibility is that adsorbed acetone itself or an enolate gives rise to this band [46,62,63]. The other signals (i. e. the ones related to C-C, C-H and O-H of the adsorbed molecules) are not visible on the HT_{rec} spectrum, likely covered by the intense HT peaks. Only a very small signal, perhaps connected to a C-O bond, can be detected in the fingerprint region, at ~ 1150 cm^{-1}. However, the intensity of this peak is so low that it might just be a disturbance in the baseline. Raman spectroscopy was also used to gather information about the organic matter deposited on the solid surface. The spectrum obtained after HT analysis presents peaks whose positions are in accordance with the previously reported data (Fig. S4) [64]: a peak at ~ 130 cm^{-1}, ascribed to a hydrogen-bonding stretching vibration; one at ~ 580 cm^{-1}, due to Al-O-Al and Al-O-Mg linkages; another one at ~ 1060 cm^{-1}, attributed to carbonate ν_1 symmetric stretching modes; a broad band centered at ~ 3500 cm^{-1}, in the area of OH stretching vibrations. On the other hand, the spectrum of HT_{rec} (as well as the spectra of all the other recovered catalysts) is dominated by fluorescence, which drowns out any Raman signal. Arguably, the deposited organic matter is the source of this

fluorescence. This issue together with the intrinsic low sensitivity of the technique are the reasons why Raman spectroscopy could not provide us with any information about the adsorbed species.

Degradation of the solids was performed by TGA coupled with MS. The TGA curve obtained for HT (Fig. 7) is in good agreement with the previously reported data [47]. The total mass loss at 1070 K is about 50 % which can be divided into two components: the first one, below 550 K, is attributed to the loss of physisorbed and inter-layer water, and a second one, above 550 K, is ascribed to dehydroxylation and decarboxylation of the solid. The MS analysis shows how CO_2 developed from HT gives rise to three different peaks corresponding to about 473, 623 and 723 K (Fig. S6). The curve obtained for HT_{rec} is analogous to the previous one. The total mass loss is however about 10 % greater than the one of HT, similarly to what has been observed for related systems [46]. More than introducing a distinct mass loss, the adsorbed matter is lost over a long range of temperatures above 573 K. This observation is backed up by the MS results, where the original CO_2 peaks of HT are covered by a broad peak ranging from 573 to 973 K.

N_2 physisorption results in previous reports show how the trend of the isotherms for HT-related materials depends on the catalyst preparation and, of course, on the degassing procedure [47,61,65,66]. In our case, the isotherm for HT (and for all other catalysts derived from it, Fig. 8) appear to belong to the Type III, that is, of solids that are non-porous, or possibly macroporous, and that have a low energy of adsorption [67]. Also, all isotherms present adsorption hysteresis. The hysteresis loops appear to belong to the Type H3, which is typical of clays composed of non-rigid aggregates of plate-like particles [67]. However, this type of narrow hysteresis loop with nearly parallel adsorption and desorption branches has also been attributed to Type H1 [61]. The obtained BET area for HT (Table 3, entry 1) is comparable to the ones in previous reports [47,61,65,66], although it appears to be somewhat higher than other reported values. A possible explanation for this is that oftentimes the reported HT-related catalysts have Mg:Al molar ratios of 3, whereas we used an HT with a ratio of 2: the surface area is high for a ratio of 2 like ours, and its value decreases when this ratio is increased [66]. BJH analysis of these sample shows how the parent HT is actually quite

a porous material (Table 3, entry 1), with a pore size right outside the range of mesopores (2 to 50 nm).

Temperature-programmed desorption was used to study the degradation of $[CO_3]^{2-}$ in the HT sample to CO_2. The TPD profile obtained (Fig. 9) very well matches the one of CO_2 in the TG-MS analysis of the same sample (Fig. S6). The different CO_2 signals arguably correspond to $[CO_3]^{2-}$ in three different chemical environments. CO_2 chemisorption studies, that is, TPD after adsorption of gaseous CO_2 are often used to obtain information on the basicity of a catalyst. Yet, in our case the presence of intense CO_2 degradation signals complicates the estimation of the CO_2 uptake. Besides, HT already has a fairly high level of CO_2 saturation given the amount of $[CO_3]^{2-}$ in its structure and the fact that HT is stored under air. Even so, some degree of exchange is expected, being HTs breathing materials [68]. Notwithstanding, an overall increase in the area of the CO_2 signals was detected (Table 3, entry 1). The N_2 physisorption and CO_2 chemisorption analyses were not performed on HT_{rec} (nor on any other recovered catalyst) since heating it at relatively low temperatures (as low as 353 K) seems to alter the composition of the surface-adsorbed species, which results in a color change of the solid to darker (brown) colors. Hence, it is not possible to properly outgas and dry out the solid without degrading the sample.

Lastly, HT was characterized by ICP-AES to obtain the total content of metals in the solid. It has been demonstrated that the sodium cation involved in the HT preparation, which may affect the outcome of the aldol condensation [65], is very difficult to wash away from the solid during the work-up. Nonetheless, the sodium content in samples from any batch of HT used for this study, independently prepared, is either very low or not detectable (Table 4), indicating successful HT washings. The Mg:Al molar ratios obtained by ICP-AES (2.35-2.36) are higher than the theoretical one based on the molar ratio of the salt precursors (which is 2), and are also substantially higher than the one measured by EDX. A possible, although tentative, explanation for this result is that while ICP-AES is performed on the digested sample as a whole, EDX just probes the surface of the sample (in the order of magnitude of 2-3 μm). Following this reasoning, it may be that at the early stages of

the co-precipitation an Mg-rich core is formed, whereas at the end of the co-precipitation the outer layer of the particles has an Mg:Al ratio that resembles the one of the precursors in the feeding solution.

3.3. Reaction selectivity

The reaction selectivities appeared to be quite stable throughout the optimization, with the C9:C15 product selectivity ratio about constant at 3:1-2:1 and the total selectivity to the aldol condensation products in the range of ~80-90 %. No other byproduct derived from HMF had been detected by GC-FID; adsorption of HMF-related compounds on the catalyst surface may account, at least partially, for the missing ~ 10-20 %. Small amounts of diacetone alcohol are detected, whereas no mesityl oxide is formed. Other analytical techniques were used to determine species in the reaction mixture in order to detect substances that do not burn in an FID detector (GC-MS), or compounds with higher molecular weights that are not volatile (HPLC-DAD and -TOF); nonetheless, final mixtures obtained at our reaction conditions do not appear to contain any additional byproduct in consistent amounts.

In addition to product selectivity, the stereoselectivity of the reaction was determined. C9 can exist in two diastereoisomeric forms, *Z* and *E* (or *cis* and *trans*); for C15, three configurations are possible, (*Z*,*Z*), (*E*,*E*) and two equivalent (*E*,*Z*) forms (or all *cis*, all *trans* and *cis*/*trans*). The *trans* forms are generally the most stable and favourable ones [69]. The stereoisomeric distribution of the products is important information, especially when the products are to be further modified (e. g. HDO). In the GC-FID chromatograms of our reaction mixtures only single peaks appear for C9 and C15, suggesting the presence of only one stereoconfiguration of each in the final reaction mixture [29]. NMR spectrometry may differentiate between diastereoisomers of the same compound and allow to quantify their ratio [70]. Thus, ^{1}H NMR spectroscopy was used to determine the ratio between the various diastereoisomers. The analysis of the products was performed on the reaction mixtures directly to avoid sample alteration. This method is convenient and straightforward as it

bypasses the removal of the reaction solvent and re-dissolution of the obtained solid in a deuterated solvent. The proton signals in the obtained spectra are well resolved despite the great number of inequivalent hydrogens in the mixture (Fig. 10). Details of the assignments are provided in the *Supplementary Information* (Section S5.3E). It can be noticed how only one set of signals for each product is present in the chemical shift area of arylic and olefinic protons. This implies that only one diastereoisomer of each compound is present in the final reaction mixture. Even in the fortuitous case that all analogous protons of the diastereoisomers were isochronous, at least the $^{3}J_{cis}$ and $^{3}J_{trans}$ coupling constants of the olefinic hydrogens should be different [25]; instead, only regular doublets are observed. The magnitude of the coupling constants related to the olefinic signals of both C9 and C15 (15-16 Hz) indicates that their stereoconfigurations are the *trans* and the all *trans* ones, respectively. This makes our process *E*-selective; the lack of stereoselectivity studies in previous reports does not permit us to understand conclusively if this is an exclusive feature of our and a few other systems [29,37]. The ^{1}H NMR study of our reaction mixtures also confirms that the quantity of diacetone alcohol formed is indeed very low considering that the reaction is performed neat (molar (HMF+C9+C15): diacetone alcohol of 43:1). An impurity that has signal pattern analogous to the one of HMF is detected in very low amounts; this impurity is also present in the commercial HMF that was used as a reactant (Fig. S23) and has been identified as an HMF degradation dimer, also known as cirsiumaldehyde, based on spectra in previous reports [14].

3.4. Catalyst comparison

The catalyst choice proved to have a remarkable influence on the reaction outcome. Upon calcination the shape of the diffractogram changed dramatically with the loss of the LDH structure (Fig. 4). The new peaks correspond to the diffraction lines of the MgO cubic phase [71]. On the other hand, TEM analysis shows how the morphology of the solid does not undergo substantial changes (Fig. 5f). All of the $[OH]^{-}$, H_2O and $[CO_3]^{2-}$ related peaks in the HT FT-IR spectrum disappear as a

result of calcination (Fig. 6). Only an intense and broad band below 1100 cm^{-1} is present, which can be assigned to vibration modes for M-O in the solid [47]. In the Raman spectrum of this solid the LDH peaks also disappear to be substituted by two broad peaks at ~ 1500 and 2000 cm^{-1} (Fig. S4). In the thermogravimetric analysis of the solid, the mass of MMO slowly decreases to 80 % of its original value (Fig. 7); this mass loss is not associated with the formation of CO_2 (Fig. S6). It is commonly observed that the surface area sharply increases when as-synthesized HTs are calcined to MMOs [47,65,66]; our catalyst is no exception (Table 3, entry 2). MMO has a porosity similar to HT, but much smaller pores. Given its higher surface area and its stronger basicity character, the MMO obtained after calcination of HT should in principle exhibit a higher activity in aldol condensations than its parent catalyst [46]. TPD degradation study of MMO corroborates the absence of $[CO_3]^{2-}$ in its structure (Fig. 9). Furthermore, the CO_2 chemisorption analysis suggests that MMO has a more pronounced basicity than its parent catalyst (Table 3, entry 2), although the very different type of basicity and composition of the two solids makes the results not comparable. Quite surprisingly, the activity of the freshly-calcined MMO proved to be remarkably lower than the one of as-synthesized HT (Table 5, entry 2).

The as-synthesized HTs contain counter-anions such as $[OH]^-$, $[CO_3]^{2-}$ and $[NO_3]^-$ in their inter-layer space that neutralize the positive charges of the LDH. The basicity of each anion is different; therefore, their distribution in the solid would in principle affect the activity of the catalyst as a whole. In particular, $[NO_3]^-$, which derives from the starting salt precursors, is less basic than $[CO_3]^{2-}$. For this reason, we prepared and tested the reactivity of an HT containing only carbonate as a counter-anion. This catalyst (HT_{reg}) was prepared by exploiting the memory properties of HTs: the freshly-calcined HT was immersed in a 1 M aqueous solution of Na_2CO_3 for the MMO to sorb water and carbonates, and to recover its original LDH structure (Fig. 4) [44]. The carbon percentage seems to increase from HT to HT_{reg} (Table 2, entry 3), but this increase may not be significant considering the low intensity of the carbon EDX signal (Fig. S3). The FT-IR spectrum of HT_{reg} does not appear to be appreciably different from the one of its parent catalyst (Fig. 6); the same consideration applies

to the Raman spectrum (Fig. S4). The TGA curve of HT_{reg} also is very similar to the one of HT, with just a slightly higher total mass loss (Fig. 7); the MS results also are quite similar (Fig. S6). Importantly, in neither the analysis of HT nor in the one of HT_{reg} was detected any formation of NO_x, suggesting that the amount of nitrates in HT, as compared to carbonates, is negligible. The obtained BET surface area (Table 3, entry 3) is higher than the one of HT, but lower than the one of MMO; porosity and pore size of HT_{reg} are comparable to the ones of HT. Nevertheless, the catalytic activity lost upon calcination is partially recovered as the resulting conversion of the aldol condensation with HT_{reg} (Table 5, entry 3) is quite higher than the one obtained with MMO. This confirms that HT as a Brønsted-basic LDH is a more active catalyst than its calcined, Lewis-basic MMO form. On the other hand, HT_{reg} proved to be less active for the transformation than the original, as-synthesized HT. This may be due to irreversible structural modifications during calcination, and an incomplete LDH structure reconstruction.

In order to boost up the Brønsted basicity of our LDH, we swapped the carbonate counter-anions for hydroxyls. To do this, the freshly calcined MMO was immersed in Ar-bubbled, carbonate-free deionized water, where the only anions contained are indeed hydroxyl ones. The rehydration was successful and the LDH structure was restored (as confirmed by PXRD, Fig. 4) but, despite these precautions, the obtained MX ended up incorporating carbon in its structure. The C content obtained by EDX analysis is even higher than the one of the original HT, albeit only slightly so (Table 2, entry 4). FT-IR analysis revealed that this carbon is in the form of carbonate: a sharp peak which can be ascribed to a $[CO_3]^{2-}$ ν_3 is present (Fig. 6). In point of fact, the FT-IR spectra of MX prepared with procedures similar to ours also include the $[CO_3]^{2-}$ ν_3 peak [47,66,72]. Since MMO, its precursor, do not seem to include carbonates, the reintroduction of $[CO_3]^{2-}$ has likely happened in the work-up step, highlighting the importance of avoiding contact with air. The rest of the MX spectrum is also analogous to the HT one. Differences in the two spectra lie in the different pattern of the M-OH translations (below 1100 cm^{-1}). This difference may be due to the high hydroxyl content of MX as compared to HT. In this spectral region, a peak at 935 cm^{-1} appears. It should be noticed, however,

that for HT an inflection point is present at this same position. The Raman spectrum of MX resembles very much the one of the HT as well (Fig. S4). The two spectra differ in the presence of the peak at ~ 130 cm^{-1} (which is absent in the MX spectrum), and in the relative intensity of the peaks at ~ 560 and 1060 cm^{-1} (corresponding to Al-O-Al and Al-O-Mg linkages and $[CO_3]^{2-}$ ν_1 symmetric stretching, respectively). The TGA curve of MX (Fig. 7) is similar to the one of HT, although the profile appears to be somewhat different, in agreement with previously reported results [46,47]. The MS results from TGA corroborates the presence of carbonates in the solid (Fig. S6). Other proofs are provided by temperature-programmed desorption of MX: the TPD degradation profile of this catalyst matches its CO_2 MS profile and the previously reported TPD profile of the same catalyst after CO_2 adsorption (Fig. 9) [47]. The calculated CO_2 uptake for MX is lower than the one of MMO and the ones in the literature (Table 3, entry 4) [47]. Besides being dependent on the TPD analysis conditions, this result is unreliable: the outcome is greatly affected by how long MX has been in contact with air (which may also influence the activity of the said catalyst [46]); assuming that before work up MX did not contain any carbonate, the CO_2 uptake after the preparation was about 415 μmol/g. This result also shows the importance of performing a TPD degradation study together with the actual CO_2 chemisorption experiment for properly calculating the net uptake. The surface area of MX, whose N_2 physisorption properties very much depend on the synthesis conditions [66], is the lowest among the catalysts tested so far (Table 3, entry 4). Additionally, MX has also a considerably lower porosity and higher pore size. Nonetheless, MX exhibited a very high catalytic activity in our system (Table 5, entry 4), leading to almost complete conversion after 10 minutes of irradiation with a 5:1 HMF:MX ratio.

In all cases, LDHs performed better than the MMO. It is unclear whether the reason for this lies in the fact that Brønsted basicity is more suitable than Lewis basicity for the catalysis of the aldol condensation at our reaction conditions, or that the catalyst structural differences make LDHs better microwave absorbers (e. g. the ordered layered structure or the presence of inter-layer water aid the formation of hotspots in the solid catalyst). In any case, the reaction selectivity does not seem to be

influenced much by the catalyst choice despite the different activities observed with different catalysts.

Na_2CO_3 and NaOH, which are used in the HT co-precipitation, are both solid bases. In order to get an insight into the possible impact of sodium carbonate and hydroxide contained as impurities in the final catalysts, they were also tested as heterogeneous catalysts. Notably, Na_2CO_3 proved to be a completely inactive catalyst for the transformation at our reaction conditions (Table 5, entry 5). Conversely, NaOH was very active (Table 5, entry 6), and other products in addition to the usual C9 and C15 were observed. Particularly worth noting was the presence, in high concentration, of the condensation products of C9 and acetone in the reaction mixture, as confirmed by GC-MS (Section S5.3B). The formation of this byproduct, C12, is favoured as the consecutive product of C9 over C15, which is just barely detected. Having said that, the Na content of any catalyst was below the detection limit of the EDX elemental analysis, and ICP-AES analysis of the parent HT only showed trace amounts of Na in the solid. Therefore, in all likelihood neither sodium carbonate nor sodium hydroxide have contributed to the activity of our catalysts.

3.5. Catalyst recycle

An important feature of a catalyst is its ability to be reused in subsequent processes. For this reason, different forms of catalyst recycle have been tested. The most convenient catalyst recycle method is the direct reuse of these recovered catalysts, HT_{rec}, MMO_{rec} and MX_{rec}, meaning that the used catalyst is loaded into another reaction mixture without further treatment. Yet, none of the recovered catalysts showed significant activity under our optimized conditions (Table 6, entries 1-3). These results indicate that the aldol condensation process causes catalyst poisoning. Undergoing reaction catalysis does not seem to bring about significant changes to the solid structure of HT_{rec}, and the same applies to MMO_{rec} and MX_{rec} (Fig. 4). In contrast, as previously mentioned, the used, de-activated catalysts appear visibly different at the end of the reaction, as their colour change from white before the reaction to yellow-brown after recovery. The increase of the carbon content from MX to

MX_{rec} appears to be significant (Table 2, entry 5). Changes in the composition of the solids after catalysis are detected by FT-IR, too (Fig. 6). The spectrum of MMO_{rec} resembles the one of its precursors, although peaks in the region above 1100 cm^{-1} appear. It has been previously demonstrated that adsorption of H_2O and CO_2 on calcined hydrotalcites gives rise to adsorption bands at ~ 3500 cm^{-1} and 1200-1900 cm^{-1}, respectively [73]. The peak at 1571 cm^{-1}, observed in the spectrum of HT_{rec}, is not detectable. However, this peak may not be visible as a result of overlapping with the carbonate/bicarbonate band. Other reasons for this may be the low conversion obtained with the MMO (namely, the low concentration of C9 and C15 in the reaction mixtures which perhaps are the main responsible of the poisoning), and the fact MMO is a different type of catalyst and may undergo a different deactivation pathway (it was previously demonstrated that solids analogous to our MMO_{rec} are still catalytically active at different reaction conditions [29]). Moreover, a small peak at ~ 1150 cm^{-1}, arguably connected to a C-O signal, can be detected together with another small peak at ~ 1000 cm^{-1}. On the other hand, in the spectrum of MX_{rec} the peak at 1571 cm^{-1} is present, together with the aforementioned less intense peaks at ~ 1150 and ~ 1000 cm^{-1}. The TGA curve of MMO_{rec}, when compared with the one of MMO, vividly shows how the mass loss connected to the adsorbed organic matter is spread over a range of temperatures (Fig. 7). The profile of the MX_{rec} curve is more similar to the one of HT than to MX; this phenomenon has been observed also in previous reports [46]. The CO_2 MS signals for MMO_{rec} and MX_{rec} are both broad and analogous to the ones of HT_{rec} (Fig. S6).

The catalyst de-activation implies that a regeneration, the second recycle method, is required for catalyst recycle. All regenerations started with a calcination to remove the deposited organic matter. Of course, while the calcined MMO_{rec} can be reused as it is (MMO'), high-temperature treatment of an LDH causes structural collapse and requires reconstruction. This was achieved by immersion of the freshly-calcined MMO in a suitable aqueous solution, which restores the original structure (HT'$_{reg}$ and MX') much like it did for the preparation of the original catalysts (HT_{reg} and MX).

The catalysts obtained with this procedure showed lower or comparable activity to the original ones (HT'$_{reg}$ and MMO', Table 6, entries 4 and 5 respectively) and, to our delight, MX' showed almost identical activity to MX (entry 6). In this case, the reaction selectivity is substantially unaffected by the use of a recycled catalyst. It should be noted that the catalyst recovery procedure does not allow complete recovery of the loaded solid after reaction, mostly due to fine catalyst powder sticking to the walls of the tubes. The reported results are the average of the outcomes of five independent reactions and, for this reason, it was impossible to obtain enough catalyst for five tests from the previous five. Nevertheless, the reported reaction outcome is the result of the catalysis by a solid prepared with 80% of MX' from the previous run, and 20% of MX' prepared after another run performed earlier on. Thus, the solid used was formally a 100% MX'.

The used MX' was recovered after reaction and regenerated a second time to afford MX''. In this instance, given the lack of solid, the catalyst used was composed of 80% of MX'' prepared by regeneration of MX'$_{rec}$ from the previous run, and 20% of MX'. This solid proved to be quite active as well, albeit the conversion was somewhat lower (Table 6, entry 7). This may be the result of irreversible structural changes after recycle, which only makes sense considering that MX'' has undergone overall 3 cycles of calcination-rehydration. Yet, the PXRD analysis of MX''$_{rec}$, the final recovered solid, shows how it still possesses the original LDH structure (Fig. 4). The "desert rose"-like morphology is also still present (Fig. 5c). The TGA curve of this solid is similar to the one of MX$_{rec}$ (Fig. 7), and so are the results of the MS analysis (Fig. S6).

4. Conclusions

We have developed a protocol that can be used to convert rapidly HMF and acetone into their aldol condensation products. The use of LDHs at our reaction conditions pushes the boundary of how fast HMF could be converted into C9 and C15 in a selective fashion over a heterogeneous catalyst so far. Moreover, our protocol makes use of relatively low amounts of a catalyst made up of earth-abundant atoms that can be recycled. Our premier result is an average of a 96% conversion with an

89% total selectivity towards the desired enones obtained from five parallel reactions of 0.1 g of HMF (for a total of 0.5 g) in 5 mL of acetone (for a total of 25 mL) catalysed by 0.02 g of MX (for a total of 0.1 g) in 10 minutes of irradiation at 300 W (plus 20 minutes of no irradiation), that is, spending 0.18 MJ.

Heterogeneous catalysts like LDHs and MMOs are not corrosive and can be easily recovered from the reaction mixture. Aided by the results of the catalyst characterization, we developed a protocol that regenerates our deactivated catalysts. However, our recycle procedure is not optimal, as it is effective but energy-consuming, and its efficacy appears to decrease when repeated multiple times. Besides, the moderate basicity of our catalysts as compared to the very strong basicity of species such as NaOH improves overall selectivity towards the cross-aldol condensation products by minimizing the formation of the solvent self-condensation products (diacetone alcohol and mesityl oxide), cross-condensation byproducts (C12) and other compounds.

Unfortunately, none of our catalysts proved to have a consistent effect on the C9:C15 selectivity, unlike other reported catalysts that managed to shift this proportion by virtue of specific features of the solid structure (e. g. catalysts with hierarchical structures and surface modifications) [36]. Reaching the desired degree of C9:C15 selectivity with our protocol shall then be achieved by conventional optimization of HMF concentration and/or HMF:acetone ratio using a solvent [22]. Nevertheless, the overall high selectivity towards the cross-condensation products and the ease of separation of the two by means of the very different solubility of C9 and C15 in water [22] make our protocol a useful strategy for the *E*-selective preparation of these bio-derived monomers and dyes and for the synthesis of linear alkanes with targeted chain lengths.

One of the most important advantages of our protocol is that as-synthesized hydrotalcite is quite an active catalyst for the aldol condensation at our reaction conditions. HTs have a very straightforward preparation and are not as much sensitive to air as MMOs and MXs; as a matter of fact, the HT used for experiments had been stored in a vial under air for more than one year and still keeps its activity. HTs are generally not even considered and tested as catalysts in analogous

condensation processes, or perform poorly and require activation. Activation by calcination and rehydration of HTs is a lengthy procedure and intrinsically reduce the energy efficiency of the process.

Conflicts of interest

There are no conflicts to declare.

Acknowledgements

A.T. thanks AGAUR (Generalitat de Catalunya) and ESF (European Union) for his postgraduate scholarship (2018 FI_B 01124). F. M. and M. C. thank the Ministerio de Economía y Competitividad for financial support (RTI2018-098310-B-I00). A. Dafinov and the technicians of the Servei de Recursos Científics i Tècnics of URV are gratefully acknowledged for assistance in the characterizations.

Tables

Table 1. Optimization results. {To be put in a double column space}

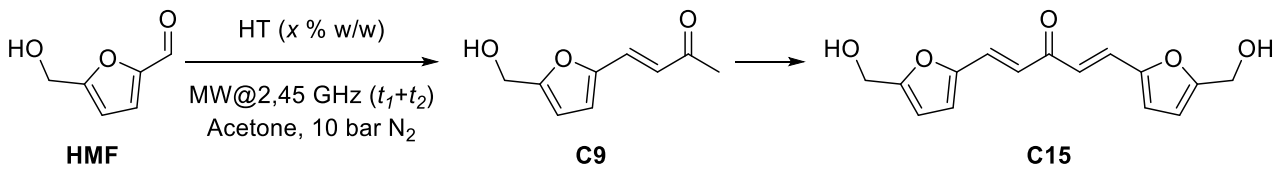

Entry	Loading [*x* % w/w]	t_1 [min]	t_2 [min]	Conv. HMF [%]	Sel. C9 [%]	Sel. C15 [%]
1	50	10	20	> 99	58	20
2	50	10	0	91	58	26
3	50	0	10	93	60	27
4	20	0	10	71	63	29
5	0	0	10	< 1	n.d.	n.d.

Table 2. Results of the elemental analysis from EDX data. {To be put in a double column space}

Entry	Sample	C		O		Mg		Al		Mg/Al
		[wt %]	[at %]	[wt %]	[at %]	[wt %]	[at %]	[wt %]	[at %]	[at/at]
1	HT	4.05	6.16	59.59	67.97	19.08	14.31	11.60	7.85	1.83
2	HT_{rec}	5.43	8.12	59.89	67.23	21.43	15.83	13.27	8.83	1.80
3	HT_{reg}	4.98	7.46	60.02	67.57	21.98	16.30	11.91	7.95	2.05
4	MX	4.41	6.60	61.11	68.79	21.84	16.18	12.65	8.44	1.92
5	MX_{rec}	9.97	14.57	56.98	62.55	19.38	14.00	12.56	8.18	1.72

Table 3. Obtained N_2 physisorption and CO_2 chemisorption data for HT, MMO, HT_{reg} and MX. {To be put in a double column space}

Entry	Catalyst	S_{BET} [m^2/g]	V_{pore} [mL/g]	r_{pore} [Å]	C_{basic} [μmol/g]
1	HT	109.028	0.835	62.799	42.170
2	MMO	179.018	0.842	18.650	170.046
3	HT_{reg}	140.667	0.789	51.098	/
4	MX	70.088	0.583	89.410	69.043

Table 4. Content of Mg, Al and Na of two different HT batches prepared independently, obtained by ICP-AES. {To be put in a single column space}

Sample	Mg [w/w %]	Al [w/w %]	Na [w/w %]	Mg/Al [at/at]
HT	22.3	10.5	n.d.	2.35
HT_{bis}	22.0	10.3	0.0014	2.36

Table 5. Comparison of catalyst performances. {To be put in a single column space}

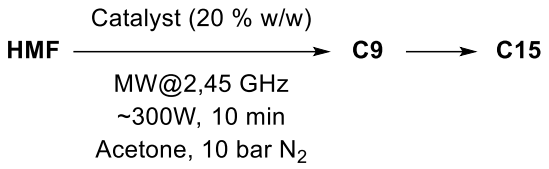

Entry	Catalyst	Conv. HMF [%]	Sel. C9 [%]	Sel. C15 [%]
1	HT	71	63	29
2	MMO	22	64	19
3	HT_{reg}	52	59	25
4	MX	96	64	25
5	Na_2CO_3	< 1	n.d.	n.d.
6	NaOH	> 99	51	< 1

Table 6. Recycle potential of the prepared catalysts. {To be put in a single column space}

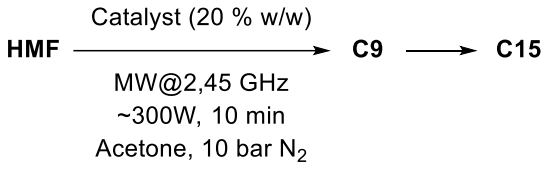

Entry	Catalyst	Conv. HMF [%]	Sel. C9 [%]	Sel. C15 [%]
1	HT_{rec}	< 1	n.d.	n.d.
2	MMO_{rec}	< 1	n.d.	n.d.
3	MX_{rec}	< 1	n.d.	n.d.
4	HT'_{reg}	37	58	16
5	MMO'	19	50	n.d.
6	MX' [a]	94	64	28
7	MX'' [b]	86	69	30

[a] Composed of 80% of regenerated MX_{rec} from the test in Table 5, entry 4 and 20% of regenerated MX_{rec} from an analogous test. [b] Composed of 80% of regenerated MX'_{rec} from the test in this table, entry 6 and 20% of regenerated MX_{rec} from an analogous test.

Figures

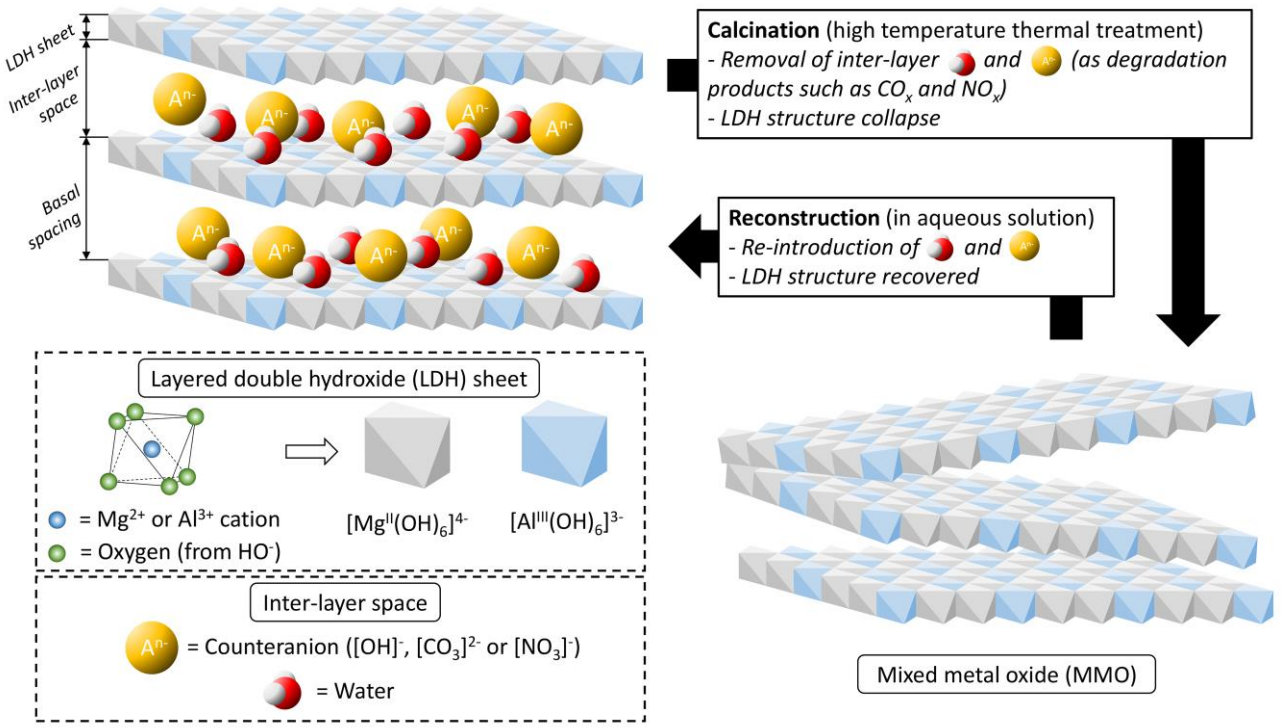

Fig. 1. Overview of structure and composition of HT-like materials, and their structure-memory behaviour. {To be put in a double column space}

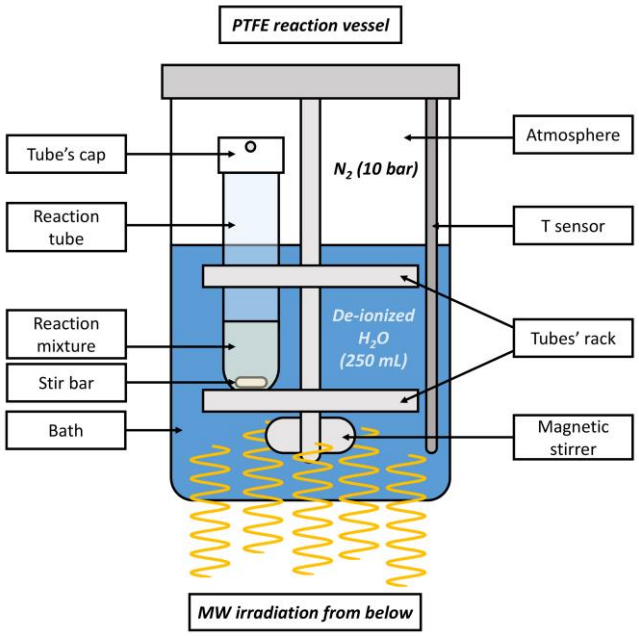

Fig. 2. Schematic representation of the reaction setup. {To be put in a single column space}

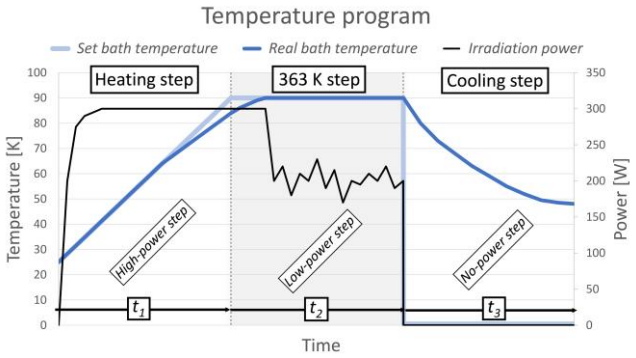

Fig. 3. Bath temperature program and power irradiation over time in MW-assisted experiments. {To be put in a single column space}

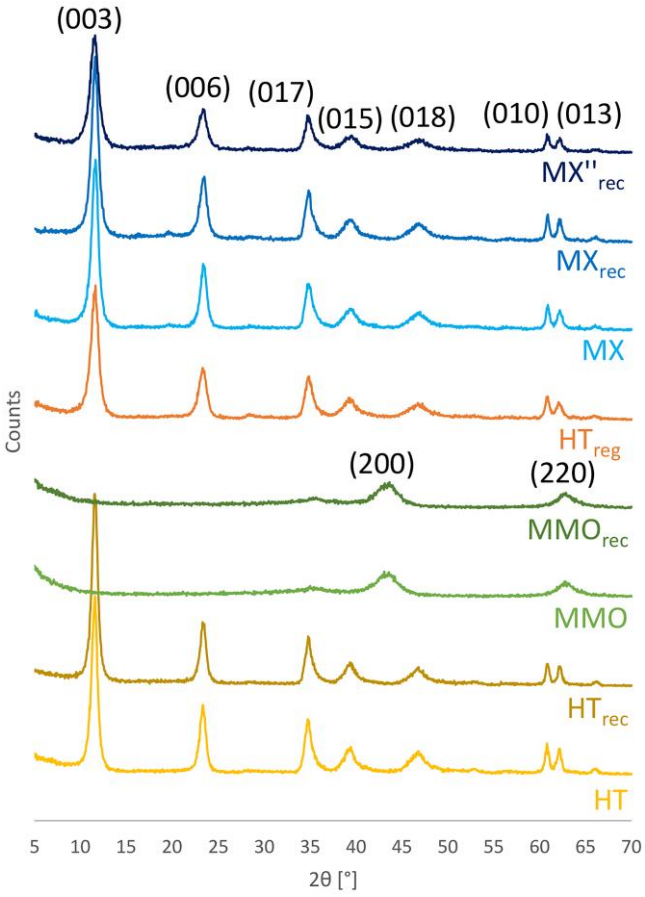

Fig. 4. X-ray diffractograms of solid catalysts before and after reaction. {To be put in a single column space}

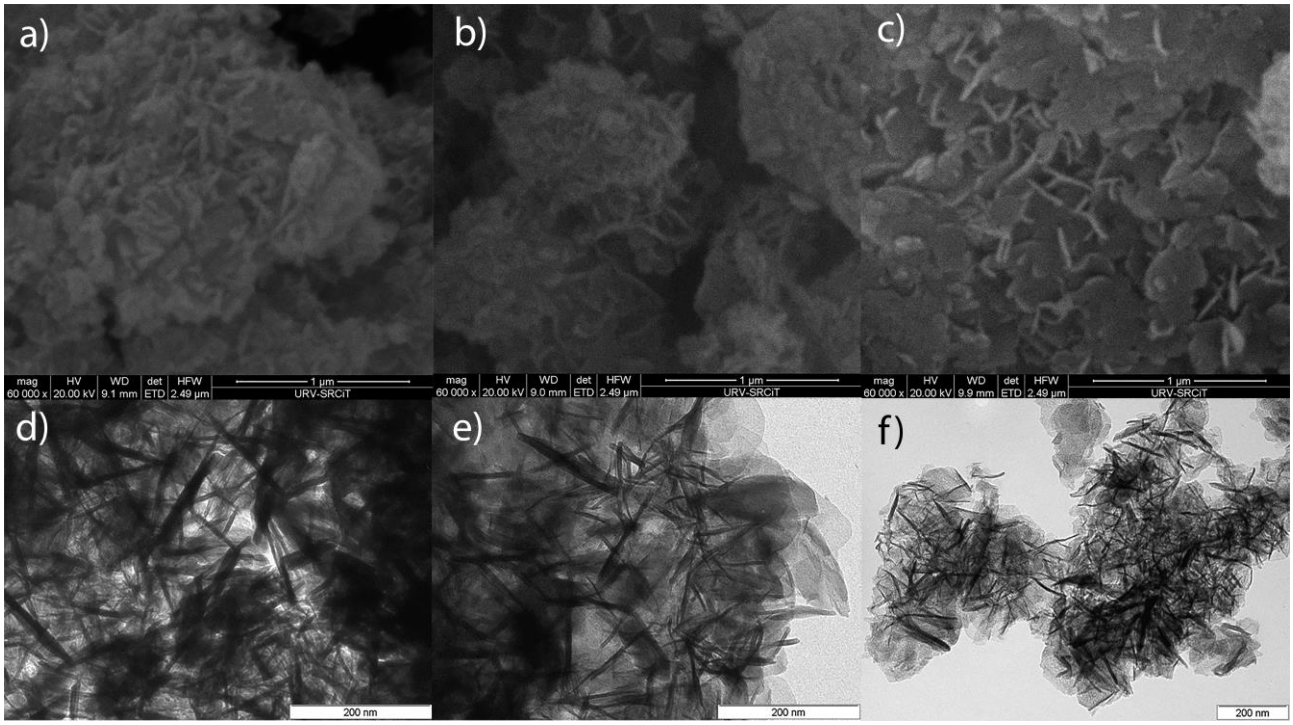

Fig. 5. ESEM micrographs at 60 K of HT (a), HT_{rec} (b) and MX''_{rec} (c). TEM micrographs at 100 K of HT (d), HTrec (e) and MMO (f). {To be put in a double column space}

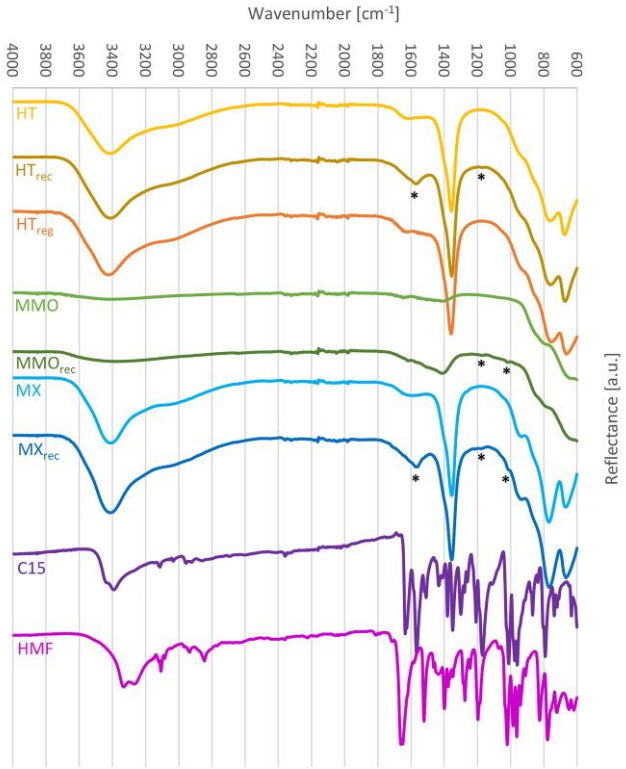

Fig. 6. FT-IR spectra of solid catalysts before and after reaction, and of C15 and HMF. {To be put in a single column space}

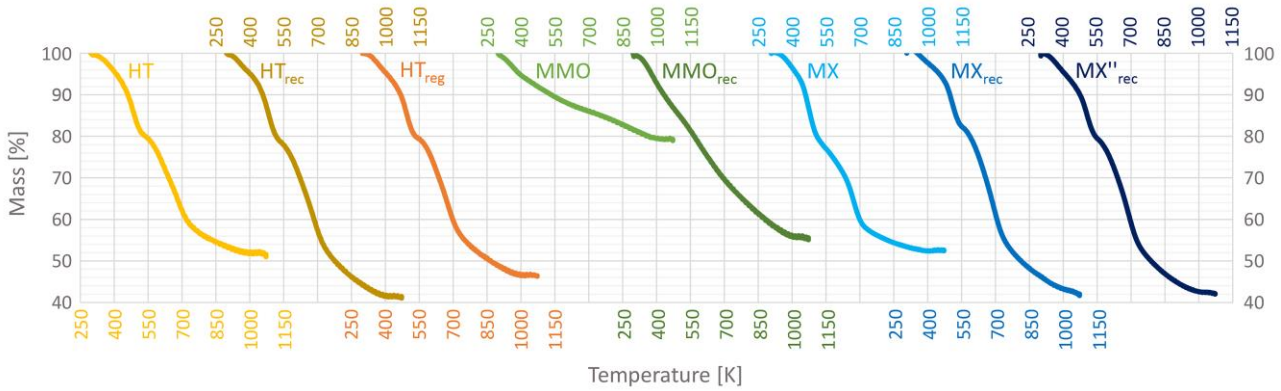

Fig. 7. TGA curves of solid catalysts before and after reaction. {To be put in a double column space}

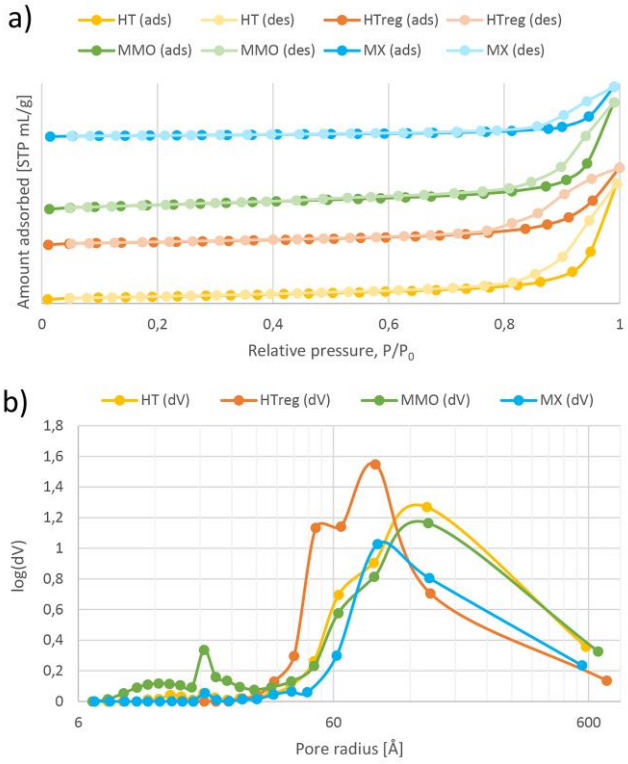

Fig. 8. a) Isotherms of N_2 adsorption-desorption and b) BJH pore size distributions of solid catalysts. {To be put in a single column space}

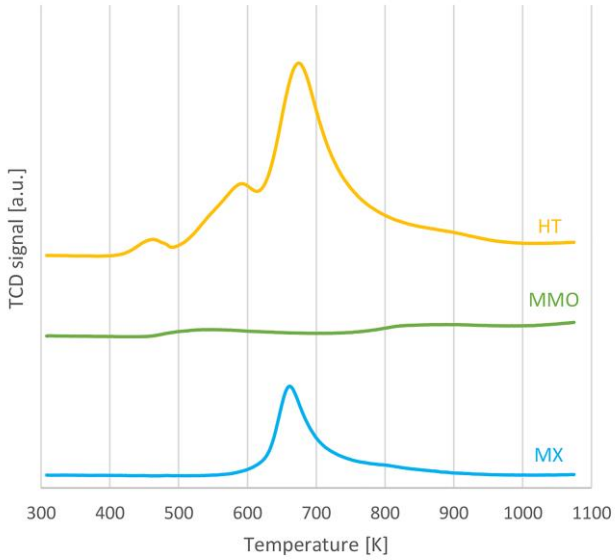

Fig. 9. TPD-CO_2 degradation profiles of HT, MMO and MX.

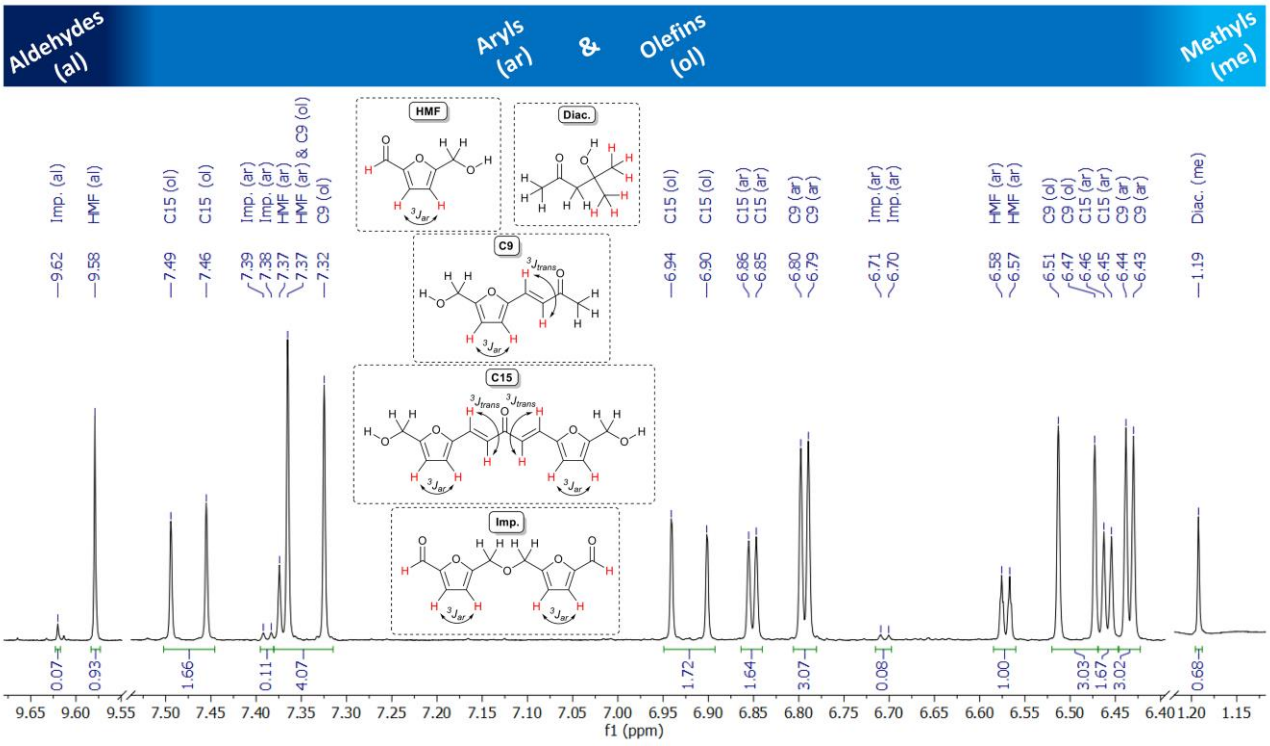

Fig. 10. Liquid-phase ^{1}H NMR spectrum of the final reaction mixture with the characteristic peaks useful for their determination. The ordinate is an arbitrary NMR signal intensity. ^{1}H-NMR (400 MHz, no-D acetone) HMF δ 9.58 (s, 1H), 7.37 (d, $^3J_{ar}$ = 3.6 Hz, 1H), 6.58 (d, $^3J_{ar}$ = 3.6 Hz, 1H); C9 δ 7.34

(d, $^{3}J_{trans}$ = 16.1 Hz, 1H), 6.79 (d, $^{3}J_{ar}$ = 3.4 Hz, 1H), 6.49 (d, $^{3}J_{trans}$ = 16.1 Hz, 1H), 6.43 (d, $^{3}J_{ar}$ = 3.4 Hz, 1H); C15 δ 7.48 (d, $^{3}J_{trans}$ = 15.6 Hz, 2H), 6.92 (d, $^{3}J_{trans}$ = 15.7 Hz, 2H), 6.85 (d, $^{3}J_{ar}$ = 3.3 Hz, 2H), 6.46 (d, $^{3}J_{ar}$ = 3.3 Hz, 2H); Imp. δ 9.62 (s, 2H), 7.39 (d, $^{3}J_{ar}$ = 3.5 Hz, 2H), 6.58 (d, $^{3}J_{ar}$ = 3.5 Hz, 2H); Diac. δ 1.19 (s, 6H). {To be put in a double column space}

References

[1] I. Capellán-Pérez, M. Mediavilla, C. de Castro, Ó. Carpintero, L.J. Miguel, Fossil fuel depletion and socio-economic scenarios: An integrated approach, Energy 77 (2014) 641–666. https://doi.org/10.1016/j.energy.2014.09.063.

[2] M. Höök, X. Tang, Depletion of fossil fuels and anthropogenic climate change—A review, Energy Policy 52 (2013) 797–809. https://doi.org/10.1016/j.enpol.2012.10.046.

[3] R. Ahorsu, F. Medina, M. Constantí, Significance and challenges of biomass as a suitable feedstock for bioenergy and biochemical production: A review, Energies 11 (2018) 3366. https://doi.org/10.3390/en11123366.

[4] A. Corma, S. Iborra, A. Velty, Chemical routes for the transformation of biomass into chemicals, Chemical reviews 107 (2007) 2411–2502. https://doi.org/10.1021/cr050989d.

[5] D. Esposito, M. Antonietti, Redefining biorefinery: the search for unconventional building blocks for materials, Chemical Society reviews 44 (2015) 5821–5835. https://doi.org/10.1039/C4CS00368C.

[6] J.N. Chheda, G.W. Huber, J.A. Dumesic, Liquid-phase catalytic processing of biomass-derived oxygenated hydrocarbons to fuels and chemicals, Angewandte Chemie (International ed. in English) 46 (2007) 7164–7183. https://doi.org/10.1002/anie.200604274.

[7] Z. Ma, L. Wei, W. Zhou, L. Jia, B. Hou, D. Li, Y. Zhao, Overview of catalyst application in petroleum refinery for biomass catalytic pyrolysis and bio-oil upgrading, RSC Adv. 5 (2015) 88287–88297. https://doi.org/10.1039/c5ra17241a.

[8] M. Dusselier, M. Mascal, B.F. Sels, Top chemical opportunities from carbohydrate biomass: a chemist's view of the Biorefinery, Topics in current chemistry 353 (2014) 1–40. https://doi.org/10.1007/128_2014_544.

[9] L.T. Mika, E. Cséfalvay, Á. Németh, Catalytic conversion of carbohydrates to initial platform chemicals: Chemistry and sustainability, Chemical reviews 118 (2018) 505–613. https://doi.org/10.1021/acs.chemrev.7b00395.

[10] C.-H. Zhou, X. Xia, C.-X. Lin, D.-S. Tong, J. Beltramini, Catalytic conversion of lignocellulosic biomass to fine chemicals and fuels, Chemical Society reviews 40 (2011) 5588–5617. https://doi.org/10.1039/C1CS15124J.

[11] G.W. Huber, R.D. Cortright, J.A. Dumesic, Renewable alkanes by aqueous-phase reforming of biomass-derived oxygenates, Angewandte Chemie (International ed. in English) 43 (2004) 1549–1551. https://doi.org/10.1002/anie.200353050.

[12] R.M. West, Z.Y. Liu, M. Peter, J.A. Dumesic, Liquid alkanes with targeted molecular weights from biomass-derived carbohydrates, ChemSusChem 1 (2008) 417–424. https://doi.org/10.1002/cssc.200800001.

[13] J.G. de Vries, Green syntheses of heterocycles of industrial importance. 5-hydroxymethylfurfural as a platform chemical, in: Heterocyclic Chemistry in the 21st Century - A Tribute to Alan Katritzky, Elsevier, 2017, pp. 247–293.

[14] K.I. Galkin, E.A. Krivodaeva, L.V. Romashov, S.S. Zalesskiy, V.V. Kachala, J.V. Burykina, V.P. Ananikov, Critical influence of 5-hydroxymethylfurfural aging and decomposition on the utility of biomass conversion in organic synthesis, Angewandte Chemie (International ed. in English) 55 (2016) 8338–8342. https://doi.org/10.1002/anie.201602883.

[15] K.I. Galkin, V.P. Ananikov, Towards improved biorefinery technologies: 5-methylfurfural as a versatile C6 platform for biofuels development, ChemSusChem 12 (2019) 185–189. https://doi.org/10.1002/cssc.201802126.

[16] K.I. Galkin, V.P. Ananikov, When will 5-hydroxymethylfurfural, the "Sleeping giant" of sustainable chemistry, awaken?, ChemSusChem 12 (2019) 2976–2982. https://doi.org/10.1002/cssc.201900592.

[17] X. Kong, Y. Zhu, Z. Fang, J.A. Kozinski, I.S. Butler, L. Xu, H. Song, X. Wei, Catalytic conversion of 5-hydroxymethylfurfural to some value-added derivatives, Green Chem. 20 (2018) 3657–3682. https://doi.org/10.1039/c8gc00234g.

[18] G.J. Kelly, F. King, M. Kett, Waste elimination in condensation reactions of industrial importance, Green Chem. 4 (2002) 392–399. https://doi.org/10.1039/B201982P.

[19] L. Wu, T. Moteki, A.A. Gokhale, D.W. Flaherty, F.D. Toste, Production of fuels and chemicals from biomass: Condensation reactions and beyond, Chem 1 (2016) 32–58. https://doi.org/10.1016/j.chempr.2016.05.002.

[20] J.C. Serrano-Ruiz, J.A. Dumesic, Catalytic routes for the conversion of biomass into liquid hydrocarbon transportation fuels, Energy Environ. Sci. 4 (2011) 83–99. https://doi.org/10.1039/c0ee00436g.

[21] A.D. Sutton, F.D. Waldie, R. Wu, M. Schlaf, L.A.P. Silks, J.C. Gordon, The hydrodeoxygenation of bioderived furans into alkanes, Nature chemistry 5 (2013) 428–432. https://doi.org/10.1038/NCHEM.1609.

[22] H. Chang, A.H. Motagamwala, G.W. Huber, J.A. Dumesic, Synthesis of biomass-derived feedstocks for the polymers and fuels industries from 5-(hydroxymethyl)furfural (HMF) and acetone, Green Chem. 21 (2019) 5532–5540. https://doi.org/10.1039/c9gc01859j.

[23] H. Gruber, P. Groß, R. Rauch, A. Reichhold, R. Zweiler, C. Aichernig, S. Müller, N. Ataimisch, H. Hofbauer, Fischer-Tropsch products from biomass-derived syngas and renewable hydrogen, Biomass Conv. Bioref. 48 (2019) 22. https://doi.org/10.1007/s13399-019-00459-5.

[24] H. Zang, K. Wang, M. Zhang, R. Xie, L. Wang, E.Y.-X. Chen, Catalytic coupling of biomass-derived aldehydes into intermediates for biofuels and materials, Catal. Sci. Technol. 8 (2018) 1777–1798. https://doi.org/10.1039/c7cy02221b.

[25] L. Faba, E. Díaz, S. Ordóñez, Aqueous-phase furfural-acetone aldol condensation over basic mixed oxides, Applied Catalysis B: Environmental 113-114 (2012) 201–211. https://doi.org/10.1016/j.apcatb.2011.11.039.

[26] R.M. West, Z.Y. Liu, M. Peter, C.A. Gärtner, J.A. Dumesic, Carbon–carbon bond formation for biomass-derived furfurals and ketones by aldol condensation in a biphasic system, Journal of Molecular Catalysis A: Chemical 296 (2008) 18–27. https://doi.org/10.1016/j.molcata.2008.09.001.

[27] G.W. Huber, J.N. Chheda, C.J. Barrett, J.A. Dumesic, Production of liquid alkanes by aqueous-phase processing of biomass-derived carbohydrates, Science (New York, N.Y.) 308 (2005) 1446–1450. https://doi.org/10.1126/science.1111166.

[28] W. Shen, G.A. Tompsett, K.D. Hammond, R. Xing, F. Dogan, C.P. Grey, W.C. Conner, S.M. Auerbach, G.W. Huber, Liquid phase aldol condensation reactions with MgO–ZrO2 and shape-selective nitrogen-substituted NaY, Applied Catalysis A: General 392 (2011) 57–68. https://doi.org/10.1016/j.apcata.2010.10.023.

[29] J. Cueto, L. Faba, E. Díaz, S. Ordóñez, Performance of basic mixed oxides for aqueous-phase 5-hydroxymethylfurfural-acetone aldol condensation, Applied Catalysis B: Environmental 201 (2017) 221–231. https://doi.org/10.1016/j.apcatb.2016.08.013.

[30] C.J. Barrett, J.N. Chheda, G.W. Huber, J.A. Dumesic, Single-reactor process for sequential aldol-condensation and hydrogenation of biomass-derived compounds in water, Applied Catalysis B: Environmental 66 (2006) 111–118. https://doi.org/10.1016/j.apcatb.2006.03.001.

[31] K. Pupovac, R. Palkovits, Cu/MgAl(2)O(4) as bifunctional catalyst for aldol condensation of 5-hydroxymethylfurfural and selective transfer hydrogenation, ChemSusChem 6 (2013) 2103–2110. https://doi.org/10.1002/cssc.201300414.

[32] A. Bohre, B. Saha, M.M. Abu-Omar, Catalytic upgrading of 5-hydroxymethylfurfural to drop-in biofuels by solid base and bifunctional metal-acid catalysts, ChemSusChem 8 (2015) 4022–4029. https://doi.org/10.1002/cssc.201501136.

[33] J.D. Lewis, S. van de Vyver, Y. Román-Leshkov, Acid-base pairs in Lewis acidic zeolites promote direct aldol reactions by soft enolization, Angewandte Chemie (International ed. in English) 54 (2015) 9835–9838. https://doi.org/10.1002/anie.201502939.

[34] N.S. Biradar, A.M. Hengne, S.S. Sakate, R.K. Swami, C.V. Rode, Single pot transfer hydrogenation and aldolization of furfural over metal oxide catalysts, Catal Lett 146 (2016) 1611–1619. https://doi.org/10.1007/s10562-016-1786-6.

[35] S. Li, F. Chen, N. Li, W. Wang, X. Sheng, A. Wang, Y. Cong, X. Wang, T. Zhang, Synthesis of renewable triketones, diketones, and jet-fuel range cycloalkanes with 5-hydroxymethylfurfural and ketones, ChemSusChem 10 (2017) 711–719. https://doi.org/10.1002/cssc.201601727.

[36] T. Yutthalekha, D. Suttipat, S. Salakhum, A. Thivasasith, S. Nokbin, J. Limtrakul, C. Wattanakit, Aldol condensation of biomass-derived platform molecules over amine-grafted hierarchical FAU-type zeolite nanosheets (Zeolean) featuring basic sites, Chemical communications (Cambridge, England) 53 (2017) 12185–12188. https://doi.org/10.1039/c7cc06375j.

[37] D. Suttipat, W. Wannapakdee, T. Yutthalekha, S. Ittisanronnachai, T. Ungpittagul, K. Phomphrai, S. Bureekaew, C. Wattanakit, Hierarchical FAU/ZIF-8 hybrid materials as highly efficient acid-base catalysts for aldol condensation, ACS applied materials & interfaces 10 (2018) 16358–16366. https://doi.org/10.1021/acsami.8b00389.

[38] S. Rojas-Buzo, P. García-García, A. Corma, Hf-based metal–organic frameworks as acid–base catalysts for the transformation of biomass-derived furanic compounds into chemicals, Green Chem. 20 (2018) 3081–3091. https://doi.org/10.1039/c8gc00806j.

[39] R.S. Malkar, H. Daly, C. Hardacre, G.D. Yadav, Aldol condensation of 5-hydroxymethylfurfural to fuel precursor over novel aluminum exchanged-DTP@ZIF-8, ACS Sustainable Chem. Eng. 7 (2019) 16215–16224. https://doi.org/10.1021/acssuschemeng.9b02939.

[40] A. Bohre, M.I. Alam, K. Avasthi, F. Ruiz-Zepeda, B. Likozar, Low temperature transformation of lignocellulose derived bioinspired molecules to aviation fuel precursor over magnesium–lanthanum

mixed oxide catalyst, Applied Catalysis B: Environmental (2020) 119069. https://doi.org/10.1016/j.apcatb.2020.119069.

[41] S. Nishimura, A. Takagaki, K. Ebitani, Characterization, synthesis and catalysis of hydrotalcite-related materials for highly efficient materials transformations, Green Chem. 15 (2013) 2026. https://doi.org/10.1039/c3gc40405f.

[42] G.M. Lari, A.B.L. de Moura, L. Weimann, S. Mitchell, C. Mondelli, J. Pérez-Ramírez, Design of a technical Mg–Al mixed oxide catalyst for the continuous manufacture of glycerol carbonate, J. Mater. Chem. A 5 (2017) 16200–16211. https://doi.org/10.1039/c7ta02061a.

[43] L. Hora, V. Kelbichová, O. Kikhtyanin, O. Bortnovskiy, D. Kubička, Aldol condensation of furfural and acetone over MgAl layered double hydroxides and mixed oxides, Catalysis Today 223 (2014) 138–147. https://doi.org/10.1016/j.cattod.2013.09.022.

[44] M. Mokhtar, A. Inayat, J. Ofili, W. Schwieger, Thermal decomposition, gas phase hydration and liquid phase reconstruction in the system Mg/Al hydrotalcite/mixed oxide: A comparative study, Applied Clay Science 50 (2010) 176–181. https://doi.org/10.1016/j.clay.2010.07.019.

[45] K. Kaneda, T. Mizugaki, Design of high-performance heterogeneous catalysts using hydrotalcite for selective organic transformations, Green Chem. 21 (2019) 1361–1389. https://doi.org/10.1039/c8gc03391a.

[46] S. Abelló, D. Vijaya-Shankar, J. Pérez-Ramírez, Stability, reutilization, and scalability of activated hydrotalcites in aldol condensation, Applied Catalysis A: General 342 (2008) 119–125. https://doi.org/10.1016/j.apcata.2008.03.010.

[47] S. Abelló, F. Medina, D. Tichit, J. Pérez-Ramírez, J.C. Groen, J.E. Sueiras, P. Salagre, Y. Cesteros, Aldol condensations over reconstructed Mg-Al hydrotalcites: structure-activity relationships related to the rehydration method, Chemistry (Weinheim an der Bergstrasse, Germany) 11 (2005) 728–739. https://doi.org/10.1002/chem.200400409.

[48] R. Gedye, F. Smith, K. Westaway, H. Ali, L. Baldisera, L. Laberge, J. Rousell, The use of microwave ovens for rapid organic synthesis, Tetrahedron Letters 27 (1986) 279–282. https://doi.org/10.1016/S0040-4039(00)83996-9.

[49] R.J. Giguere, T.L. Bray, S.M. Duncan, G. Majetich, Application of commercial microwave ovens to organic synthesis, Tetrahedron Letters 27 (1986) 4945–4948. https://doi.org/10.1016/S0040-4039(00)85103-5.

[50] A.M. Rodríguez, P. Prieto, A. de La Hoz, Á. Díaz-Ortiz, D.R. Martín, J.I. García, Influence of polarity and activation energy in microwave-assisted organic synthesis (MAOS), ChemistryOpen 4 (2015) 308–317. https://doi.org/10.1002/open.201402123.

[51] R. Nagahata, K. Takeuchi, Encouragements for the use of microwaves in industrial chemistry, Chemical record (New York, N.Y.) 19 (2019) 51–64. https://doi.org/10.1002/tcr.201800064.

[52] S. Horikoshi, R.F. Schiffmann, J. Fukushima, N. Serpone, Microwave chemical and materials processing, Springer Singapore, Singapore, 2018.

[53] J.D. Moseley, C.O. Kappe, A critical assessment of the greenness and energy efficiency of microwave-assisted organic synthesis, Green Chem. 13 (2011) 794. https://doi.org/10.1039/c0gc00823k.

[54] H. Cho, F. Török, B. Török, Energy efficiency of heterogeneous catalytic microwave-assisted organic reactions, Green Chem. 16 (2014) 3623–3634. https://doi.org/10.1039/c4gc00037d.

[55] S. Horikoshi, N. Serpone, Role of microwaves in heterogeneous catalytic systems, Catal. Sci. Technol. 4 (2014) 1197. https://doi.org/10.1039/c3cy00753g.

[56] A. Kokel, C. Schäfer, B. Török, Application of microwave-assisted heterogeneous catalysis in sustainable synthesis design, Green Chem. 19 (2017) 3729–3751. https://doi.org/10.1039/c7gc01393k.

[57] X. Zou, C. Zhu, Q. Wang, G. Yang, Catalytic dehydration of hexose sugars to 5-hydroxymethylfural, Biofuels, Bioprod. Bioref. 13 (2019) 153–173. https://doi.org/10.1002/bbb.1932.

[58] G. Fetter, F. Hernández, A.M. Maubert, V.H. Lara, P. Bosch, Microwave irradiation effect on hydrotalcite synthesis, Journal of Porous Materials 4 (1997) 27–30. https://doi.org/10.1023/A:1009619005529.

[59] P.P. Upare, A. Chamas, J.H. Lee, J.C. Kim, S.K. Kwak, Y.K. Hwang, D.W. Hwang, Highly efficient hydrotalcite/1-butanol catalytic system for the production of the high-yield fructose crystal from glucose, ACS Catal. 10 (2020) 1388–1396. https://doi.org/10.1021/acscatal.9b01650.

[60] J.T. Kloprogge, L. Hickey, R.L. Frost, FT-Raman and FT-IR spectroscopic study of synthetic Mg/Zn/Al-hydrotalcites, J. Raman Spectrosc. 35 (2004) 967–974. https://doi.org/10.1002/jrs.1244.

[61] R. Galindo, A. López-Delgado, I. Padilla, M. Yates, Hydrotalcite-like compounds: A way to recover a hazardous waste in the aluminium tertiary industry, Applied Clay Science 95 (2014) 41–49. https://doi.org/10.1016/j.clay.2014.03.022.

[62] B.E. Hanson, L.F. Wieserman, G.W. Wagner, R.A. Kaufman, Identification of acetone enolate on γ-alumina: implications for the oligomerization and polymerization of adsorbed acetone, Langmuir 3 (1987) 549–555. https://doi.org/10.1021/la00076a019.

[63] M.I. Zaki, M.A. Hasan, L. Pasupulety, Surface reactions of acetone on Al 2 O 3 TiO 2 ZrO 2 and CeO 2 IR spectroscopic assessment of impacts of the surface acid−base properties, Langmuir 17 (2001) 768–774. https://doi.org/10.1021/la000976p.

[64] S.J. Palmer, R.L. Frost, G. Ayoko, T. Nguyen, Synthesis and Raman spectroscopic characterisation of hydrotalcite with CO32− and (MoO4)2− anions in the interlayer, J. Raman Spectrosc. 39 (2008) 395–401. https://doi.org/10.1002/jrs.1838.

[65] S. Abelló, F. Medina, D. Tichit, J. Pérez-Ramírez, X. Rodríguez, J.E. Sueiras, P. Salagre, Y. Cesteros, Study of alkaline-doping agents on the performance of reconstructed Mg–Al hydrotalcites in aldol condensations, Applied Catalysis A: General 281 (2005) 191–198. https://doi.org/10.1016/j.apcata.2004.11.037.

[66] C. Xu, Y. Gao, X. Liu, R. Xin, Z. Wang, Hydrotalcite reconstructed by in situ rehydration as a highly active solid base catalyst and its application in aldol condensations, RSC Adv 3 (2013) 793–801. https://doi.org/10.1039/c2ra21762g.

[67] M. Thommes, K. Kaneko, A.V. Neimark, J.P. Olivier, F. Rodriguez-Reinoso, J. Rouquerol, K.S.W. Sing, Physisorption of gases, with special reference to the evaluation of surface area and pore size distribution (IUPAC Technical Report), Pure and Applied Chemistry 87 (2015) 1051–1069. https://doi.org/10.1515/pac-2014-1117.

[68] S. Ishihara, P. Sahoo, K. Deguchi, S. Ohki, M. Tansho, T. Shimizu, J. Labuta, J.P. Hill, K. Ariga, K. Watanabe, Y. Yamauchi, S. Suehara, N. Iyi, Dynamic breathing of CO2 by hydrotalcite, Journal of the American Chemical Society 135 (2013) 18040–18043. https://doi.org/10.1021/ja4099752.

[69] J. Clayden, N. Greeves, S.G. Warren, Organic chemistry, 2nd ed., Oxford University Press, Oxford, 2012.

[70] A. Tampieri, M. Szabó, F. Medina, H. Gulyás, A brief introduction to the basics of NMR spectroscopy and selected examples of its applications to materials characterization, Physical Sciences Reviews (2020 (in press)).

[71] C. Barriga, M. Gaitán, I. Pavlovic, M.A. Ulibarri, M.C. Hermosîn, J. Cornejo, Hydrotalcites as sorbent for 2,4,6-trinitrophenol: influence of the layer composition and interlayer anion, J. Mater. Chem. 12 (2002) 1027–1034. https://doi.org/10.1039/b107979b.

[72] O. Kikhtyanin, Z. Tišler, R. Velvarská, D. Kubička, Reconstructed Mg-Al hydrotalcites prepared by using different rehydration and drying time: Physico-chemical properties and catalytic performance in aldol condensation, Applied Catalysis A: General 536 (2017) 85–96. https://doi.org/10.1016/j.apcata.2017.02.020.

[73] K. Coenen, F. Gallucci, B. Mezari, E. Hensen, M. van Sint Annaland, An in-situ IR study on the adsorption of CO2 and H2O on hydrotalcites, Journal of CO2 Utilization 24 (2018) 228–239. https://doi.org/10.1016/j.jcou.2018.01.008.

Supplementary information

Microwave-assisted condensation of bio-based hydroxymethylfurfural and acetone over recyclable hydrotalcite-related materials

Alberto Tampieri,[a] Cesare Russo,[a] Raffaele Marotta,[b] Magda Constantí,[a] Sandra Contreras,[a] Francesc Medina*[a]

* Corresponding author. Email address: francesc.medina@urv.cat.

[a] DEQ, ETSEQ, Universitat Rovira i Virgili, Avinguda dels Països Catalans 26, 43007, Tarragona, Spain.

[b] DICMAPI, Università di Napoli Federico II, p.le V. Tecchio 80, 80125, Napoli, Italy.

Table of Contents

S1 - Reaction scheme

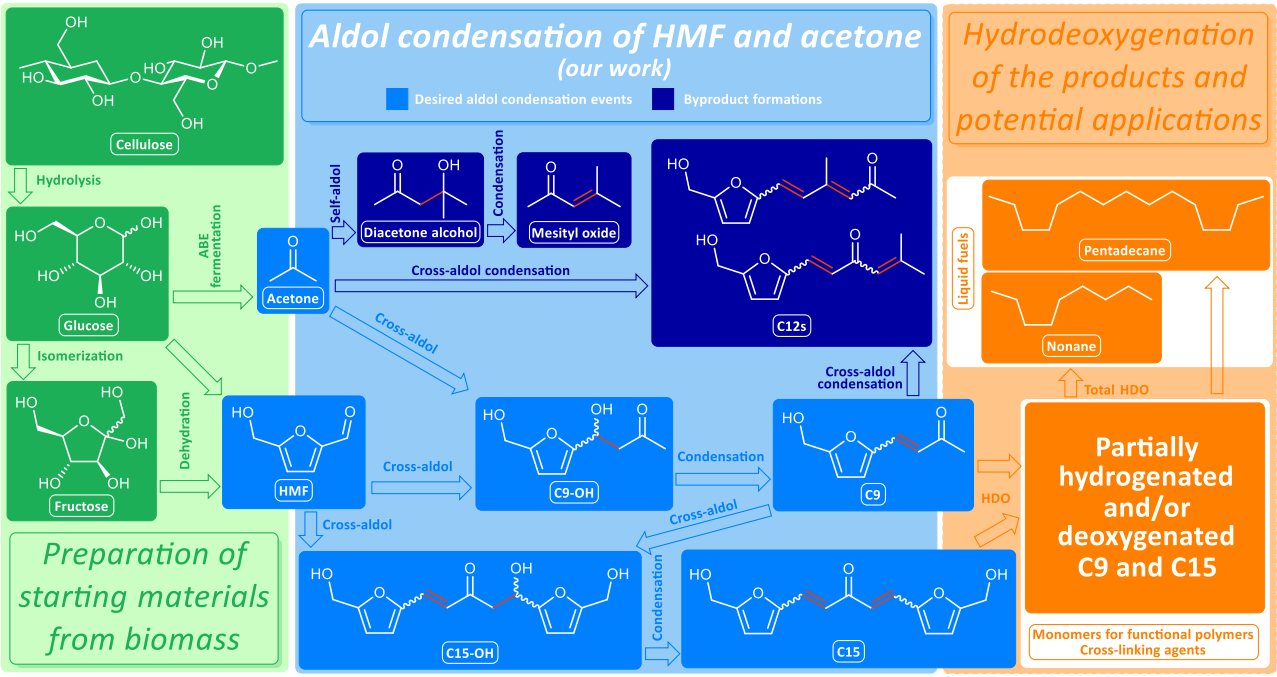

Scheme S1 - Reaction scheme of starting materials preparation (green box), desired aldol condensation process and byproduct formations (our work, blue box); hydrodeoxygenation of the condensation products and their potential applications (orange box).

S2 - Reagents

All starting materials were obtained from commercial sources and used without further purification. The salt precursors used in the preparation of the parent 2:1 Mg:Al HT were $Mg(NO_3)_2 \cdot 6H_2O$ (extra pure, Acros Organics) and $Al(NO_3)_3 \cdot 9H_2O$ (≥ 98 %, Fisher Chemical). In this preparation, NaOH (Pellets, 98.9 %, Fisher Chemical) and Na_2CO_3 (Anhydrous, ≥ 99.5%, Fisher Chemical) were used as well. Na_2CO_3 was also used in the preparation of HT_{reg}. Water used for all experiments was deionized water (as provided by a Simplicity UV water purification system, Merck Millipore, 18.2 MΩ·cm@ 25 °C). Acetone (99.5+%, Acros Organic) was used as a reagent/solvent in the neat aldol condensation, and to wash MX during filtration. The acetone used for dilutions in the preparation of GC-FID samples post-reaction had a lower purity (> 95%, Fisher Chemical). HMF (5-hydroxymethyl-2-furaldehyde, 97%, Alfa Aesar) was used as a reagent, and it was stored in a

refrigerator at 4 °C. This is fundamental to prevent HMF degradation, which will turn the originally white-yellow solid into a yellow-orange one. In addition, HMF is a low melting compound, and storage at higher temperature may result in melting that would afford a tough, unique block out of the original powder. A tank of pure N_2 (≥ 99,9992%, 200 bar at 15 °C, Carburos Metalicos), connected to the MW reactor, was used to increase the chamber pressure during the microwave-assisted condensation experiments. Toluene (≥ 99.3%, Honeywell) was used as an internal standard for the quantification of species in the GC-FID analysis of post-reaction samples. $CDCl_3$ (Chloroform-d for NMR, 99.8 atom % D, Acros Organics) was used as an NMR solvent. D_2O (Deuterium oxide (Heavy water), 99.8 atom % D, Carlo Erba) was used as source of an NMR lock signal. Diacetone alcohol (99%, Aldrich) and mesityl oxide (90%, Aldrich) were used to aid GC-FID peak assignations.

S3 - Details of the catalyst preparation

S3.1 - Preparation of Mg/Al layered double hydroxides (HT)

HT was prepared by co-precipitation following a previously reported procedure [1]. The solution A for the co-precipitation contained the Mg and Al salts, whereas the solution B contained the Na salts necessary to maintain a constant pH in the medium and provide carbonates. Typically, solution A was prepared by dissolving $Mg(NO_3)_2 \cdot 6\ H_2O$ (50 mmol, 12,82 g, 0,36 M) and $Al(NO_3)_3 \cdot 9\ H_2O$ (25 mmol, 9,38 g, 0,18 M) in 140 mL of deionized water. Solution B was prepared by dissolving NaOH (500 mmol, 20 g, 2 M) and Na_2CO_3 (125 mmol, 13,25 g, 0,5 M) in 250 mL of deionized water. Solutions A and B were added dropwise at room temperature into a glass vessel which initially contained 100 mL of deionized water, under magnetic stirring (500 rpm). The pH was monitored by a pH meter (HI-5222, HANNA Instruments) and controlled by the solutions' addition rates. The glass vessel was then covered and the co-precipitation medium was left stirring at room temperature overnight. Then, the solid was separated with a Buchner filtration (Filter paper, qualitative, Fisherbrand), then washed with 3 L of deionized water to completely remove sodium from the HT [2]. The obtained solid was then transferred into a crucible and dried at 80 °C for 24 hours. The dry

solid was ground, passed through a 500 μm sieve and stored in a closed vial. The described procedure affords about 5-6 g of white, dry HT.

S3.2 - Preparation of Mg/Al mixed metal oxide (MMO)

MMOs were prepared by calcination of layered double hydroxides (HT or MX, as synthesized or recovered). The desired amount of HT was weighted in a crucible. The crucible was inserted into a muffle furnace (HD - 150 muffle furnace, Hobersal) at room temperature. The HTs were heated to 450 °C in 1 hour, and the temperature was kept under air for 4 h. After this time, the furnace was let cooling down to about 200 °C. The crucible was then covered, taken out of the furnace and let cool down. The obtained white MMO is not stable under air and it was not stored. All reactions with an MMO as a catalyst involved freshly-calcined solids. The mass loss of HT after calcination is typically around 40-50%.

S3.3 - MMO regeneration (HT_{reg})

Regenerated HT catalysts (HT_{reg}) were prepared by modification of the correspondent MMO. Freshly calcined MMOs were immersed in aqueous solutions containing an excess of carbonate anions, which reconstruct the original LDHs, following a previously reported procedure [3]. Typically, 0,5 g of MMO were immersed in 250 mL of a Na_2CO_3 0,1 M aqueous solution. The mixture was then left under magnetic stirring (500 rpm) at room temperature for 24 h. After this time, the mixture was centrifuged and the liquid portion eliminated. The mixture was distributed between 50 mL centrifugation tubes and put in a centrifuge (Jouan BR4i multifunction, Thermo Electron Corporation). The tubes were centrifuged at 3500 rpm for 10 minutes, and the liquid discarded. The collected solid is then immersed in 100 mL of de-ionized water and stirred for 10 minutes at room temperature, then centrifuged again. This operation was repeated 3 times overall (or until neutral pH of the filtrate is reached). The obtained solid was then transferred into a crucible and dried at 80 °C for 24 hours. The obtained dry, white HT_{reg} was stored in a closed vial.

S3.4 - MMO rehydration (MX)

Rehydrated HTs catalysts (MX) were prepared by modification of the correspondent MMO. For the rehydration, freshly calcined MMOs were immersed in liquid water. Typically, 0,5 g of MMOs were immersed in 250 mL of de-ionized water contained in a 2-neck round bottom flask. Before immersion, the liquid was bubbled with pure Ar for 10 minutes; after immersion, the mixture was bubbled for 5 more minutes. The round bottom flask was then sealed with cap and parafilm, and the mixture was left stirring at 500 rpm for 24 hours at room temperature. After this time, the stirring was stopped, and the mixture was centrifuged to separate the solid. The following step shall be performed rapidly, as the contact of the obtained MX with the CO_2 contained in the air has a negative effect on its catalytic properties [4]. The wet solid obtained after centrifugation was filtered. Small quantities of pure acetone (previously inertized by bubbling pure Ar for 10 min and cooled in an ice bath) were then used to remove the residual water. This step was performed to remove the water on the surface of the MX to facilitate the drying process, due to the higher volatility of acetone; acetone was cooled down to minimize its self-condensation reaction catalyzed by the rehydrated hydrotalcite. The obtained solid was transferred into a vial and dried overnight under vacuum to obtain the dry and white MX. The catalyst was stored for short periods of time under vacuum to prevent the interaction of the solid with air CO_2.

S3.5 - Catalyst recovery after aldol condensation (HT_{rec}, MMO_{rec}, MX_{rec})

After reaction, the solids were separated from the reaction mixtures via Buchner filtration (Filter paper, qualitative, Fisherbrand). The solids were washed with abundant acetone in order to wash away all of the non-adsorbed reaction components. The obtained solids were then transferred into crucibles and let dry from acetone overnight under air. Typically, the solids were left at room temperature, which affords yellow/brown-colored solids; the tone of this color appears to change according to the

conversion obtained for the reaction they were used as catalysts (Fig. S1): from gold (MMO_{rec}, low conversions), to golden brown (HT_{rec}, intermediate conversions), to ochre (MX_{rec}, high conversions). Drying at higher temperatures seems to alter the composition of the surface-adsorbed species, which results in a color change to darker (brown) colors. The solids obtained after drying were stored in closed vials.

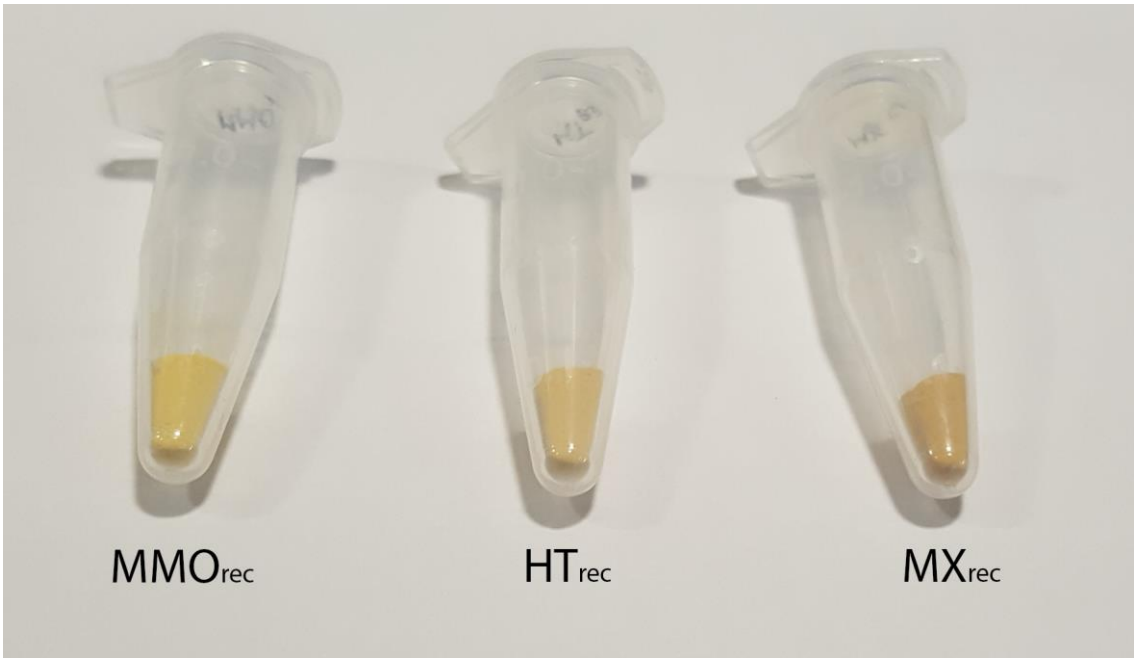

Fig. S1 - Photographs of the solids recovered after reactions with identical reaction conditions.

S4 - Details of the catalyst characterization

S4.1 - Inductively Coupled Plasma - Atomic Emission Spectroscopy (ICP-AES)

The original HT was analyzed by ICP-AES to obtain the content of Na, Mg, and Al of the solid obtained after the co-precipitation. The analysis was performed on two different samples, taken from two different batches of HTs prepared following the same procedure (HT and HT_{bis}). The digested samples were prepared by weighing 50,0 mg of HT sample from the first batch, and 51,1 mg of HT_{bis} sample, inserting them in the dedicated vessel and adding 10 mL of 69 % HNO_3. The vessels were then sealed and inserted into a microwave digester (Ethos Easy, Milestone), and digested following the microwave program that is reported in Fig. S2.

Fig. S2 - Microwave program for ICP-AES sample digestion.

The solutions obtained after digestion were transferred to 50 mL volumetric flasks and diluted with deionized water. The concentrations of Na, Mg and Al in the samples were calculated using calibration curves for the elements in the range 0-20 ppm. The concentrations obtained for Mg and Al were outside of this range, and a dilution was needed to bring their concentrations into the linear range. More diluted samples were prepared by performing a 1 to 10 dilution with deionized water. Table S1 & S2 reports the obtained concentrations for HT and HT_{bis}, respectively. The sodium content in both samples is very low, indicating a successful HT washing during the work-up.

Element	<x>	n	sd	t (α = 0.05, DF = 2)	Dilution	Result [mg/L]
Mg	22.323	3	0.081	4.303	1:10	223±2
Al	10.531	3	0.035	4.303	1:10	105.3±0.9
Na	<0	3	0.001	4.303	/	n.d.

Table S1 - ICP-AES elemental analysis of HT.

Element	<x>	n	sd	t (α = 0.05, DF = 2)	Dilution	Result [mg/L]
Mg	22.463	3	0.328	4.303	1:10	225±8
Al	10.553	3	0.072	4.303	1:10	106±2
Na	0.014	3	0.002	4.303	/	0.014±0.005

Table S2 - ICP-AES elemental analysis of HT_{bis}.

S4.2 - Energy Dispersive X-ray spectroscopy (ESEM-EDX)

The dried catalysts were analyzed by ESEM-EDX. The samples were prepared by suspending the solid in distilled water by sonication, and then depositing a drop of this suspension on a crystalline Si wafer. The drops were let drying under air in a fumehood for 3h at room temperature before analysis. In Fig. S3 are collected the EDX spectra of the catalysts with two repetitions for each solid, performed on different points of the same sample. HT, HT_{rec}, HT_{reg}, MX and MX_{rec} were analyzed as solids deposited on silicon wafers because the carbon content of the samples is information of interest. As a result, silicon appears in (some of) the EDX spectra although no silicon is present in the original samples. This was proved by a blank analysis of HT deposited on carbon (Fig. S3, a and b).

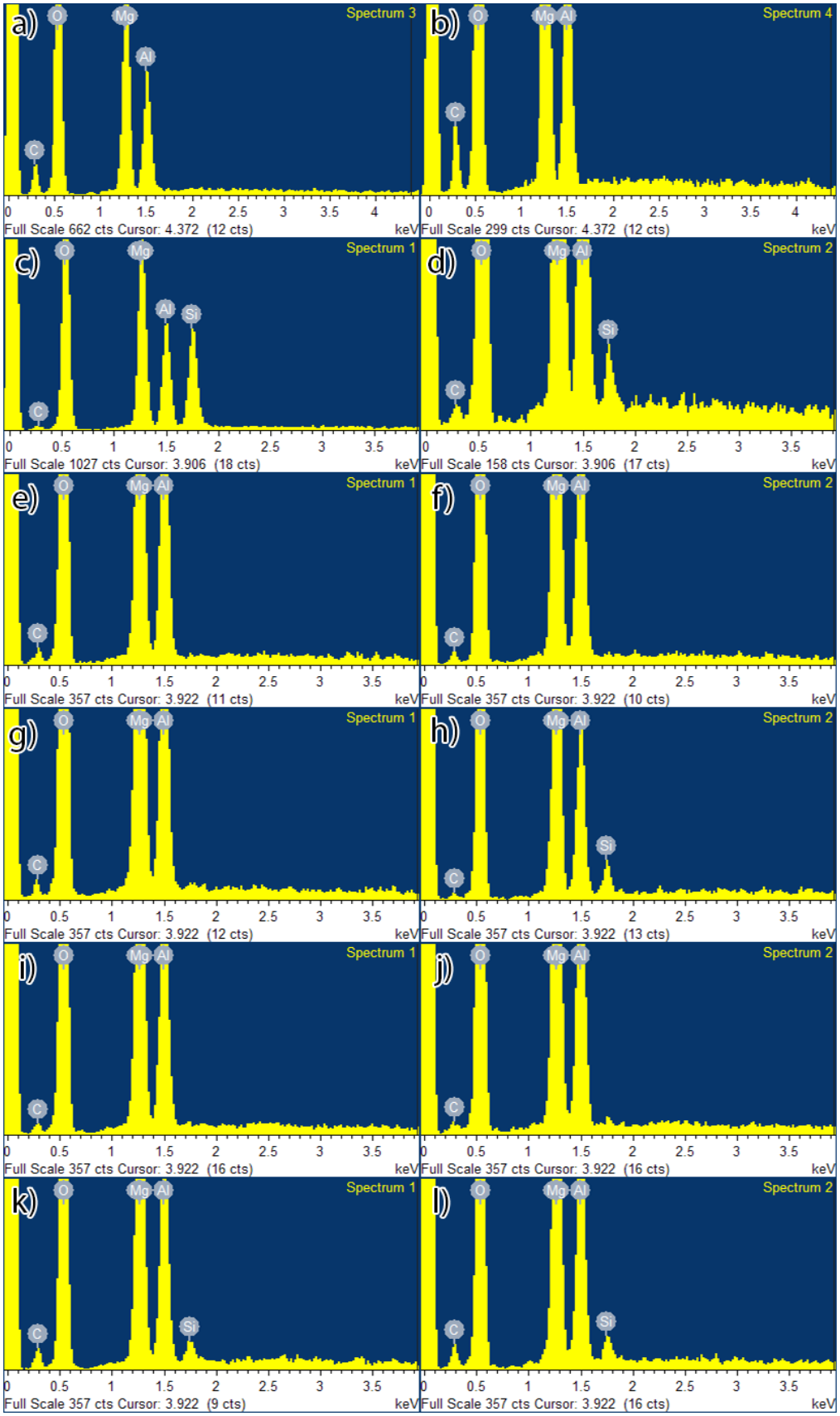

Fig. S3 - EDX spectra of HT on carbon (a and b); EDX spectra on silicon of HT (c and d), HT_{rec} (e and f), HT_{reg} (g and h), MX (i and j) and MX_{rec} (k and l).

S4.3 - Raman spectroscopy

The samples were analyzed as powders placed on microscope glass slides and observed with the microscope to correctly center the laser on the desired sample. The powder was then excited with a red (633 nm) laser for 10 seconds and its Raman spectrum registered. HMF and C15 were analyzed cold, that is, just taken out from the refrigerator; MMO analyzed was freshly calcined; MX analyzed was stored under vacuum until it was analyzed; the rest of the samples were not stored with any particular care.

The obtained spectra are reported in Fig. S4. All HTs give rise to the same peaks, whose positions are in good agreement with previously reported data for HTs [5]. These peaks cannot be spotted in the spectrum of the MMO, which presents a different set of broad peaks, as a result of calcination. The spectra of all recovered catalysts are dominated by fluorescence, and no peak can be distinguished clearly. Fluorescence also dominates the spectra of C15 and HMF; while for the former no signal can be discerned from the baseline, the spectrum of the latter presents peaks that appear to be also in good agreement with the previously reported data [6].

One way to eliminate the effects of fluorescence in the spectra of our samples is, for instance, to irradiate with the laser for a longer time, which induces an alteration in the structure of the compounds and causes the fluorescence to fade (photobleaching). However, since the organic matter that brings about the fluorescence is the analyte of interest, this is not a viable option for our investigations. For this reason, to get rid of the fluorescence we decided to use a different laser, with a wavelength of 785 nm. The obtained spectra are in Fig. S5. The spectrum at 785 nm excitation of an HT sample (HT_{reg}) includes, of course, the same peaks as in the relative spectrum at 633 nm. The signal-to-noise ratio in his spectrum is very low, as a result of the higher excitation wavelength, and the broad peak at ~ 3500 cm^{-1} cannot be seen. Also, no signals are seen in the spectrum of HT_{rec}.

As a conclusion, Raman spectroscopy does not allow to obtain any information on the organic matter contained in the recovered catalysts, at least not by normal means.

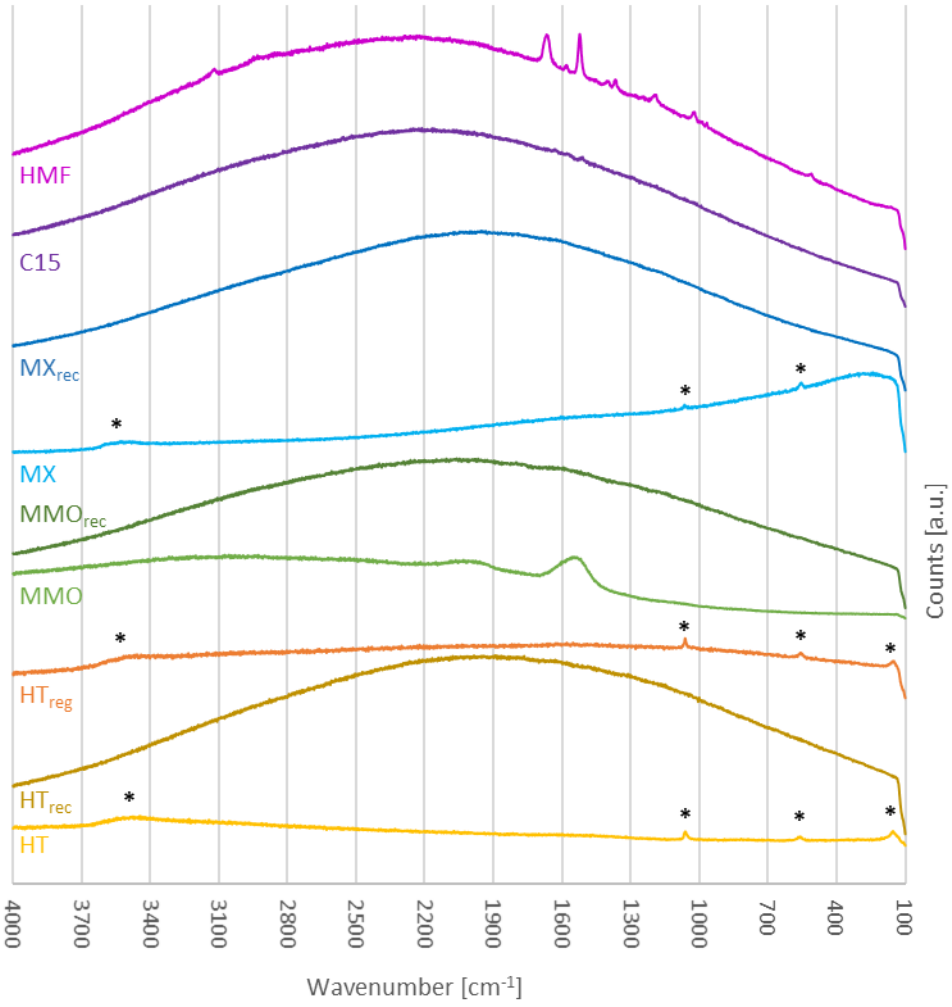

Fig. S4 - Raman spectra of solid catalysts and reaction species recorded after excitation with the 633 nm laser.

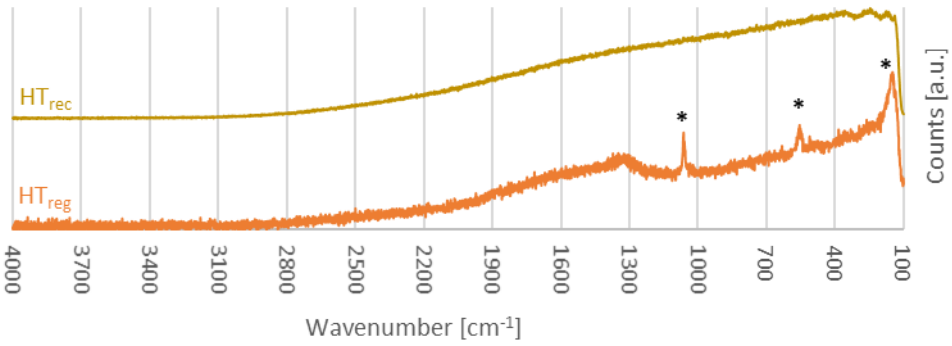

Fig. S5 - Raman spectra of solid catalysts recorded after excitation with the 785 nm laser.

S4.4 - ThermoGravimetric Analysis coupled with Mass Spectrometry (TGA-MS)

The outlet of the thermal analyser SENSYS evo was connected to the inlet of the mass spectrometer (HiCube pumping station and PrismaPlus QMG220, Pfeiffer Vacuum). The results obtained by the mass spectrometer for the analyses in Ar are reported in Fig. S6. Among all the channels selected for analysis, each corresponding to a specific mass, the channel of CO_2 was the only one providing clear and relatively sharp signals. Therefore, this gas is the only one that will be discussed. While freshly calcined MMO does not give rise to any CO_2 signal, all the other solids do. The HTs originate two signals at ~ 350 and at ~ 450 °C, plus an almost indistinguishable one at ~ 200 °C; the MX profile includes only the one at ~ 450 °C. All recovered catalysts develop CO_2 over a long period of time, ranging from 30 to 70 minutes (corresponding to ~ 300 and ~ 700 °C, respectively).

It should be noted that the time-temperature relation reported in Fig. S6 refers to the thermal analyser, whereas the time in the MS results refers, of course, to the mass spectrometer. For this reason, there is a delay between the two analysis (whose magnitude has not been determined but that should be in the order of minutes) and the real temperatures may be lower than the ones discussed.

The TGA and MS results obtained for the analyses in synthetic air are reported in Fig. S7. Apparently, the presence of O_2 does not have a remarkable influence on the decomposition of both HT and HT_{rec}.

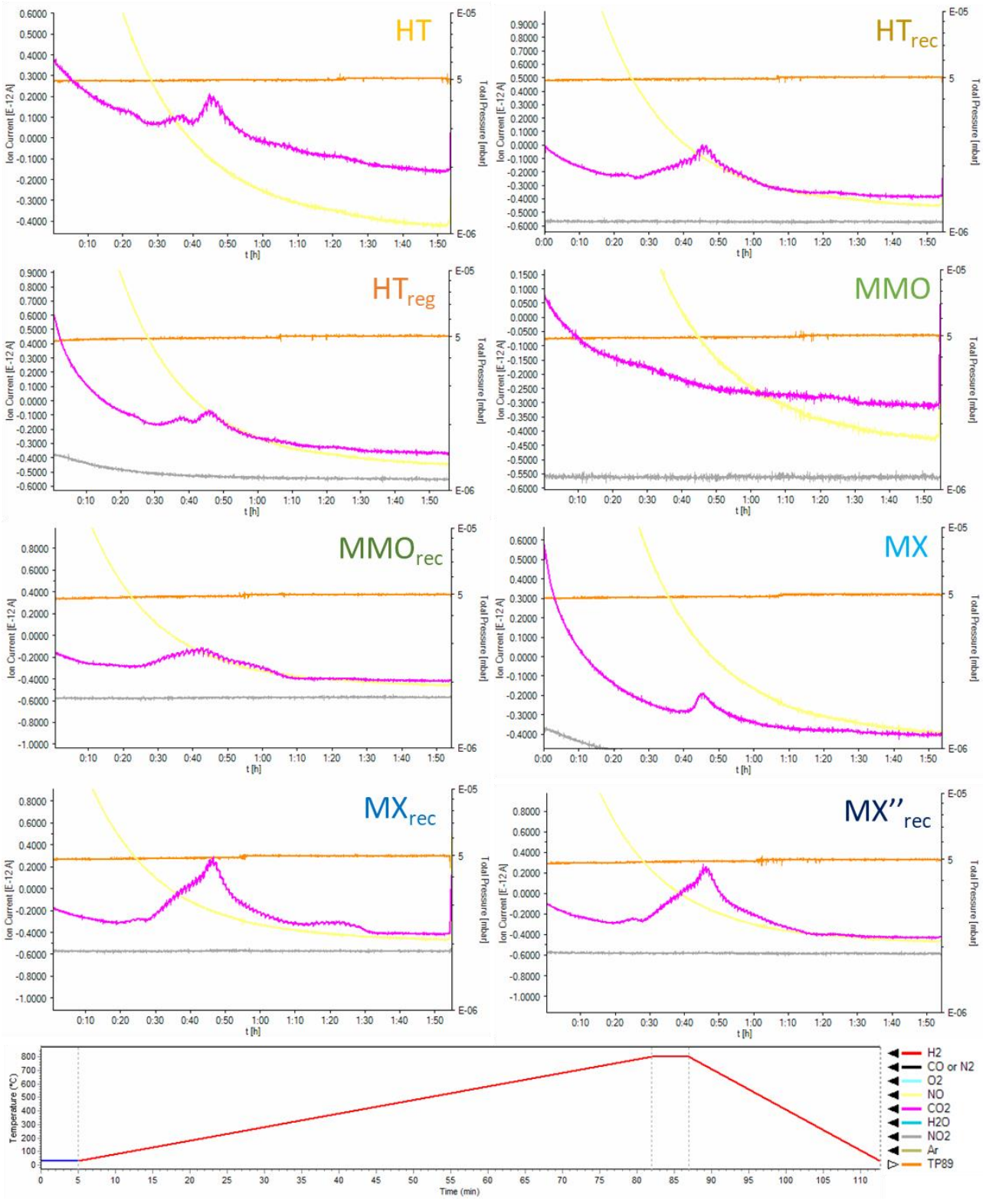

Fig. S6 - Above: mass spectrometry results for each catalyst; below: relation between analysis time and temperature of the thermal analyzer chamber and legend containing the color code of the mass spectrometry graphs.

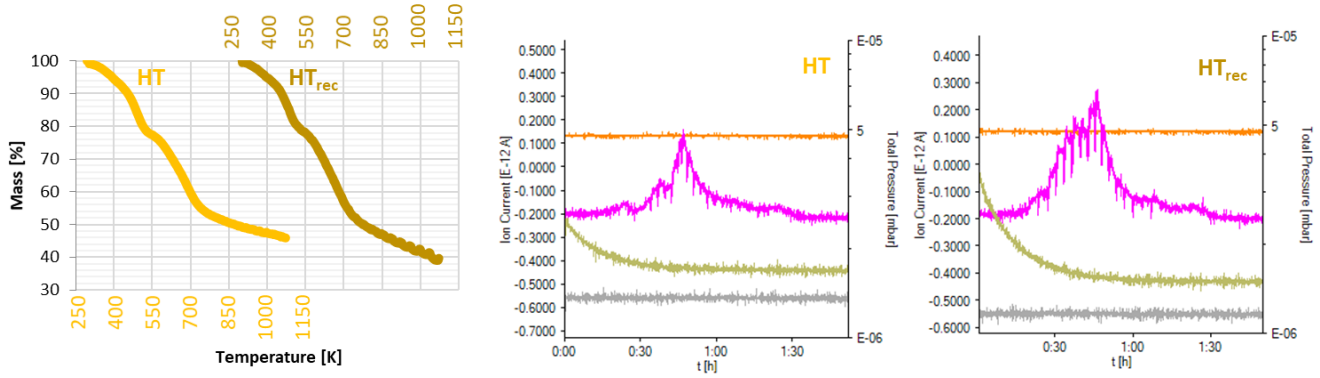

Fig. S7 - Left: TG curves for HT and HT_{rec}, under air; center: MS results for HT; right: MS results for HT_{rec}.

S4.5 - Temperature-programmed desorption of CO_2 (TPD-CO_2)

Two types of TPD experiments were performed. In the first type of experiment (degradation study), no external CO_2 was flown through the sample holder, and the only CO_2 detected was the one arising from carbonates contained in the original sample. In the second type of experiment (CO_2 adsorption-desorption study, to measure the basicity of the sample) CO_2 was flown during the low-temperature adsorption step. In Fig. S7 is a graph illustrating the TPD analysis conditions of this second type of experiments; the conditions of the first type of experiments are identical to those, with the only difference being that the flow of He is constant at 30 cm^3/min throughout the whole experiment. The results of the TPD analyses are recorded by a TCD detector; the obtained profiles, expressed in a.u., are converted to the ones expressed in CO_2 STP cm^3/min based on a calibration curve for this gas. The signal areas are selected with the Peak Editor function of the program (AutoChem II 2940 V4.03), and are expressed as cm^3/g STP. The final results are expressed as µmol (of CO_2)/g (of catalyst) by dividing the peak area for the molar volume of a gas at STP (0.02241 cm^3/µmol at 0 °C and 1 atm, conditions reported in the manual). Finally, the net adsorption of CO_2 of a catalyst is obtained by subtracting the value obtained from the degradation experiment from the one obtained after the corresponding CO_2 adsorption-desorption experiment.

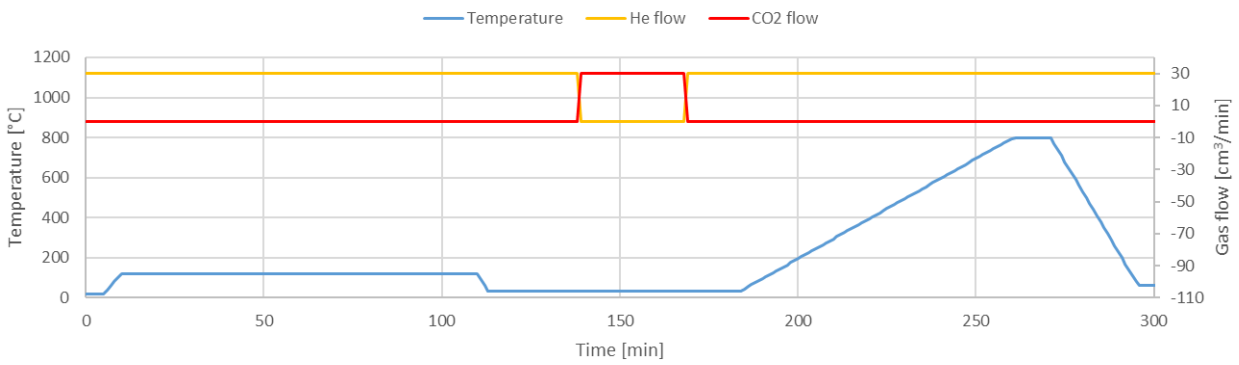

Fig. S7 - TPD analysis conditions for the CO_2 adsorption-desorption experiments.

In Fig. S8 are the results of the degradation experiments for HT, MMO and MX when no trap is used. The obtained profiles are expressed in CO_2 STP cm^3/min for comparison with other profiles, but they also include water signals (the TGA-MS results indicate that the presence of nitrate in the HT is negligible); therefore, the profiles do not actually reflect the desorption profile of CO_2.

Hence, a water trap is necessary. We preferred using a physical trap instead of a chemical one to avoid any retention of CO_2. Water in the gas stream is sequestered by means of solidification to ice. In order to do that, a cooling bath at a temperature lower than 0 °C is required; another requirement is that the bath temperature is higher than -78.5 °C, temperature at which gaseous CO_2 sublimates. For this reason, we used simple a bath of ethanol:ethylene glycol 20:80 v:v, cooled down to -65 °C in a refrigerator, contained in a dewar flask with flat bottom (Type FB-CAL, KGW Isotherm). Under this conditions, if nitrates are converted to NO_2 (although no such specie was detected by TGA-MS), this molecule would also be trapped. The temperature of the bath was monitored with a 2-channel differential thermometer (testo 922, Testo ltd.) and it decreased over time during the analysis, but this proved not to be a problem for analysis reproducibility. However, at the end of one day of analyses the bath reaches a temperature of about -10 °C and it must be renewed. In Fig. S9 are the TPD-CO_2 degradation profiles obtained when the cold trap is used.

The same strategy was used when performing CO_2 adsorption-desorption studies (Figure S10).

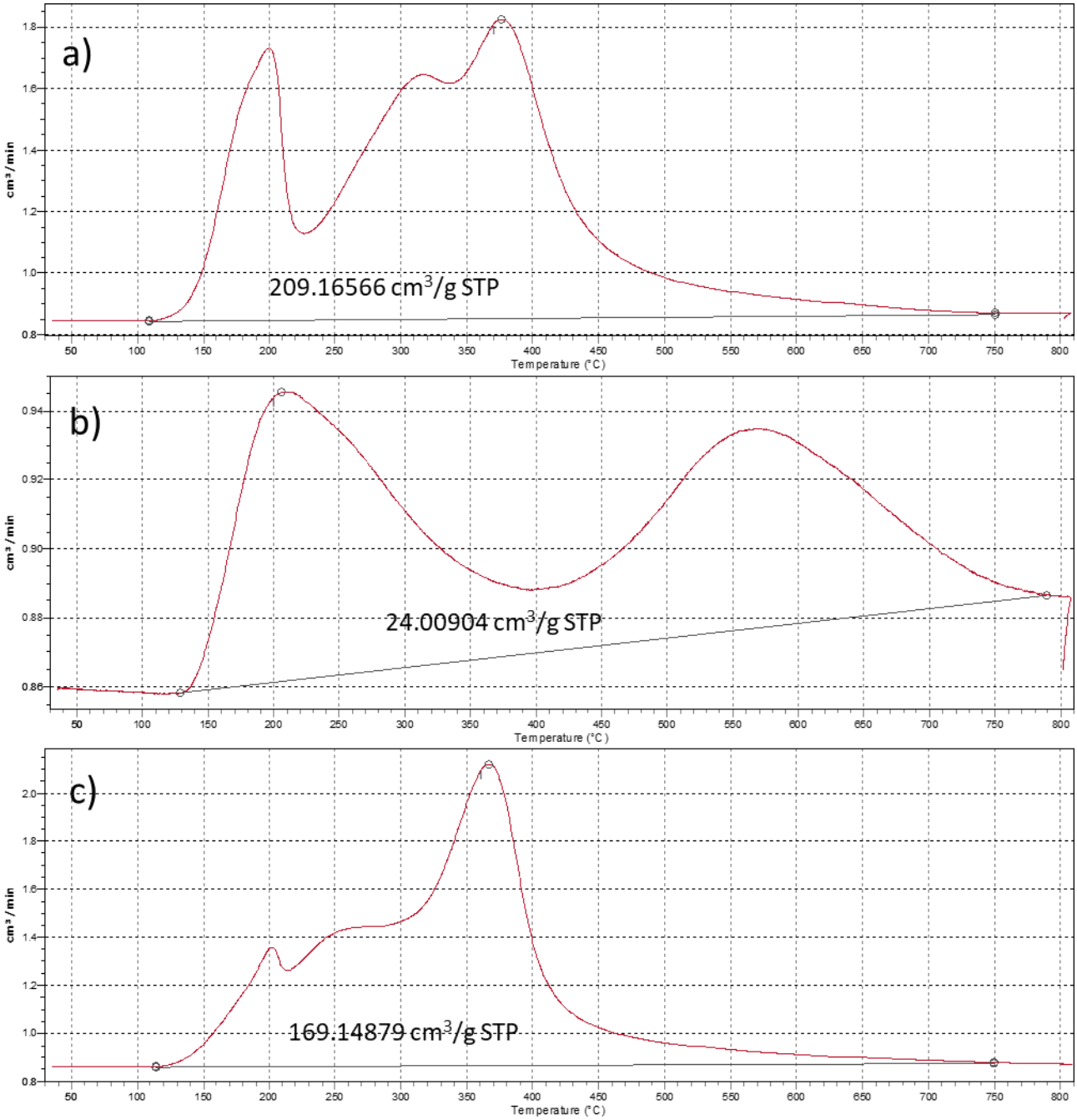

Fig. S8 - TPD profiles for HT (a), MMO (b) and MX (c) when no trap is used (degradation study).

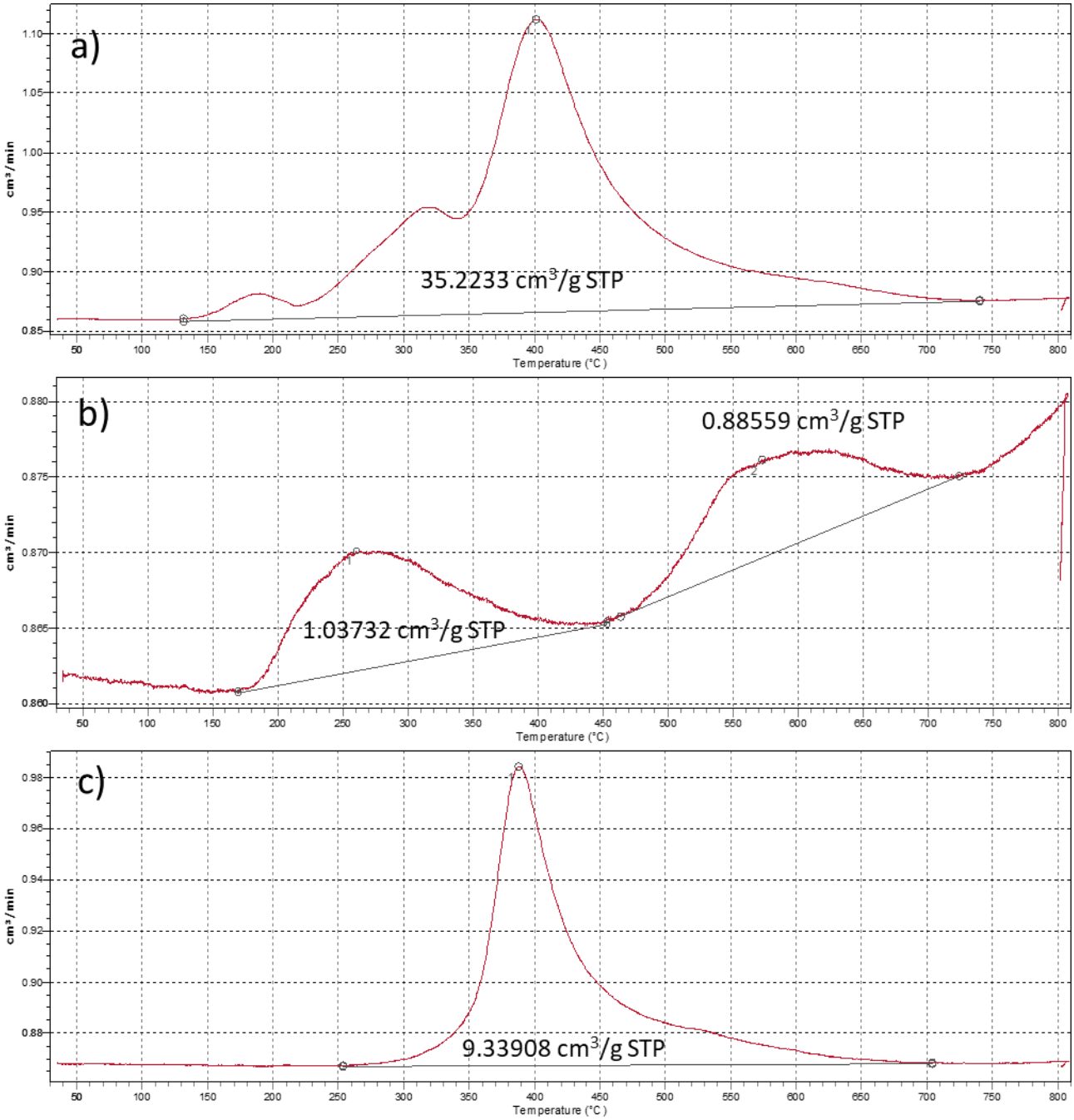

Fig. S9 - TPD profiles for HT (a), MMO (b) and MX (c) when the cold trap is used (degradation study).

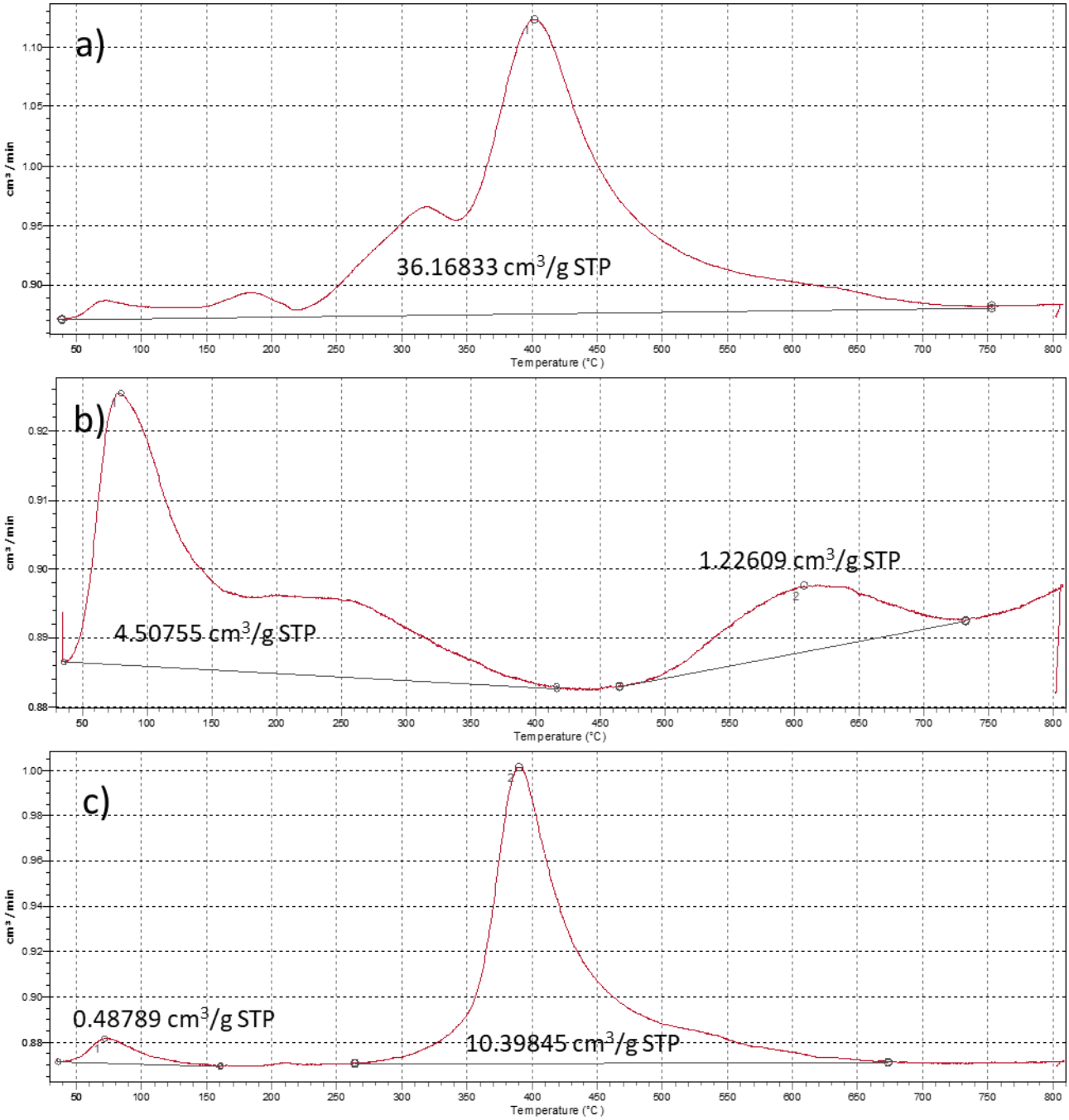

Fig. S10 - TPD profiles for HT (a), MMO (b) and MX (c) when the cold trap is used (CO_2 adsorption-desorption study).

S5 - Details of the microwave-assisted aldol condensation protocol

S5.1 - Reaction mixture preparation

A mother solution of HMF was prepared by weighing the desired quantity of HMF in a 5 mL volumetric flask, filling it with pure acetone. This step is performed because of the difficulty in weighing HMF, since its low melting point makes it sticky; in addition, it may melt in hot weather.

Hence, in principle, preparing a mother solution should improve the reproducibility of the initial HMF quantity, and also reduce wastes. All mother solutions used were freshly prepared, as HMF appears to be not stable in solution with an unidentified byproduct being formed over time (perhaps a dimer) [7], although very slowly. The reaction solutions were prepared by putting the correct volumes of the mother solution in 5 mL volumetric flasks so that each of them contains 0,1 g of HMF (0,79 mmol). The transfer of the mother solution to the volumetric flasks was done by using a 1000 μL micropipette. These volumetric flasks were also filled with pure acetone. Therefore, the HMF initial concentration in the reaction solution is 0,02 g/mL (0,16 mM). The desired quantity of solid catalyst was weighed and added to the oven-dried glass reaction tube, together with a stir bar. The typical quantity of solid catalyst added was 0,02 g (HMF:catalyst 5:1 w/w). The reaction solution was then transferred into the reaction tube, loosely covered with a cap, and the tube was placed in the reactor's rack.

S5.2 - Microwave-assisted reaction

The rack was introduced into the reactor and immersed in the heating bath. The bath is contained in a PTFE reaction vessel and it consisted of 250 mL of de-ionized water at room temperature. The rack includes a magnetic stirrer whose movement induces agitation in the reaction mixtures by rotating the stir bars in the tubes; the magnetic stirrer also agitates the liquid bath. In all cases, five reaction tubes, containing either reaction mixtures or pure acetone, were inserted in the rack in order to fill it and ensure reproducibility, as the number of tubes influence the bath level according to the Archimedes' principle and would affect the heat transfer to the reaction mixtures. The rack was then connected to cover of the reactor and the reaction chamber was closed by lowering this cover. An O-ring between the cover and the PTFE reaction vessel makes the chamber tightly sealed. The chamber is connected to a N_2 tank through a valve (with a rotary handle), which was opened to pressurize the chamber to 10 bar and then closed.

The reactor (Fig. S11, single reaction chamber microwave synthesis system, Milestone SynthWAVE) was controlled with a control panel (Terminal 660 with easyCONTROL software) connected to it.

The software allowed the control of the various parameters during operation. The irradiation power limit was set to 300 W. The stirring rate was set to 50 %. The system is connected to a chiller, which prevents overheating of the machine during operation and promotes the cooling of the reaction vessel at the end of the reaction. The temperature of the cooling liquid is set to be 4 °C, and the recirculation is activated when the temperature outside of the vessel reaches 40 °C. Although the instrument allows the design of experiments with very complex temperature programs, the temperature programs of all experiment had the general structure of a first heating step (t_1, Fig. S12), followed by a second constant-temperature step (t_2) and concluding with a cooling step (t_3) to reach temperatures below 56 °C (acetone's boiling point) before pressure release, as explained in the main text. In Fig. S13 is depicted the temperature program for the optimized protocol. It is also possible to release pressure and open the vessel at higher temperatures, but not above 80 °C for safety reasons. Once the pressure is released, the reaction vessel is open and the reaction tubes are collected.

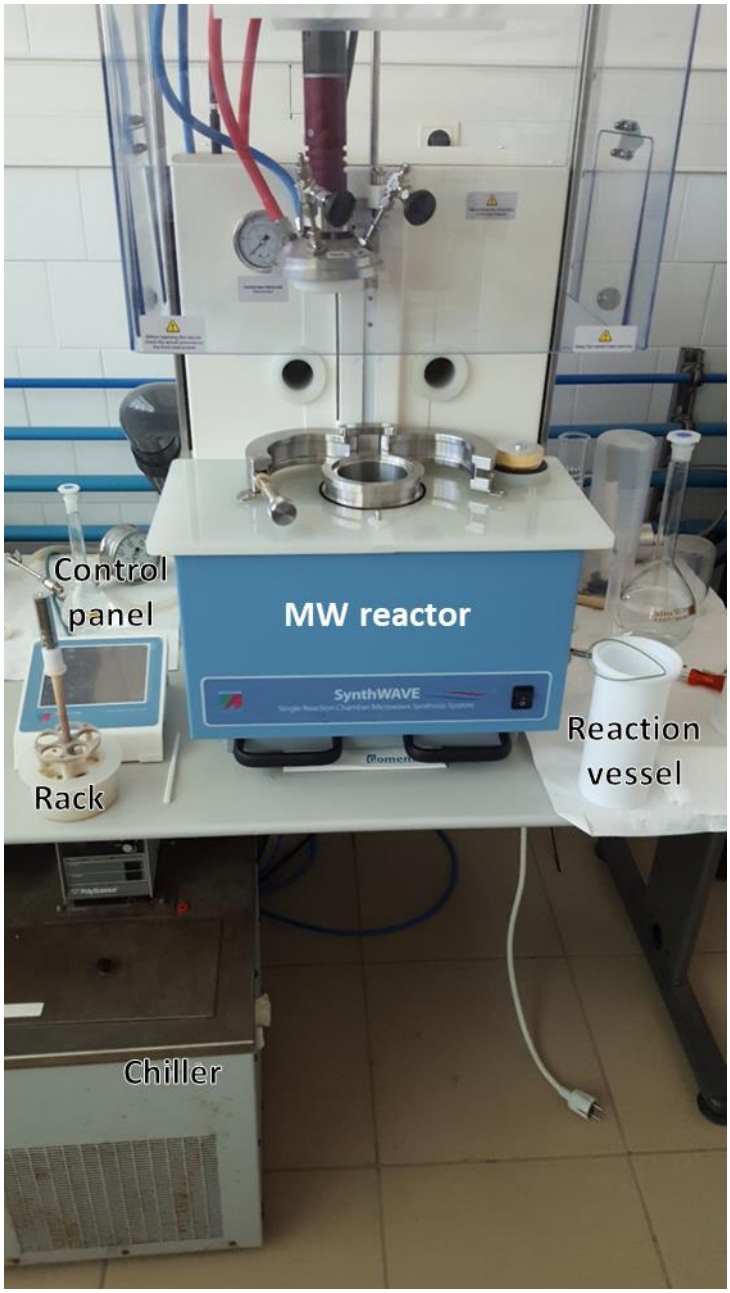

Fig. S11 - Photograph of the synthWAVE reactor and other elements.

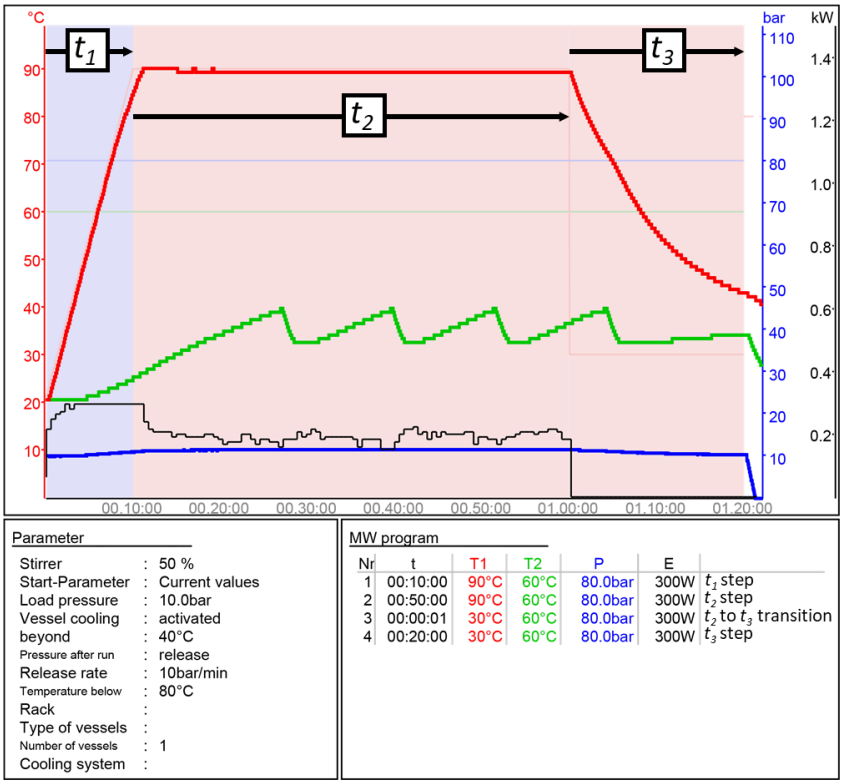

Fig. S12 - Parameter profiles in a typical microwave experiment: set (thin red) and real (thick red) bath temperature; maximum (thin green) and real (thick green) temperature of the outer stainless steel vessel (regulated by the chiller); maximum (thin blue) and real (thick blue) pressure of the reaction chamber; microwave irradiation power (black).

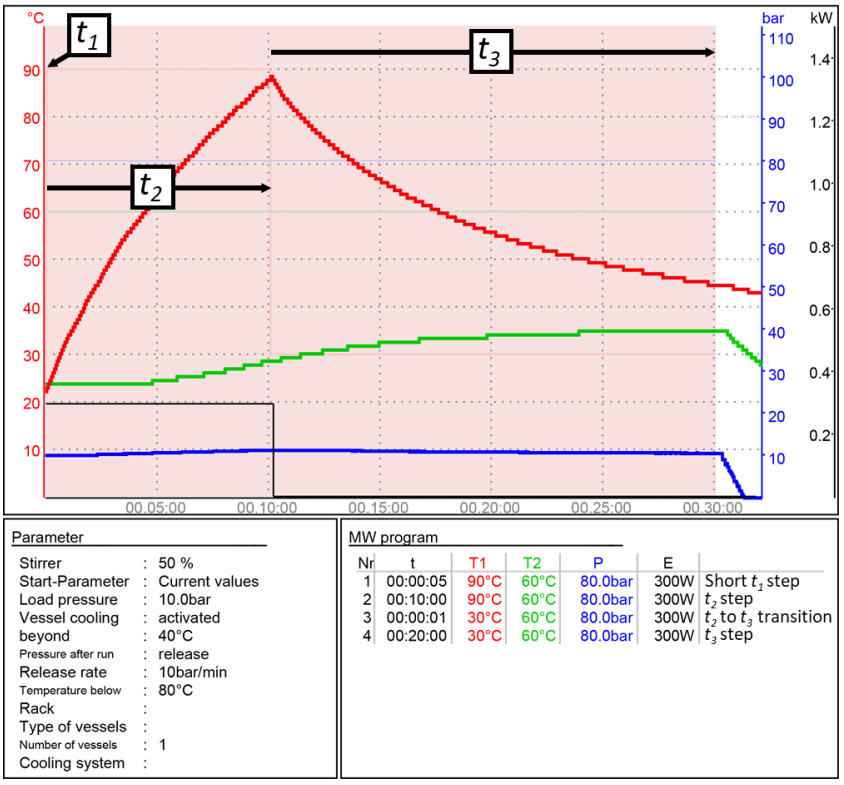

Fig. S13 - Parameter profiles in a microwave experiment with the optimized protocol.

S5.3 - Analysis of the reaction mixture

Solutions to collect samples during reaction with our reactor are possible, but modifications to the reactor setup are required. Moreover, the short reaction times make analysis during reaction unpractical. For these reasons, all analyses reported in this section are performed on samples collected from the final reaction mixture after pressure release.

S5.3A - GC-FID

The tubes collected after reaction were placed on a rack and positioned on a stir plate. 100 µL of pure toluene (0,94 mmol) was added with a 100 µL micropipette to the reaction mixture as an internal standard. The walls of the reaction tube were cleaned with a small quantity of low purity acetone. Toluene was completely dissolved by magnetically stirring the mixture for 2 minutes at 500 rpm. Then, the agitation was stopped, and from each tube 1 mL of reaction mixture was taken with a 1000 µL pipette and put in a different 5 mL volumetric flask. This operation dilutes the sample so that the reaction components do not saturate the GC column and good peak shapes are obtained in the chromatogram. The volumetric flasks were filled with lower purity acetone, and a sample was taken with a syringe and filtered with a nylon filter (Nylon 25 mm 0.22 µm, Sharlab) into a vial. This sample is analyzed with GC-FID (GC-2010 from Shimadzu) using a TRB-5 column (Teknokroma, TR-120232; length: 30 m, film thickness: 25 µm; inner diameter: 0.25 mm). The temperature program is illustrated in Fig. S14 and consists of a first step at constant temperature (50 °C for 2 minutes), a second one of linear temperature increase (50 to 300 °C at 40 °C/min) and a third step at constant temperature (300 °C for 6,75 minutes).

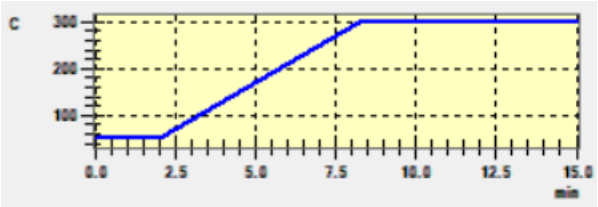

Fig. S14 - GC-FID temperature program.

Fig. S15-17 show typical GC chromatograms obtained with the previously described method for three different samples (called A, B and C), whereas Table S3 summarizes the retention times of the species in the mixture with this GC method. Molecular structures of the species mentioned in Table S3 may be found in Scheme S1.

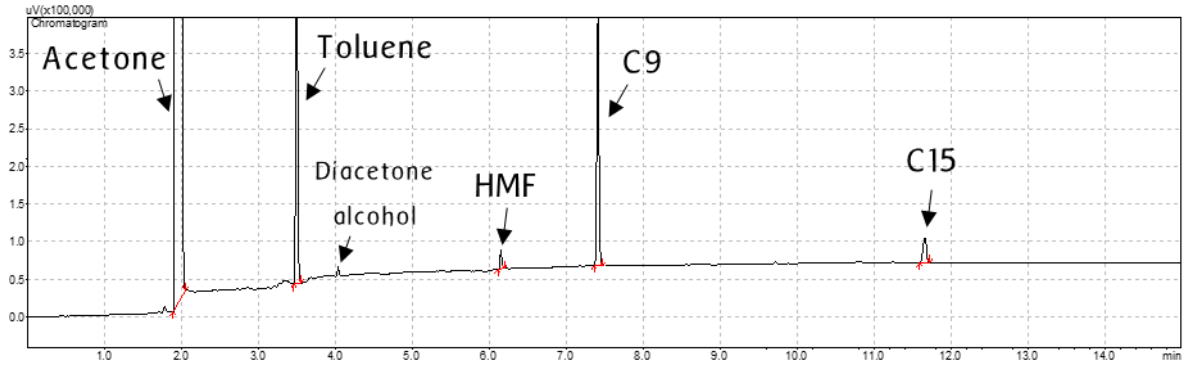

Fig. S15 - GC-FID chromatogram corresponding to the analysis of the final mixture for an MX-catalyzed reaction (Sample A).

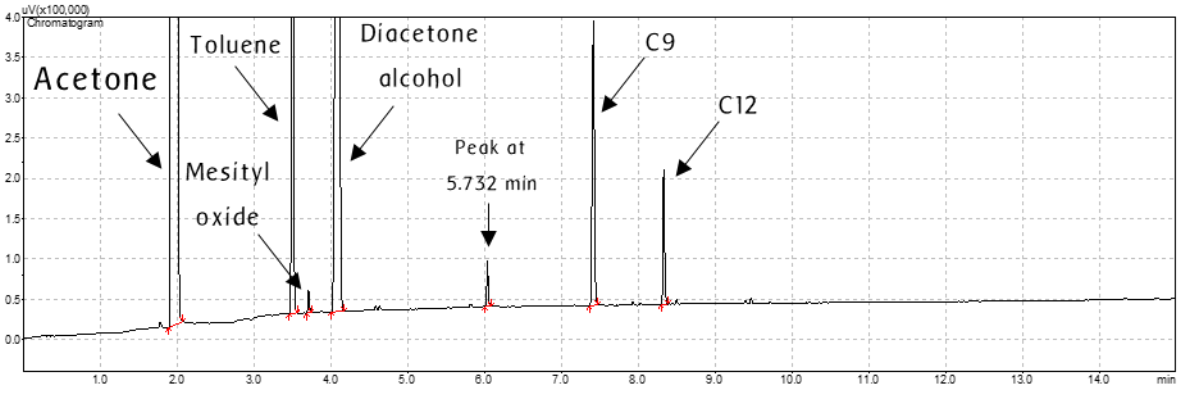

Fig. S16 - GC-FID chromatogram corresponding to the analysis of the final mixture for a NaOH-catalyzed reaction (Sample B).

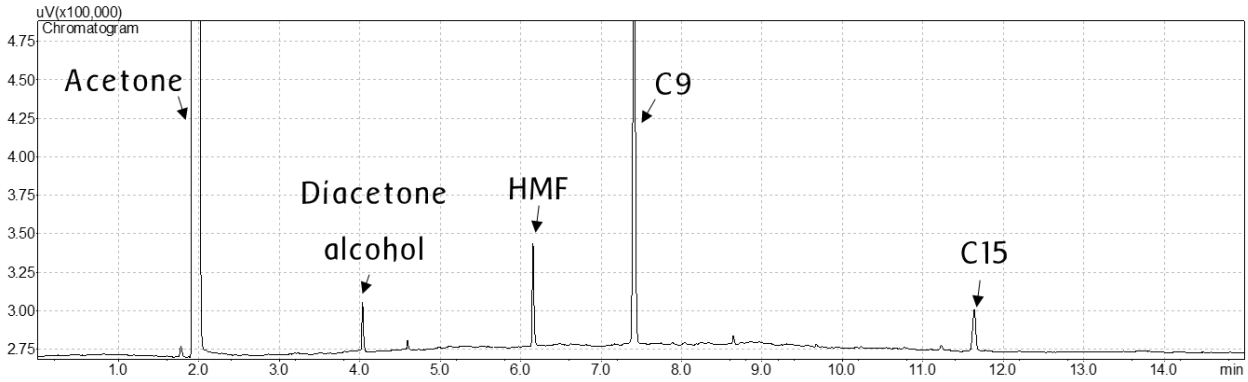

Fig. S17 - GC-FID chromatogram corresponding to the analysis of the final mixture not containing toluene, dried and redissolved in acetone, used for HPLC analyses (Sample C).

Entry	Specie	Role	Ret. time [min]	Identification
1	Acetone	Solvent/reactant	1.96	Injection of pure compound
2	Toluene	Internal standard	3.50	Injection of pure compound
3	Mesityl oxide	Byproduct (acetone self-condensation)	3.72	Injection of pure compound
4	Diacetone alcohol	Byproduct (acetone self-condensation)	4.10	Injection of pure compound
5	Unknown	Unknown	6.04	None (peak at 5.732 min in GC-MS, molecular ion at 159.2 m/z)
6	HMF	Reactant	6.16	Injection of pure compound
7	C9	Intermediate/product	7.43	Comparison with previously reported literature [8]; GC-MS; HPLC-TOF; ^{1}H NMR
8	C12s	Byproduct (condensation of C9 and acetone)	8.33	GC-MS
9	C15	Product	11.65	Comparison with previously reported literature [8]; HPLC-TOF; product synthesis [9]; ^{1}H NMR

Table S3 - Retention times of species in the reaction mixtures. No other peak other than the ones that are related to compounds listed in this table (and that could be distinguished from the baseline) have been observed in any chromatogram of post-reaction samples.

Diacetone alcohol is always detected in the final mixtures, but generally in low concentrations, that is, in concentration not substantially different from the ones in the original pure acetone and in the

lower purity one, where it is present in small quantities as an impurity; mesityl oxide is usually not detected unless diacetone alcohol is present in relatively high concentrations (i. e. when NaOH is used as a catalyst). Other byproducts of further self-condensation of acetone (e. g. phorone, isophorone) were not detected. C12s were only detected when NaOH was used as a catalyst. C9, C12 and C15 are not commercially available, and it was not possible to identify them by GC-FID injection of pure compound. Their identification and the peak assignation were supported by a number of analytical techniques, as described in the next sections.

Obviously, since acetone is used as a solvent, the amount of this compound in the mixture that is converted is negligible as compared to its total amount; hence, the determination of acetone conversion is not possible with our protocol. This makes it also difficult to express the results as carbon balances, as it has been done in other reports [10]. HMF conversion was determined by using a calibration curve calculated using data of samples containing a constant quantity of toluene and quantities of HMF corresponding to 0%, 25%, 50% and 75% conversion. As for quantification of C9 and C15 yields were estimated based on the HMF's calibration curve by using the effective carbon number (ECN) correction factor on the basis of their structure similarity (as they share the same hydroxymethyl furan core) [11]. This approach has been already used in previous reports for the same quantification [8,10] and for related molecular systems [9]. The calculated ECN factors for HMF, C9 and C15 are 3.5, 6.4 and 10.8, respectively. This information can be used to build calibration curves for C9 and C15 based on the areas of the HMF one.

The conversion *X* of HMF, and the yields *Y* and selectivities *S* of C9 and C15 were calculated as follows:

$$X_{HMF} = \frac{n^0_{HMF} - n_{HMF}}{n^0_{HMF}} \cdot 100$$

$$Y_{C9} = \frac{n_{C9}}{n^0_{HMF}} \cdot 100 \qquad and \qquad Y_{C15} = \frac{2 \cdot n_{C15}}{n^0_{HMF}} \cdot 100$$

$$S_{C9} = \frac{Y_{C9}}{X_{HMF}} \cdot 100 \qquad and \qquad S_{C15} = \frac{Y_{C15}}{X_{HMF}} \cdot 100$$

S5.3B - GC-MS

In order to corroborate the peak assignments in the GC-FID chromatograms and to characterize the unknown compounds, GC-MS analyses were performed. Samples were analyzed using a gas chromatograph 6890 Series equipped with an automatic liquid sampler (HP7683 Series) and mass spectrometer (5973 Hewlett Packard). The column used was a HP-5MS (30 m x 0.25 mm x 0.25 μm) from Hewlett Packard, which is analogous to the one used for GC-FID. The GC method mimicked the one reported for GC-FID, with the difference of the last step at 300 °C being longer. Hence, the order of peaks in the chromatograms obtained should be the same as in GC-FID. The first minutes are cut to not saturate the detector.

Analysis of sample A gives a GC-MS chromatogram that contains only two peaks (Fig. S18a). The mass spectrum of the first peak (Fig. S18b), at 5.732 min, matches with the spectrum of HMF (calc. mass for $C_6H_6O_3$: 126.031695 u) in the library. The following, intense peak at 6.945 min should then correspond to C9. Indeed, the mass spectrum of that GC peak (Fig. S18c) has a peak at 166.2 u that appears to be the molecular ion one. C9 is the only reasonable reaction product/byproduct with a mass of ~ 166 u (calc. mass for $C_9H_{10}O_3$: 166.062995 u). Also, the obtained spectrum is in accordance with a previously reported one [12]. No C15 is detected by GC-MS, although it is present in the mixture, as demonstrated by the analyses in the next sections.

Analysis of sample B gives a GC-MS chromatogram that contains three peaks (Fig. S18d). The second one, at 6.943 min, has the same retention time and mass spectrum as the C9 one. Surprisingly, the first peak at 5.582 min is not the one of HMF, as their mass spectra are fundamentally different (Fig. S18e). This peak corresponds to the one at around 6 minutes on the GC-FID chromatogram of the same sample (Fig. S16). The mass of the molecular ion, ~ 159 u, do not correspond to any of the simple byproducts/impurities of HMF and acetone. The third peak at 7.805 min has a mass spectrum whose molecular ion peak appears to be at 206.2 u (Fig. S18f). Given its position in the GC-MS chromatogram, this peak should correspond to the one at 8.33 min in the GC-FID chromatogram (Fig. S16). These peaks were therefore assigned to C12 (Scheme S1, calc. mass for $C_{12}H_{14}O_3$: 206.094295

u). However, the group of C12s comprises different regio- and stereoisomers. It is unclear whether the peaks correspond to a single isomer, or the different isomers have very similar volatilities.

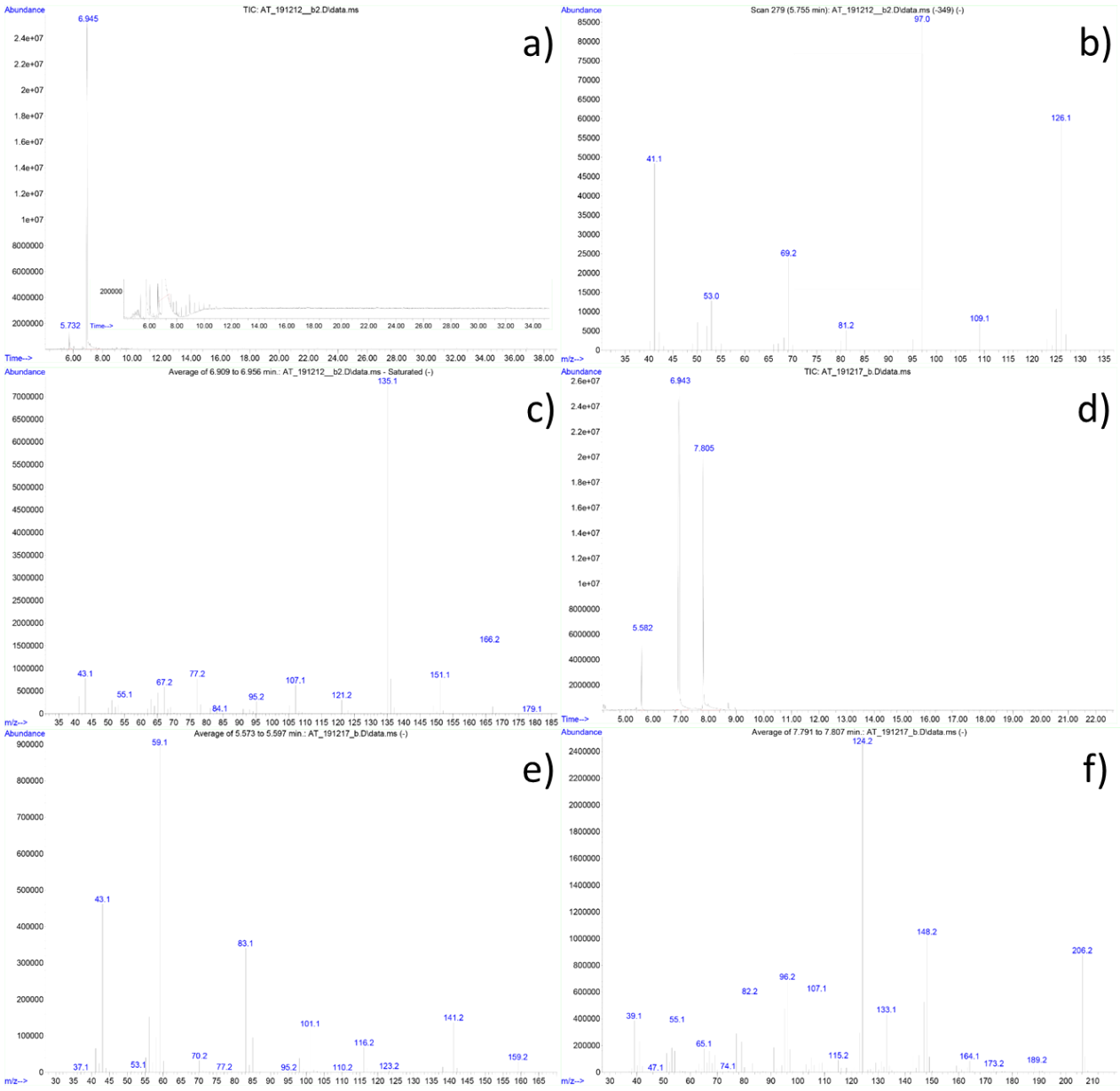

Fig. S18 - GC-MS chromatogram of sample A (a), mass spectrum of the peak at 5.732 min (b, HMF) and at 6.945 min (c, C9); GC-MS chromatogram of sample B (d), mass spectrum of the peak at 5.582 min (e, unknown byproduct/impurity) and 7.805 min (f, C12).

S5.3C - HPLC-DAD

The samples were qualitatively analyzed by HPLC-DAD. The HPLC analysis system (Shimadzu) was composed by the following units: a sampler (SIL-20A HT, equipped with a loop for injections up to 100 μL), a UFLC pump (LC-20AD), a degasser (DGU-20A 3R), an oven containing the chromatographic column (CTO-10AS VP), and a DAD (SPD-M20A). Table S4 summarizes the details of the chromatographic method used for the analyses.

Column	Mediterranea SEA18 (C18) TR-010006			Dimensions	4.6x250 mm x5 μm
Injection volume	5 μL	Flow rate	0.6 mL/min	Temperature	30 ºC
Mobile phase	Composition	Min 0	Min 20	Min 35	Min 50
A	0.1 % HCOOH in H_2O	80	0	0	80
B	MeOH	20	100	100	20

Table S4 - Details of the HPLC-DAD chromatographic method.

This technique was not used for quantification, as it is not appropriate for our reaction system (neat acetone-HMF condensation): the resulting acetone peak is very broad and intense and partially overlaps with the peak of HMF, complicating the determination of the conversion. On the other hand, the chromatograms could provide qualitative information on high molecular weight byproducts that may not have been detected by GC analyses. Fig. S19 shows the HPLC-DAD contour plot chromatogram of Sample C. The sample is very concentrated so that all impurities and byproducts could be detected. Nevertheless, no signal other than the ones of HMF and acetone (together), C9 and C15 are detected in considerable amounts. The big depression at low wavelengths is caused by the change in the mobile phase.

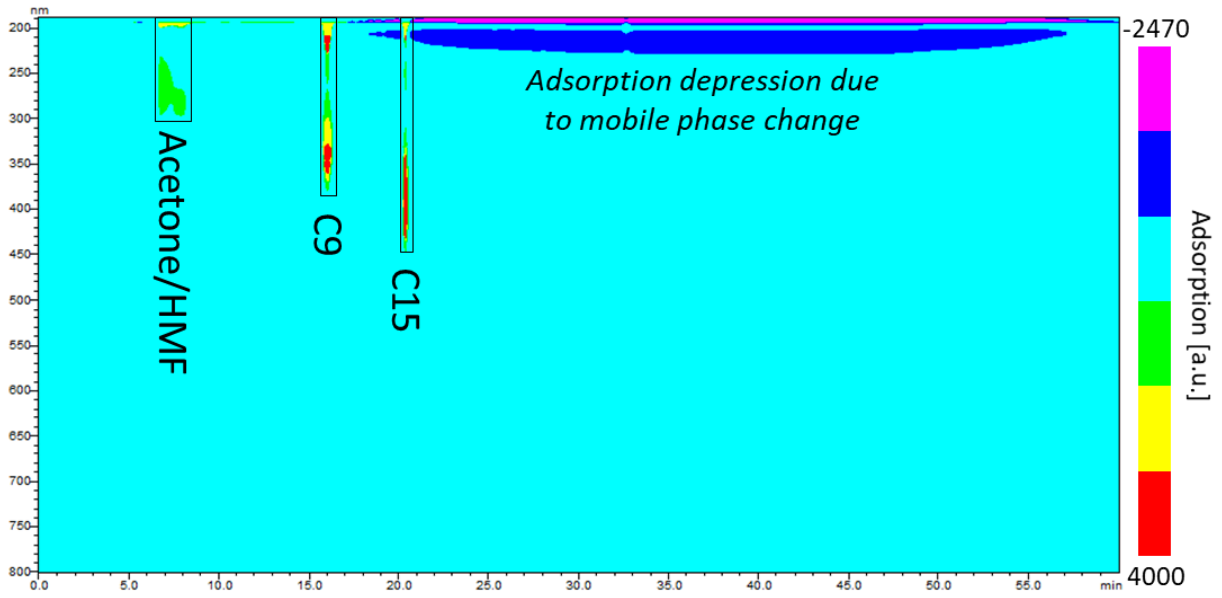

Fig. S19 - HPLC-DAD contour plot chromatogram of Sample C.

In Fig. S20 are reported the retention time and UV-Vis spectra of the various reaction components.

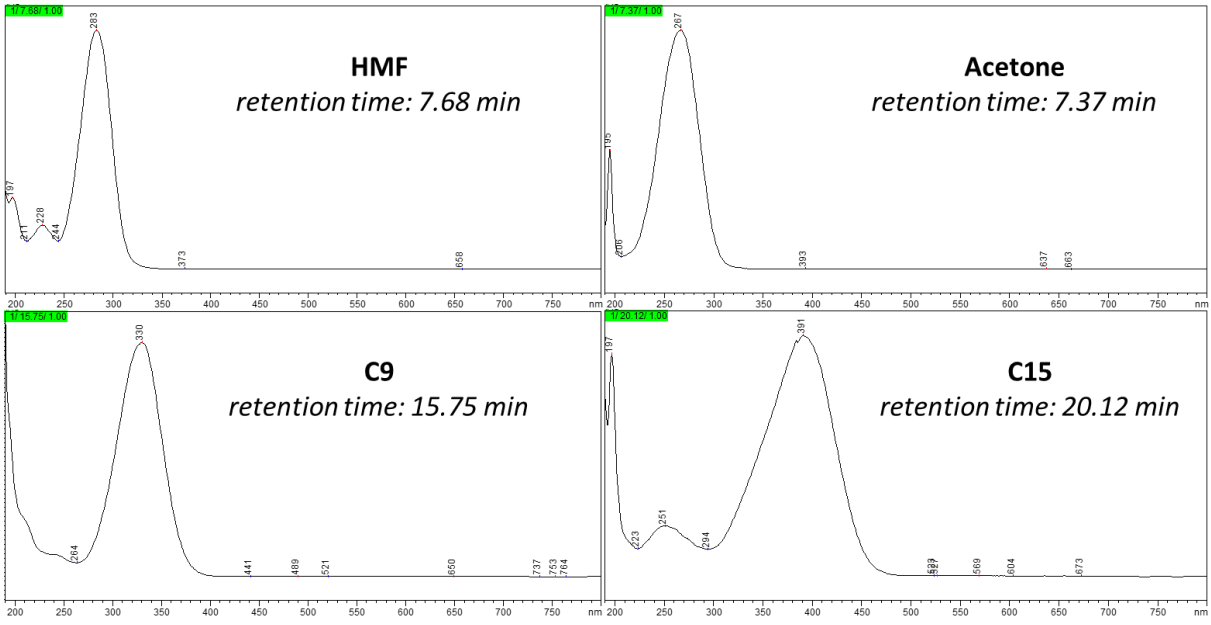

Fig. S20 - UV-vis spectra recorded by HPLC-DAD analysis. The spectra contain a contribute of the mobile phase.

S5.3D - HPLC-TOF

The samples were qualitatively analyzed by HPLC-TOF in order to get information on what could not be detected and/or identified by GC-MS. HPLC measurements were performed using an Agilent

1200 Liquid Chromatograph coupled to a 6210 Time of Flight (TOF) mass spectrometer from Agilent Technologies (Waldbronn, Germany) with an ESI interface. ESI conditions: gas temperature (300 ºC), drying gas (12 L/min), nebulizer (40 psi), fragmentor (120 V), capillary voltage (3000 V), mass range 50-1200. Table S5 summarizes the details of the chromatographic method used for the analyses.

Column	XDB-C18 Zorbax Eclipse P.N 993967-902			Dimensions	4.6x150 mm x5 µm
Injection volume	2 µL	Flow rate	0.6 mL/min	Temperature	r.t.
Mobile phase	Composition	Min 0	Min 15	Min 25	Min 30
A	0.1 % HCOOH in H_2O	80	0	0	80
B	MeOH	20	100	100	20

Table S5 - Details of the HPLC-TOF chromatographic method.

First of all, a blank analysis was performed (Fig. S21a). The chromatogram presents a number of peaks, which should then not be considered for the results interpretation of the next chromatograms.

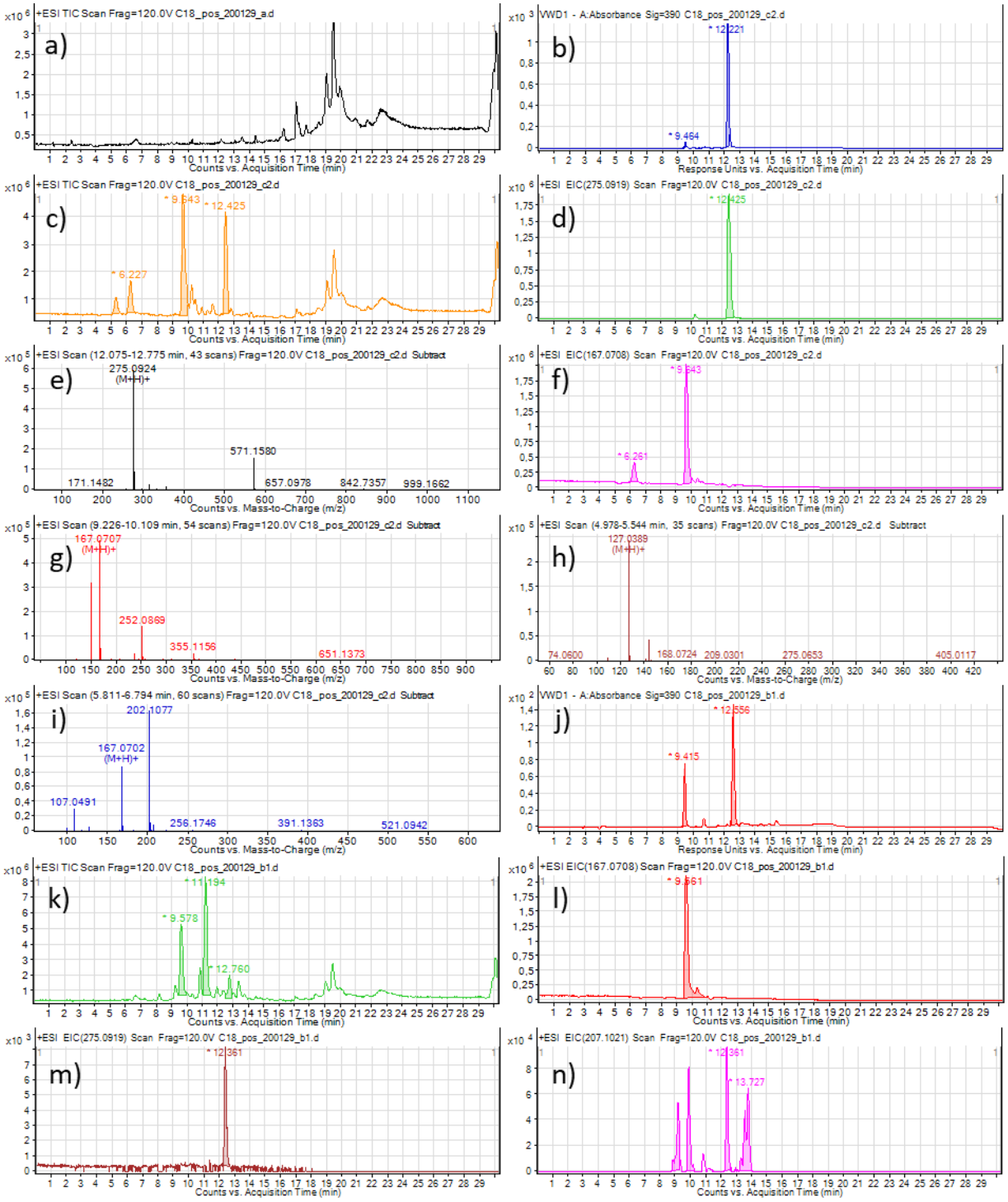

Fig. S21 - HPLC-TOF blank analysis chromatogram (a); absorbance (390 nm) chromatogram of sample C (b), TIC chromatogram of the same (c), EIC chromatogram at a m/z of 275.0919 (d) and m/z spectrum of the peak at ~ 12 minutes (e), EIC chromatogram at a m/z of 167.0708 (f) and m/z spectrum of the peak at ~ 9 minutes (g), at ~ 5 minutes (h) and at ~ 6 minutes (i); absorbance (390 nm) chromatogram of sample B (j), TIC chromatogram (k), EIC chromatogram at a m/z of 167.0708 (l), of 275.0919 (m) and of 207.1021 (n).

Then, sample C was analyzed. Fig. S21b shows the chromatogram obtained by monitoring at 390 nm with a VWD detector [9]. In this chromatogram there is an intense peak that at around 12 minutes that should correspond to C15 given that 390 nm is a maximum in its UV-vis spectrum (Fig. S20); the other, less intense peak at ~ 9 minutes likely corresponds to C9. The corresponding TIC chromatogram is in Fig. S21c. The C15 peak in this chromatogram is at a slightly shifted time because of the order in which the detectors are connected in the analysis sequence. This peak appears in the EIC chromatogram at m/z ~ 275 (Fig. S21d), and its m/z spectrum (Fig. S21e) corresponds to $C_{15}H_{15}O_5$ (and therefore to C15's formula of $C_{15}H_{14}O_5$, considering that the peak is an (M+H)+). Therefore, although C15 does not appear in the GC-MS chromatograms it is can be analyzed by HPLC-TOF. As for the peak at ~ 9 minutes, apparently it corresponds to a mass of ~ 167 (Fig. S21f). Its m/z spectrum has indeed an intense peak corresponding to $C_9H_{10}O_3$ (Fig. S21g). The earliest peak on the TIC chromatogram appears to correspond to HMF, ~ 127, $C_6H_6O_3$ (Fig. S21h). The last peak, at ~ 6 minutes, is not of easy interpretation. Its spectrum (Fig. S21i) does not point to one specific molecule. However, it should be noted that a peak in the same position was also in the blank analysis, although this was less intense in that case, and they may correspond.

Finally, sample B was analyzed. The corresponding VWD chromatogram is shown in Fig. S21j. The second peak may at a first glance seem to correspond to C15, but it actually does not (it comes out too late comparing it with the one Fig. S21m). The TIC chromatogram (Fig. S21k) looks substantially different from the one of Sample C (Fig. S21c). In the EIC chromatogram at ~ 167 (Fig. S21l) presents a sharp peak, corresponding to C9 (very similar retention time as the previous one). The EIC chromatogram at ~ 275 (C15, Fig. S21m) also has a peak at a retention time comparable to the one of the previous analysis, although its intensity is much lower. An EIC scan at ~ 207 was performed to look for C12. In this EIC chromatogram (Fig. S21n) multiple peaks are detected that, perhaps, correspond to different diastereoisomers of C12. Nevertheless, the peaks overlap and so do their m/z spectra (Fig. S22a-d): none of the spectra point univocally to a specific molecule (only the peak at ~ 10 minutes points to C9, because they overlap). The same applies to the biggest peak in the TIC

chromatogram (Fig. S21k), as the spectrum at ~ 11 minutes is complicated (Fig. S22e). To conclude, the reaction catalyzed by NaOH at our reaction conditions produces a complex mixture of products whose peaks overlap and cannot be easily assigned by HPLC-TOF.

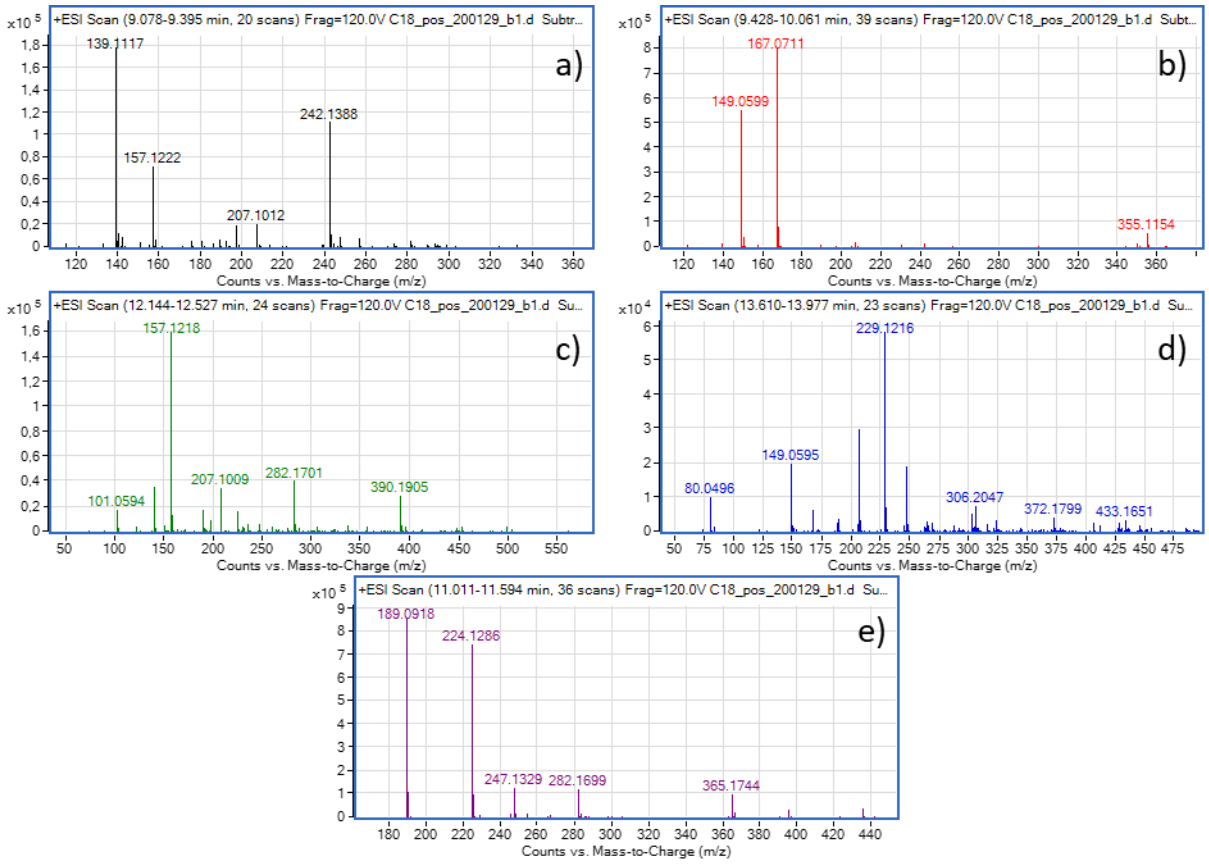

Fig. S22 - m/z spectra of sections of the EIC chromatogram in Fig. 16n: peak at ~ 9 minutes (a), at ~10 minutes (a), at ~ 12 minutes (a), at ~ 13 minutes (a), at ~ 11 minutes (a).

S5.3E - NMR

In Fig. S23 is the spectrum of the analysis of HMF in $CDCl_3$. The assignments match with previously reported data [13]. An additional set of peaks appear in the spectrum of the starting material; the chemical shift of the peaks, as well as their relative positions to the HMF ones correspond to the ones of cirsiumaldehyde, a degradation dimer of HMF [7]. Its relative molar concentration as compared to HMF is ~ 1-2 %.

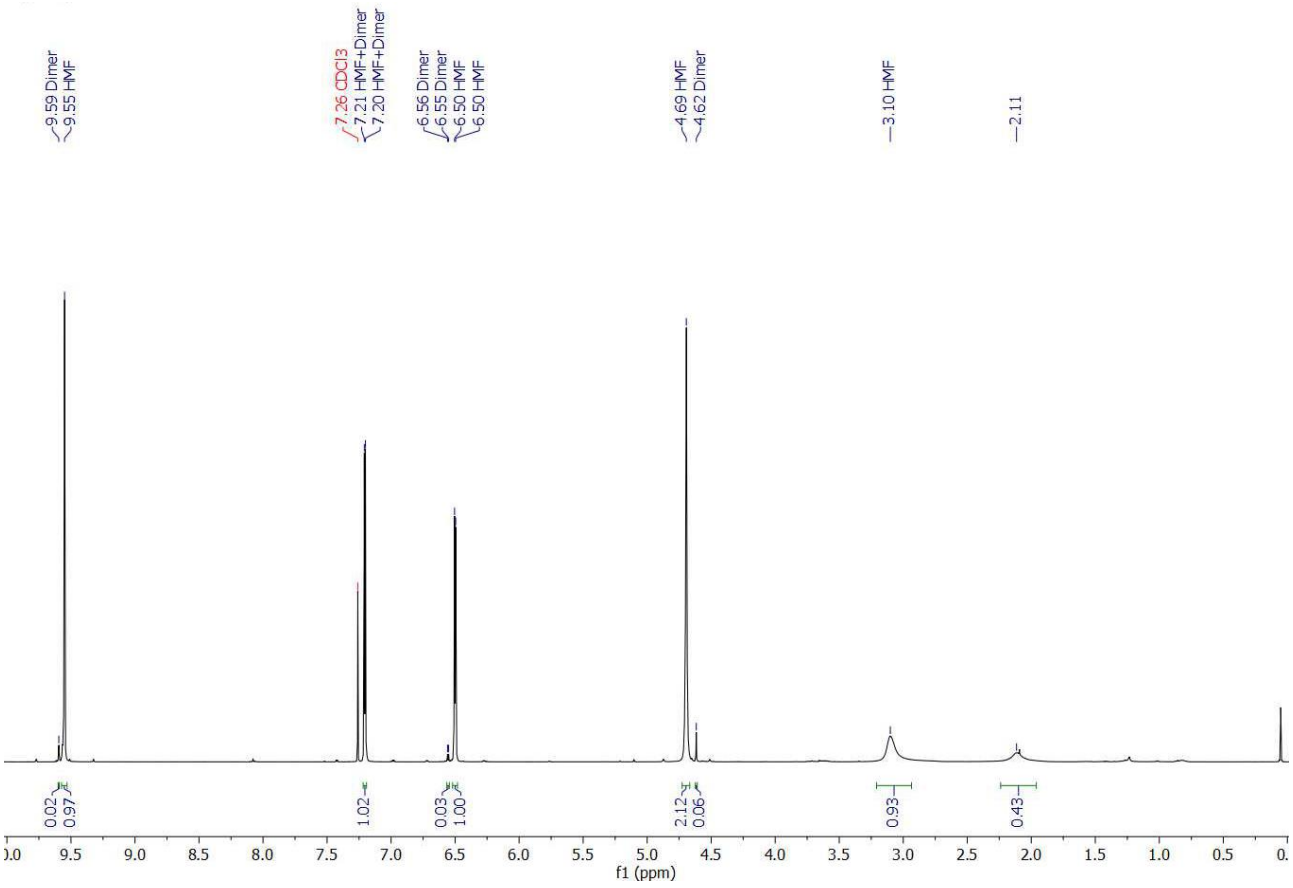

Fig. S23 - Liquid phase ^{1}H-NMR spectrum of the starting material. ^{1}H-NMR (400 MHz, $CDCl_3$) HMF δ 9.55 (s, 1H), 7.20 (d, J = 3.5 Hz, 1H), 6.50 (d, J = 3.5 Hz, 1H), 4.69 (s, 2H), 3.10 (br, 1H). HMF dimer δ 9.59 (s, 2H), ~ 7.20 (hidden) [reported: 7.21 (d, 2H, J = 3.5 Hz)] [7], 6.56 (d, J = 3.5 Hz, 2H), 4.62 (s, 4H).

In Fig. S24 is the spectrum of a reaction crude, dried and re-dissolved in $CDCl_3$ (the spectrum includes ethyl acetate). The assignments of C9 and C15 match with previously reported data, referred to the *trans* and all *trans*, respectively [14]. This, and the magnitude of the coupling constants for the olefinic signals indicates that the obtained isomers are indeed the *trans* and all *trans* ones. Analysis in $CDCl_3$ is not optimal, as in the aromatic/olefinic zone most of the signals are superimposed. Moreover, the samples preparation requires a filtration, an evaporation, a drying and a dissolution.

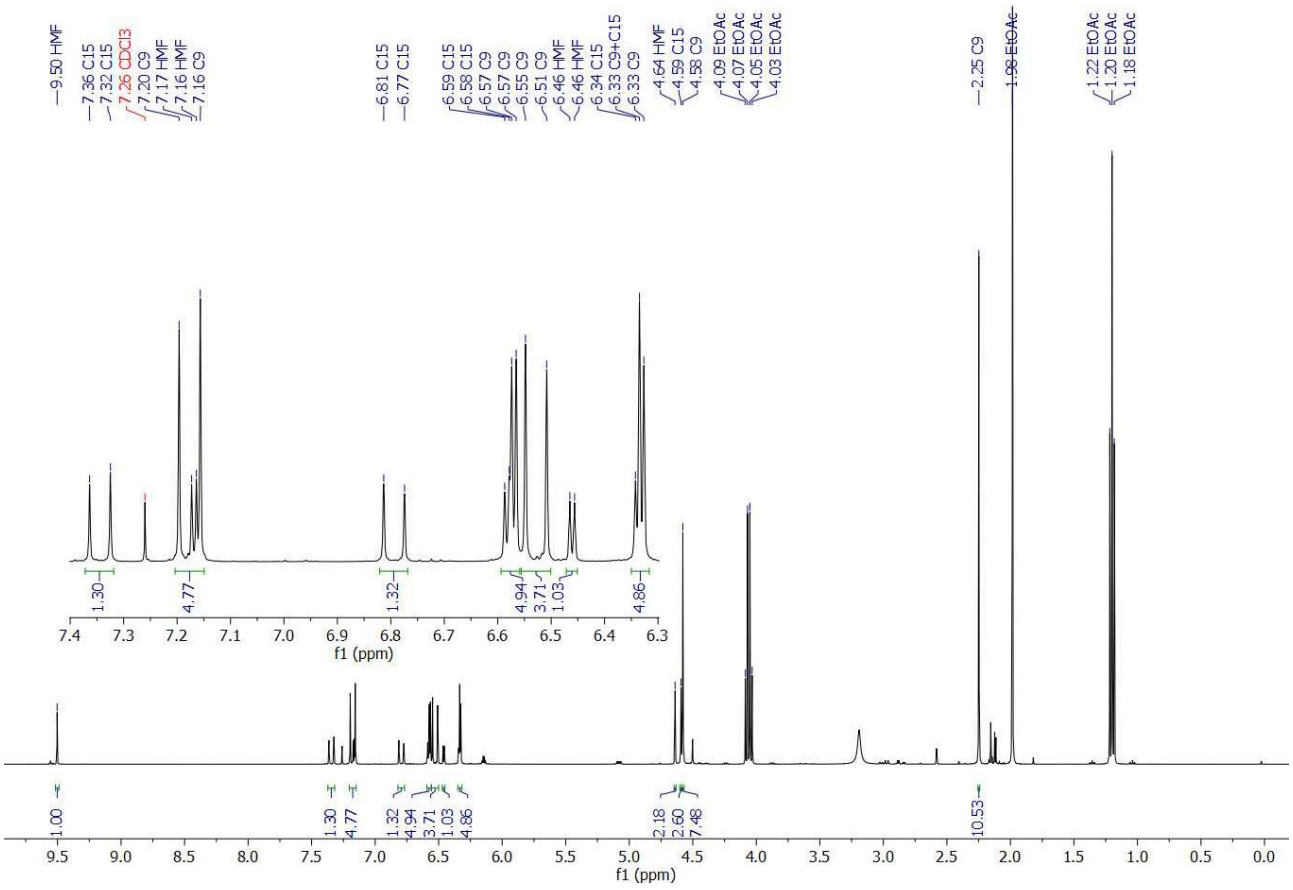

Fig. S24 - Liquid phase ^{1}H-NMR spectrum of the reaction crude, with zoom on the aromatic/olefinic zone. ^{1}H-NMR (400 MHz, $CDCl_3$) C9 δ 7.18 (d, J = 15.9 Hz, 1H); 6.57 (d, J = 3.3 Hz, 1H); 6.53 (d, J = 15.9 Hz, 1H); 6.33 (d, J = 3.3 Hz, 1H); 4.58 (s, 2H); 2.25, (s, 3H). C15 δ 7.35 (d, J = 15.6 Hz, 2H); 6.79 (d, J = 15.6 Hz, 2H); 6.58 (d, J = 3.5 Hz, 2H); 6.34 (d, J = ~ 3 Hz, 2H); 4.59 (s, 4H).

In order to corroborate the assignments, C15 was synthesized by using a different protocol [9], following the procedure to obtain a product molar C9:C15 ratio of 0.04:1. The spectrum obtained after analysis of the crude in $CDCl_3$ is in Fig. S25. The peaks obtained are slightly shifted downfield as compared to the ones assigned to C15 in Fig. S24, but the peak patterns correspond. Importantly, no methylic signal (which only C9 would have) is present in high intensity.

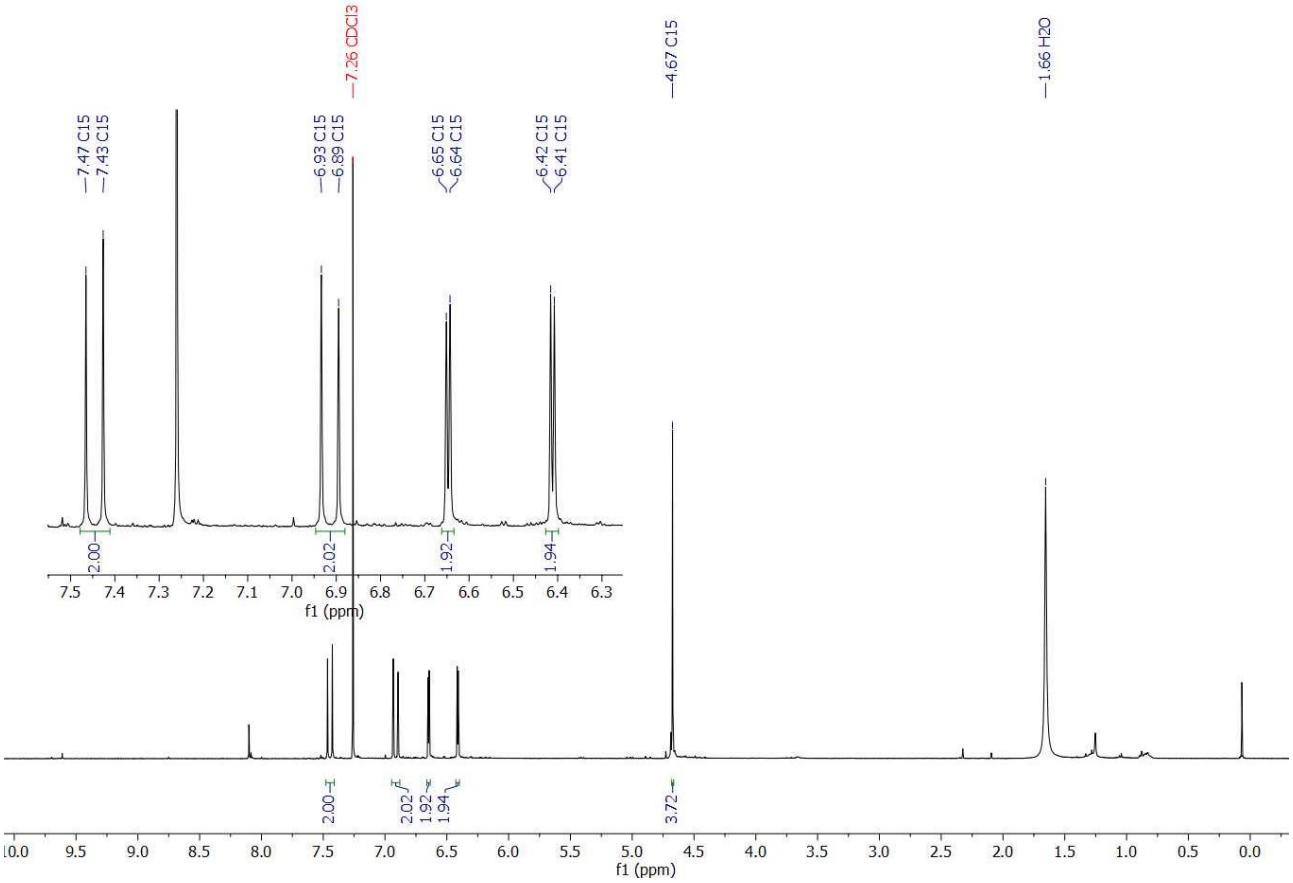

Fig. S25 - Liquid phase ^{1}H-NMR spectrum of C15 synthesized with an alternative protocol, with zoom on the aromatic/olefinic zone. ^{1}H-NMR (400 MHz, $CDCl_3$) C15 δ 7.45 (d, J = 15.6 Hz, 2H); 6.91 (d, J = 15.6 Hz, 2H); 6.65 (d, J = 3.4 Hz, 2H); 6.41 (d, J = 3.4 Hz, 2H); 4.67 (s, 4H).

In Fig. S26 is the spectrum of pure acetone, with a capillary of D_2O inserted in the tube. Three peaks appear: one of acetone, which sets the 2.09 ppm point in the chemical shift scale (it is the chemical shift of acetone in deuterated acetone); one of deuterated water, at 3.81 ppm in our scale; and the last one is water in acetone, moisture (water in deuterated acetone is 2.84 ppm) [15].

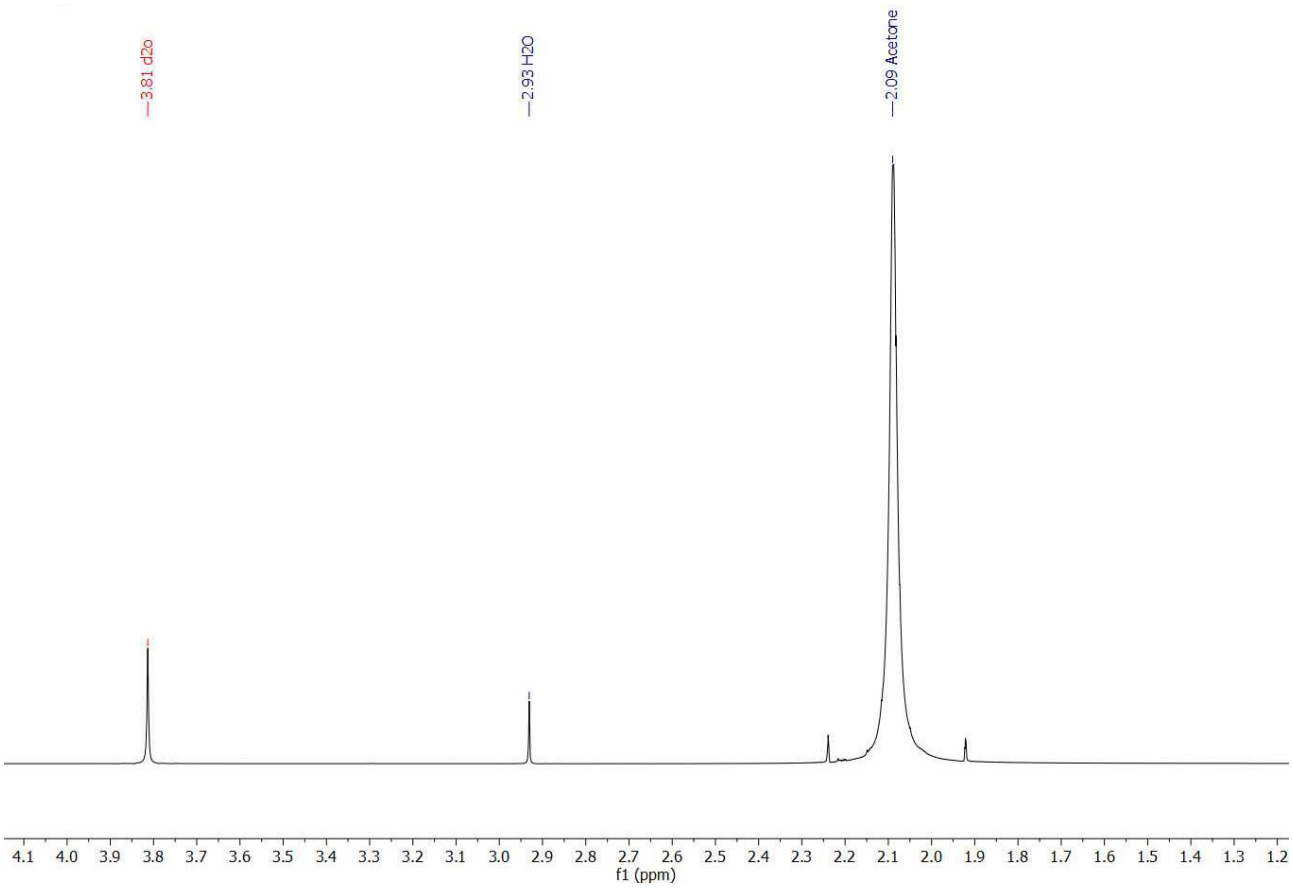

Fig. S26 - Liquid phase ^{1}H-NMR spectrum of pure acetone with capillary. ^{1}H-NMR (400 MHz, no-D acetone) H_2O δ 2.93 (s, 2H).

In Fig. S27 is the spectrum of a final reaction mixture (blank without HMF) in no-D acetone with capillary. In here it is possible to see the signals of diacetone alcohol. The protons of the two aliphatic methyls are clearly visible, and so are the -CH_2- protons; the protons of the carbonylic methyl overlap with the signal of acetone and cannot be clearly assigned; the hydroxylic signal probably overlaps with D_2O (it should be in the same area).

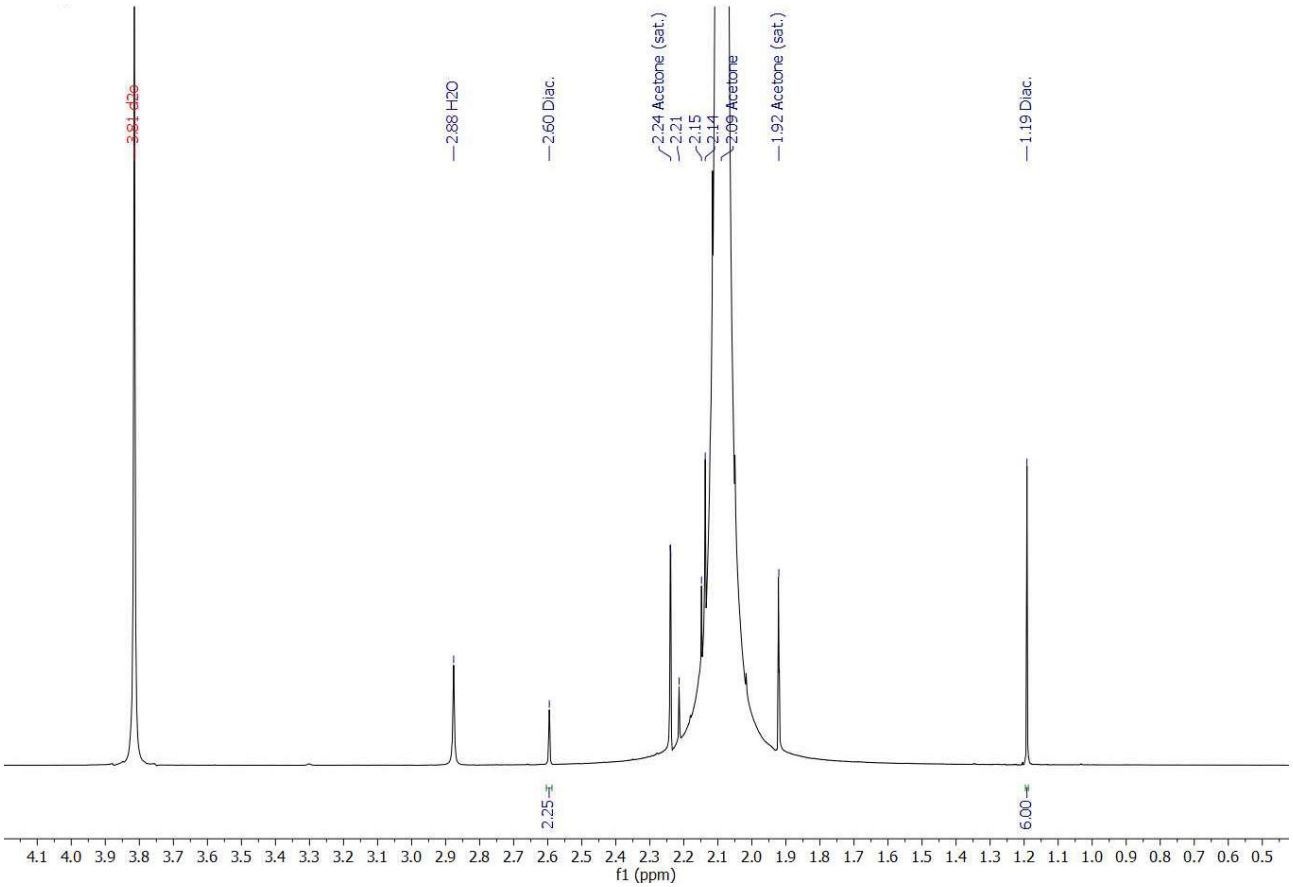

Fig. S27 - Liquid phase ^{1}H-NMR spectrum of a final reaction mixture (blank HMF) with capillary. ^{1}H-NMR (400 MHz, no-D acetone) Diac. δ 2.60 (s, 2H); 1.19 (s, 6H).

In Fig. S28 is the spectrum of HMF in no-D acetone with capillary. Cirsiumaldehyde is also detected.

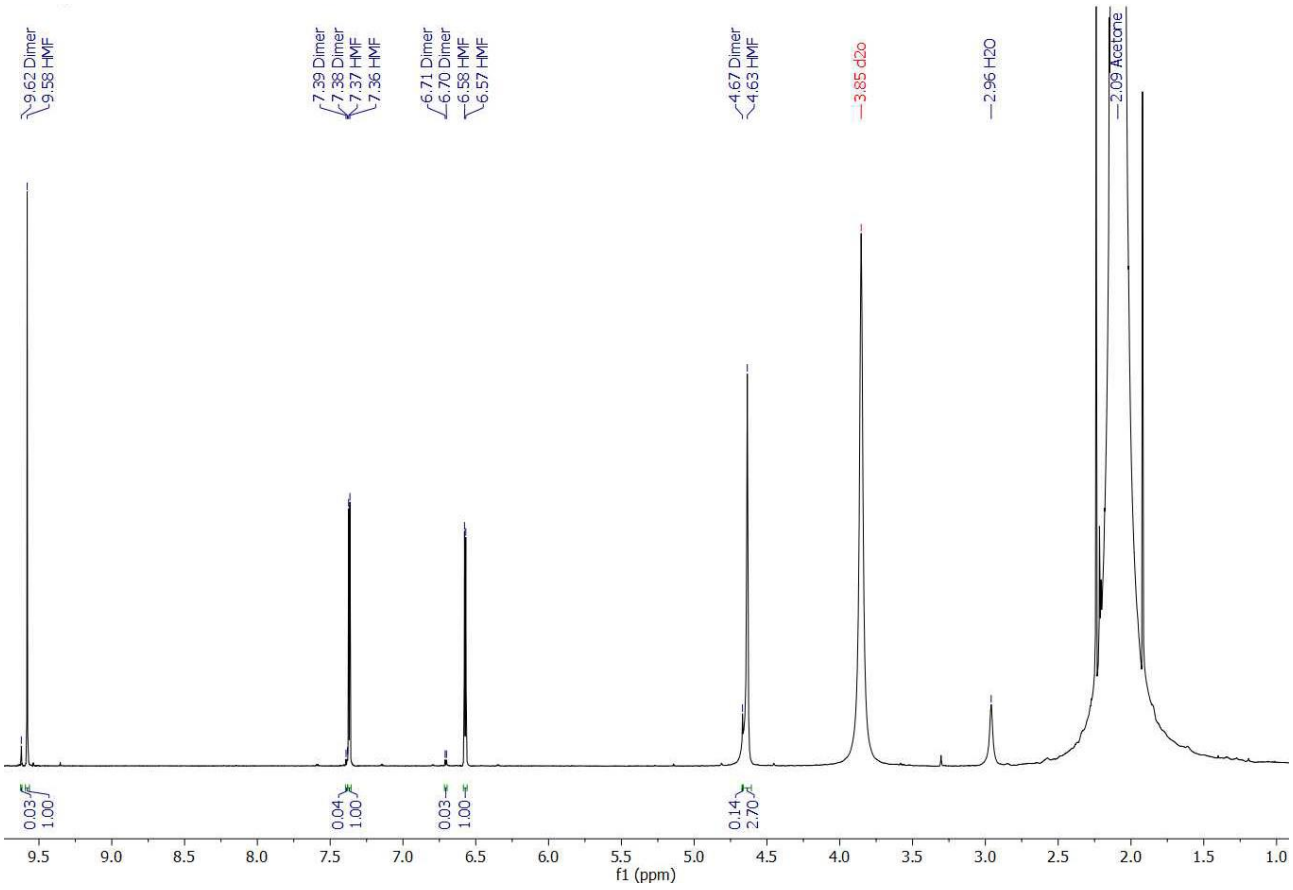

Fig. S28 - Liquid phase ^{1}H-NMR spectrum of the starting material with capillary. ^{1}H-NMR (400 MHz, no-D acetone) HMF δ 9.58 (s, 1H), 7.37 (d, J = 3.6 Hz, 1H), 6.57 (d, J = 3.5 Hz, 1H), 4.63 (s, 2H). HMF dimer δ 9.62 (s, 2H), 7.39 (d, 2H, J = 3.3 Hz), 6.71 (d, J = 3.5 Hz, 2H), 4.67 (s, 4H).

In Fig. S29 is the spectrum of the final reaction mixture in no-D acetone with capillary. For C9 and C15, the proton signals in the aromatic/olefinic zone are the only characteristic ones, as the rest of them have similar molecular neighborhoods to others and their signals overlap. These signals are better resolved than the ones in $CDCl_3$; moreover, no sample preparation is required and no deuterated solvent is wasted, as the capillary can be recovered, clean with acetone and reused right away. The only signal that is off is the one at ~ 6.2 ppm, with relatively low intensity. No other analogous peak could be picked out, and the molecule it originates from has not been identified.

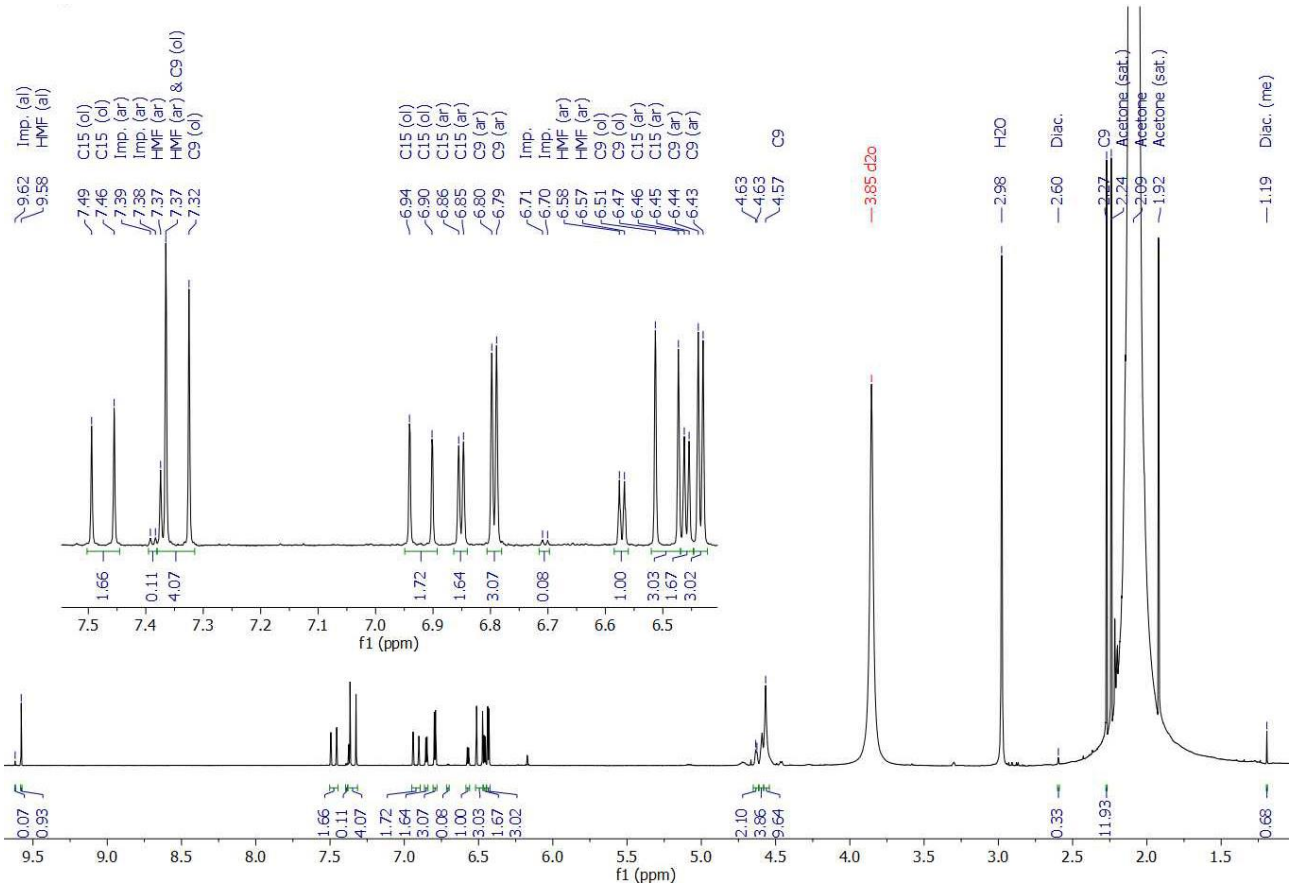

Fig. S29 - Liquid phase ^{1}H-NMR spectrum of the reaction crude, with zoom on the aromatic/olefinic zone. ^{1}H-NMR (400 MHz, no-D acetone) C9 δ 7.34 (d, J = 16.1 Hz, 1H), 6.79 (d, J = 3.4 Hz, 1H), 6.49 (d, J = 16.1 Hz, 1H), 6.43 (d, J = 3.4 Hz, 1H); C15 δ 7.48 (d, J = 15.6 Hz, 2H), 6.92 (d, J = 15.7 Hz, 2H), 6.85 (d, J = 3.3 Hz, 2H), 6.46 (d, J = 3.3 Hz, 2H).

References

[1] M.G. Álvarez, D. Tichit, F. Medina, J. Llorca, Role of the synthesis route on the properties of hybrid LDH-graphene as basic catalysts, Applied Surface Science 396 (2017) 821–831.

[2] S. Abelló, F. Medina, D. Tichit, J. Pérez-Ramírez, X. Rodríguez, J.E. Sueiras, P. Salagre, Y. Cesteros, Study of alkaline-doping agents on the performance of reconstructed Mg–Al hydrotalcites in aldol condensations, Applied Catalysis A: General 281 (2005) 191–198.

[3] M. Mokhtar, A. Inayat, J. Ofili, W. Schwieger, Thermal decomposition, gas phase hydration and liquid phase reconstruction in the system Mg/Al hydrotalcite/mixed oxide: A comparative study, Applied Clay Science 50 (2010) 176–181.

[4] S. Abelló, D. Vijaya-Shankar, J. Pérez-Ramírez, Stability, reutilization, and scalability of activated hydrotalcites in aldol condensation, Applied Catalysis A: General 342 (2008) 119–125.

[5] S.J. Palmer, R.L. Frost, G. Ayoko, T. Nguyen, Synthesis and Raman spectroscopic characterisation of hydrotalcite with CO32− and (MoO4)2− anions in the interlayer, J. Raman Spectrosc. 39 (2008) 395–401.

[6] T. Kim, R.S. Assary, L.A. Curtiss, C.L. Marshall, P.C. Stair, Vibrational properties of levulinic acid and furan derivatives: Raman spectroscopy and theoretical calculations, J. Raman Spectrosc. 42 (2011) 2069–2076.

[7] K.I. Galkin, E.A. Krivodaeva, L.V. Romashov, S.S. Zalesskiy, V.V. Kachala, J.V. Burykina, V.P. Ananikov, Critical Influence of 5-Hydroxymethylfurfural Aging and Decomposition on the Utility of Biomass Conversion in Organic Synthesis, Angewandte Chemie (International ed. in English) 55 (2016) 8338–8342.

[8] J. Cueto Naredo, L. Faba Peón, S. Ordóñez García, Condensación aldólica en fase acuosa de 5-hidroximetilfurfural y acetona sobre óxidos mixtos de carácter básico (in Spanish). Master thesis (Chemical engineering), 2016.

[9] H. Chang, A.H. Motagamwala, G.W. Huber, J.A. Dumesic, Synthesis of biomass-derived feedstocks for the polymers and fuels industries from 5-(hydroxymethyl)furfural (HMF) and acetone, Green Chem. 21 (2019) 5532–5540.

[10] J. Cueto, L. Faba, E. Díaz, S. Ordóñez, Performance of basic mixed oxides for aqueous-phase 5-hydroxymethylfurfural-acetone aldol condensation, Applied Catalysis B: Environmental 201 (2017) 221–231.

[11] J.T. Scanlon, D.E. Willis, Calculation of Flame Ionization Detector Relative Response Factors Using the Effective Carbon Number Concept, Journal of Chromatographic Science 23 (1985) 333–340.

[12] T. Yutthalekha, D. Suttipat, S. Salakhum, A. Thivasasith, S. Nokbin, J. Limtrakul, C. Wattanakit, Aldol condensation of biomass-derived platform molecules over amine-grafted hierarchical FAU-type zeolite nanosheets (Zeolean) featuring basic sites, Chemical communications (Cambridge, England) 53 (2017) 12185–12188.

[13] A. Dibenedetto, M. Aresta, L. Di Bitonto, C. Pastore, Organic Carbonates: Efficient Extraction Solvents for the Synthesis of HMF in Aqueous Media with Cerium Phosphates as Catalysts, ChemSusChem 9 (2016) 118–125.

[14] H. Quiroz-Florentino, R. Aguilar, B. Santoyo, F. Díaz, J. Tamariz, Total Syntheses of Natural Furan Derivatives Rehmanones A, B, and C, Synthesis 2008 (2008) 1023–1028.

[15] G.R. Fulmer, A.J.M. Miller, N.H. Sherden, H.E. Gottlieb, A. Nudelman, B.M. Stoltz, J.E. Bercaw, K.I. Goldberg, NMR Chemical Shifts of Trace Impurities: Common Laboratory Solvents, Organics, and Gases in Deuterated Solvents Relevant to the Organometallic Chemist, Organometallics 29 (2010) 2176–2179.